ABSTRACT

NONDESTRUCTIVE EVALUATION OF 3D PRINTED, EXTRUDED, AND NATURAL POLYMER STRUCTURES USING TERAHERTZ SPECTROSCOPY AND IMAGING

by
Alexander T. Clark

Terahertz (THz) spectroscopy and imaging are considered for the nondestructive evaluation (NDE) of various three-dimensional (3D) printed, extruded, and natural polymer structures. THz radiation is the prime candidate for many NDE challenges due to the added benefits of safety, increased contrast and depth resolution, and optical characteristic visualization when compared to other techniques. THz imaging, using a wide bandwidth pulse-based system, can evaluate the external and internal structure of most nonconductive and nonpolar materials without any permanent effects. NDE images can be created based on THz pulse attributes or a material's spectroscopic characteristics such as refractive index, attenuation coefficient, or the level birefringence present within. The evaluation processes for polyethylene gas pipes and amber specimens lack efficient and accurate NDE techniques while 3D printed polymer structures currently have no standardized NDE methods. The primary focus of this research is to determine and evaluate the use of THz spectroscopy and imaging as a NDE technique for a variety of polymers extruded mechanically and naturally.

Results indicate the refractive indices, attenuation coefficients, and level of birefringence of several 3D printing filaments including copolyester (CPE), nylon, polycarbonate (PC), polylactic acid (PLA), and polypropylene (PP) may change depending on the printing parameters. THz spectroscopy is used to measure relative permittivity of printed ceramic samples with various sintering temperatures. THz imaging proves to be a

successful method to diagnose print head misalignment in ceramic nanoparticle jetting printing processes. Proper diagnosis of surface level defects on polyethylene (PE) gas pipelines is achieved along with preliminary joint fault imaging and 3D visualization by creating an interactive detailed map of surface level defects. THz NDE imaging, combined with tailored refractive index matching materials, can construct tomographic images and 3D reconstructions of multi-million-year-old amber. Visual and THz birefringence images are created to determine stress direction within extruded PE and amber. These results suggest that THz spectroscopy and imaging have multiple confirmed uses in the NDE of polymer structures, both mechanically and naturally fabricated.

NONDESTRUCTIVE EVALUATION OF 3D PRINTED, EXTRUDED, AND NATURAL POLYMER STRUCTURES USING TERAHERTZ SPECTROSCOPY AND IMAGING

by
Alexander T. Clark

A Dissertation
Submitted to the Faculty of
New Jersey Institute of Technology
in Partial Fulfillment of the Requirements for the Degree of
Doctor of Philosophy in Materials Science and Engineering
Materials Science Option

Interdisciplinary Program in Materials Science and Engineering

May 2022

APPROVAL PAGE

NONDESTRUCTIVE EVALUATION OF 3D PRINTED, EXTRUDED, AND NATURAL POLYMER STRUCTURES USING TERAHERTZ SPECTROSCOPY AND IMAGING

Alexander T. Clark

Dr. John F. Federici, Dissertation Advisor — Date
Distinguished Professor, Department of Physics, NJIT

Dr. Ian Gatley, Committee Member — Date
Distinguished Professor, Department of Physics, NJIT

Dr. Keun Ahn, Committee Member — Date
Associate Professor, Department of Physics, NJIT

Dr. Shawn A. Chester, Committee Member — Date
Associate Professor, Department of Mechanical and Industrial Engineering, NJIT

Dr. Robert Barat, Committee Member — Date
Professor Emeritus, Department of Chemical and Materials Engineering, NJIT

Dr. Phillip Barden, Committee Member — Date
Assistant Professor, Department of Biological Sciences, NJIT

BIOGRAPHICAL SKETCH

Author: Alexander T. Clark

Degree: Doctor of Philosophy

Date: May 2022

Undergraduate and Graduate Education:

- Doctor of Philosophy in Materials Science and Engineering,
  New Jersey Institute of Technology, Newark, NJ, 2022

- Bachelor of Science in Engineering Physics,
  Ramapo College of New Jersey, Mahwah, NJ, 2017

Major: Materials Science and Engineering

Presentations and Publications:

P. Barden, C. E. Sosiak, J. Grajales, J. Hawkins, L. Rizzo, A. T. Clark, S. Gatley, I. Gatley, and J. F. Federici, "Non-destructive Comparative Evaluation of Fossil Amber Using Terahertz Time-domain Spectroscopy," *PLOS One,* (2022).

M. Carr, D. Desai, C. Bolton, A. T. Clark, I. Gatley, S. Gatley, L. Rizzo, and J. F. Federici**,** "Design and Fabrication of 2D and 3D Patterned Chaff," *Journal of DoD Research and Engineering (JDR&E), Under Review,* (2022).

A. T. Clark, J. F. Federici, and I. Gatley, "Effect of 3D Printing Parameters on the Refractive Index, Attenuation Coefficient, and Birefringence of Plastics in Terahertz Range," *Advances in Materials Science and Engineering,* vol. 2021, Article ID 8276378, (2021).

P. Parsons, A. T. Clark, Z. Larimore, A.J. Good, S. Gatley, J. Federici, and M. Mirotznik, "Millimeter and Sub-millimeter Wave Electromagnetic Characterization of Additively Manufactured Zirconia Ceramics via NanoParticle Jetting." *IEEE Transactions on Components, Packaging and Manufacturing Technology, Under Review,* (2021).

J. F. Federici, L. Rizzo, A. T. Clark, C. Bolton, S. Gatley, and I. Gatley, "Industrial Applications of THz Imaging: Plastics, Food Industry, Moisture Detection, and Additive Manufacturing" *OSA Technical Digest,* (2020).

A. T. Clark and J. F. Federici, “Quantifying the Effect of 3D Printing Parameters on the Refractive Index of Plastics in the Terahertz Range,” Poster Presentation delivered virtually at the Optical Sensors and Sensing Congress, June 2020.

Reports

A. T. Clark, C. Bolton, I. Gatley, S. Gatley, and J. F. Federici, “Benchtop Demonstration of Atmospheric & Weather Effects on Terahertz Power Beaming to an Intel Harvester Chip,” *Value Engineering for Enhances Workforce Development Training and Technology Demonstration,* (2021).

A. T. Clark, C. Bolton, I. Gatley, S. Gatley, and J. F. Federici, “Field Deployable Laser Power Beaming for Unmanned Vehicle Applications” *Value Engineering for Enhances Workforce Development Training and Technology Demonstration,* (2021).

C. Stavrou and A. T. Clark, “Piezoelectric Material Evaluation as a Strain Sensor for Indirect Fire Systems” *ADAPT Task 13,* (2017).

Confidence is the key to success, both self and from others.

This work is dedicated to my mother and father, Nancy and Thomas Clark,

the ones who always have that confidence in me.

ACKNOWLEDGMENT

I would like to personally thank several individuals that have contributed to the completion of this dissertation. Before all else, I would like to express my upmost appreciation to my Dissertation advisor, Dr. John Federici, for all the guidance, patience, and unwavering support throughout this adventure. His remarkable work ethic, knowledge, acumen, and continued encouragement are truly inspirational. It terahertz to think I will no longer be working under his direction, but I have learned a great deal from him over the years and could not be more thankful for his instruction and supervision.

Thank you to Dr. Ian Gatley for not only the scientific insight and push to look at things from outside the box, but also the reassurance when I needed it the most. I would like to extend my gratitude to my committee, Dr. Keun Ahn, Dr. Robert Barat, Dr. Shawn Chester, and Dr. Phillip Barden, for their time and support.

I would like to thank the US Army Combat Capabilities Development Command (CCDC) Armaments Center at Picatinny Arsenal for the research funding as well as the Defense University Research Instrumentation Program (DURIP) of the U.S. Army for the instrumentation support. I would also like to thank NYSEARCH as well as the Department of Physics at NJIT for their financial support.

I gratefully recognize the help and support of Christopher Bolton, Samuel Gatley, and Louis Rizzo. Not only did I get the great opportunity to call all of them coworkers and classmates, but more importantly friends. Each one of you has literally been with me throughout this entire experience, some even through undergrad, and each one of you has helped me in distinct and invaluable ways that have and will continue to push me towards

success. I also want to express my extreme appreciation to Lindsey Gray. The many years of help, both personal and academic, are simply unmatched. She has not only been my rock when I needed it the most, but also my best friend throughout this entire journey.

I also want to thank all the AddLab members that have helped me over the years at NJIT including Dr. Carley Mollica, Dr. Jimmie Adriazola, Dhruvkumar Desai, Sophia D'Anna, Nicholas Warholak, and Jessy Nemati. I want to extend my gratitude to everyone else that helped me along the way, whether big or small, every bit counts.

Most importantly, I owe my deepest gratitude to my parents, Nancy and Tom Clark. Their endless, unconditional, and loving support turned my vision of getting a PhD into reality. I have always said that I could have never asked for better parents, and this proves it. Having the ability to instill confidence in someone while simultaneously guiding them to reach their goals is not an easy task, but they succeeded. This work simply wouldn't have been possible without you both. Thank You.

TABLE OF CONTENTS

TABLE OF CONTENTS
(Continued)

Chapter **Page**

LIST OF TABLES

LIST OF FIGURES

LIST OF FIGURES
(Continued)

Figure **Page**

LIST OF FIGURES
(Continued)

Figure **Page**

LIST OF FIGURES
(Continued)

Figure **Page**

LIST OF FIGURES
(Continued)

LIST OF FIGURES
(Continued)

Figure **Page**

LIST OF ACRONYMS

AM	Additive Manufacturing
ART	Algebraic Reconstruction Technique
BCB	Benzocyclobutene
CAD	Computer-Aided Design
CPE	Copolyester
CT	Computed Tomography
DFT	Discrete Fourier Transform
DoD	Department of Defense
ERM	External Reference Mirror
ERS	External Reference Structure
FBP	Filtered Back Projection
FDM	Fused Deposition Modeling
FFT	Fast Fourier Transform
HDPE	High Density Polyethylene
MDPE	Medium Density Polyethylene
NDE	Nondestructive Evaluation
NDT	Nondestructive testing
NIST	National Institute of Standards and Technology
NPJ	Nanoparticle Jetting
PC	Polycarbonate
PCA	Photoconductive Antenna

PE	Polyethylene
PLA	Polylactic Acid
PP	Polypropylene
SART	Simultaneous Algebraic Reconstruction Technique
THz	Terahertz
ToF	Time-of-Flight
2D	Two-Dimensional
3D	Three-Dimensional

CHAPTER 1

INTRODUCTION

Nondestructive testing (NDT) or nondestructive evaluation (NDE) methods are a group of techniques currently in use by various industries to test and inspect different aspects and characteristics of materials, components, or full systems without permanent damage. NDE is extremely useful because it can save time and money in several aspects of production by allowing for rapid and significant assessment without sacrifice of the object being inspected, especially valuable or rare samples that other techniques would normally damage [1]. The goal of the research presented in this dissertation is to apply NDE techniques in the form of Terahertz (THz) spectroscopy and imaging to various manufactured and naturally extruded polymers, testing their applicability and effectiveness dependent on the structure and its application.

THz radiation refers to the electromagnetic waves between the microwave and infrared spectrums from 0.1-10THz and wavelengths of 3mm-30um [2]. This range of frequencies is commonly referred to as the "THz gap" because the technology related to the creation, manipulation, and implementation of these waves is still relatively new and not widely utilized. THz radiation offers many benefits over other traditional material evaluation techniques. Specifically, THz frequencies are non-destructive and non-ionizing to materials through which THz radiation is transmitted. This electromagnetic radiation does not carry enough energy per quantum to ionize the atoms or molecules that are exposed at the power levels used in this research.

Verification of using THz spectroscopy and imaging techniques as a means of NDE of extruded polymers is needed. The processes of evaluation and qualification of manufactured products is extremely important. Currently, there are few adapted techniques that are both safe and effective for the thorough evaluation of extruded polymers with the added benefits brought forth by THz NDE. Current techniques, such as individual X-rays and CT scans, require strict safety protocol and are much less accessible than THz imaging due to their hazardous and damaging nature [3]–[5]. Since THz radiation is relatively safe compared to X-rays and laser-based methods, it is easier to implement in NDE scenarios. THz radiation is completely skin and eye safe at the power being used in this presented research. Using the research presented, means of evaluation, qualification, and certification of various extruded polymers both manufactured and natural, can be pursued, created, and standardized for different applications.

This dissertation is organized into three main topics. The first topic focuses on the utilization of THz NDE on additive manufactured plastic and ceramic structures. The second topic also has industrial motivation: observation and detection of defects in plastic gas pipes post manufacturing, coupling, and use. The third topic, like the first two, utilizes THz NDE to detect and observe defects and voids in a polymer material. However, rather than emphasizing industrial motivation, the third application employs this technique on a naturally occurring polymer, fossilized amber, with paleontology-based motivation.

CHAPTER 2

BACKGROUND

2.1 Additive Manufacturing

The term additive manufacturing (AM) encompasses all the processes that create objects by adding material to create a final structure. The currently accepted types of additive manufacturing include material extrusion, material jetting, binder jetting, sheet lamination, vat polymerization, powder bed fusion, and direct energy deposition [6]. The terms AM and three-dimensional (3D) printing can generally be used interchangeably.

There is a general order-of-procedures to 3D print an object. The first step in 3D printing of any structure is creating a 3D model using Computer-Aided Design (CAD) software. Once modeled, the structure is then transferred to a slicing software, where the different structural parameters are requested, such as the structures infill, layer heights, size, and orientation. The slicing software then "slices" the model into a programming language called G-code. This G-code acts as a set of instructions that will tell the printer exactly what to do to successfully print the model with the specifications requested [7]. Once the G-code is transferred to the printer, the printing process may begin.

2.1.1 Qualification and Certification

AM is currently being held back from becoming a mainstream manufacturing technique due to the lack of standards for quality assurance and qualification of additive manufactured parts. The National Institute of Standards and Technology (NIST), an agency of the United States Department of Commerce and comprised of six research laboratories, states that there are actually no additive manufactured materials or processes that have been

specifically qualified for critical defense or aerospace applications [8]. This is where THz NDE of additively manufactured parts can play a major role within the industry and this qualification process.

In 2016, the United States Department of Defense (DoD) in conjunction with *America Makes* released a roadmap for AM. This roadmap was created as an overview of the steps to efficiently mature the technology of AM needed for DoD to fully adopt and utilize this technology, along with applications in the public sector. The DoD was concerned with the technical areas of design, material, process, and value chain as well as three non-technical areas including cultural change, workforce development, and data management for the modernization and adoption of AM [9]. THz NDE research in conjunction with 3D printing pursues the progress of both the material and process objectives. Recently in 2021, the DoD released an updated version of the AM roadmap as a full strategy outlining the current objectives and barriers as the related technology has been evolving. In this strategy, the DoD defines the number one barrier to move AM into the realm of accepted manufacturing technologies as "rapid and standardized approaches for qualification of materials and processes, and certification of AM parts." The development of THz NDE techniques for these AM parts can play a major role in the full adoption of this technology [10]. As stated in the original DoD roadmap, additive manufacturing has the ability to become cheaper, faster, and more reliable than most current manufacturing techniques [9].

The term "qualification" in terms of additively manufactured structures refers to satisfying different requirements put forth by the original design. The final product must satisfy dimension restraints. A major concern with additively manufactured parts is

shrinkage. Research has been performed in creating low shrinkage ratio materials for different applications that require strict dimensional constraints, such as dental crowns, but even those show signs of shrinkage of over 2% [11]. Qualification and evaluation of the final dimensions, both internal and external are key to a functional product. Due to the nature of the production process, AM parts frequently have internal voids and structural defects that are not visible under visual inspection. THz NDE will allow for quick detection through imaging of these defects long before failure may occur.

THz NDE also has the capability of creating 3D reconstructions of the structure being imaged using THz computed tomography (CT) reconstruction and related software. Like traditional X-ray CT, THz CT has been implemented before for NDE internal structure observation. Comparison of various reconstruction algorithms using THz CT have been performed and evaluated [12]. Different correction algorithms have been created to correct for refraction losses and Fresnel reflection boundary effects, but little research has been done utilizing THz CT on 3D printed structures [13], [14]. THz CT of 3D printed structures can aid in several areas within the industry such as rapid prototyping, failure analysis, and material characterization.

NDE can also characterize the electromagnetic properties of 3D printed structures. Recently, there have been advances in using fused deposition modeling (FDM) printers to print microwave and THz based passive optical components such as waveplates, phase plates, antennas, and lenses [15]–[17]. 3D printed ceramic structures are being designed for applications in filters, capacitors, dielectric resonator antennas, even 5G devices [18]-[19]. The accuracy, reproducibility, and electromagnetic response of such 3D printed structures will likely depend on the structures printing parameters, and so the ability to

fine-tune properties such as refractive index, attenuation coefficient, birefringence, and relative permittivity will depend on detailed knowledge of such dependencies. THz spectroscopy has been proven time and time again to be a reliable means for optical property characterization [20]–[23].

THz optical properties of some 3D printable plastics including Polylactic acid (PLA), Nylon, and Polypropylene (PP) have been previously reported from experiments that did not refer to the specifics of the printing process. Reference [24] measured the real refractive index as well as the absorption coefficient for a few FDM filaments seen in Table 2.1. These measurements were printing parameter independent and analyzed using the quasi-space minimization algorithm which uses the imaginary part of the complex refractive index to calculate its absorption coefficient [24], [25].

Table 2.1 Real Refractive Index and Absorption Coefficient at 0.5 THz for Various Materials

Material	Refractive Index (real)	Absorption Coefficient (cm^{-1})
PLA	1.89	11
Nylon	1.72	9
PP	1.495	0

Source: [24]

Another previous reference reported an absorption coefficient of 10 cm^{-1} at 500 GHz for a PLA 3D printed sample [26]. This measurement was once again printing parameter independent and measured using intensity as opposed to electric field. Commercially available filaments were analyzed in Reference [27] for their real refractive indices and absorption coefficients using optimized printing parameters. This research differentiates itself from previous studies by investigating the changes in the refractive

index and absorption coefficient in the THz gap using electric field transmission measurements of a 3D printed structure due to varying printing parameters used in the 3D printing process. No optical property variations due to changes in printing parameters have been previously reported.

2.2 Extruded Polyethylene Gas Pipes and Joints

Polyethylene (PE) pipes are becoming the preferred method for the transfer of natural gas, replacing the older steel and cast-iron natural gas distribution systems. PE pipes are inherently more corrosion resistant and ductile than their metal counterparts, available in a variety of density compositions depending on the application.

Solid wall PE pipes are manufactured by extrusion. Raw material, called PE compound, along with pigments depending on the application, are fed into an extruder. The extruder is responsible for heating and melting the PE compound between temperatures of 200 °C and 235 °C under high pressure between 2000 psi and 4000 psi, where it is then properly mixed and forced through an annular die using an extrusion screw. The pipe is then sized either through an external vacuum or internal pressurized sizing process. Once properly sized based on application specifications, the pipes are cooled by either total immersion or spray cooling. The pipes internal temperature must be below 71 °C before handling can occur [28].

Post manufacturing, lengths of pipes must be joined, both on and off site, to create a full distribution system. The process for connecting the ends of two PE pipes using heat and pressure is called heated butt fusion. There is a specific process that is followed for creating heat fusion joints in PE pipes. First, the pipes must be properly aligned in either a

hydraulic or manual butt fusion machine. Once aligned, a facing tool shaves the pipe ends to create a clean fusion surface. A heating tool is then inserted between the pipes to heat the end surfaces to between 400 °C and 450 °C. The pipes are pressed together with an interfacial pressure, calculated based on the pipes size, of between 60 psi and 90 psi. Beads are created around the joint location because of the fusion process. Fusion is considered complete when the heated surfaces are brought together with enough force to roll the fusion melt beads over to the pipes surface. After a period of cooling, the pipes are considered fused and ready to be used in their application [29].

2.2.1 Defect Detection and Characterization

Defects present in PE gas pipes can be a major threat to both the people and property that surround them. PE gas pipes experience different types of stress and can obtain various defects that may result in their failure, including the repeated freezing and thawing of the surrounding ground, blunt damage and crushing, or defects created during the manufacturing and joining processes. It is extremely important to be able to characterize and locate any defects present within gas pipes. Current methods of polyethylene gas pipe evaluation include visual inspection and guided wave techniques [30], [31]. Guided wave techniques rely on either axial or circumferential measurements that lack in resolution on the non-measured axis, as where THz imaging can create direct representations of the defects.

There are three types of defects that can be present within a gas pipe: surface level, internal, or within a joint, all which could be missed using the current pipe evaluation techniques. Surface defects are the first sign of a poorly extruded PE gas pipe or a sign that the pipe has experienced some sort of physical damage. Many times, visual inspection will

not be sufficient in identifying all surface level defects. THz NDE is capable of imaging and characterizing all surface level defects including scratches, dents, gouges, over-clamping, or manufacturing errors present on the surface of PE pipes. Internal defects in the PE extrusion usually cannot be seen under visual inspection due to the pigment of the pipes and can be missed using guided wave techniques if not within the axial or circumferential detection resolution. If a gas pipe has internal defects, the likelihood of critical failure of that pipe dramatically increases. THz NDE can locate those defects while also determine their severity without the need for visual inspection before said failure has the chance to occur.

A joint is considered a failure during or after the fusion process if certain indicators are observed. During the heating process, if there is a concave melt surface in the pipe wall, the joining process must be abandoned and restarted, because this can introduce air pockets into the joint effectively weakening it. Another indicator is the melt appearance, such as texture and size, along the bead after fusion. If the appearance does not meet the set requirements, it can indicate a weak or poor joint fusion. Many defects cannot be detected through visual inspection during or after the fusion process, resulting in complete failure of that joint during use. A joint can be over or under pressured during the joining procedure with minimal visual indication [29]. Contaminants may be introduced into the joint such as oil, grease, sand, or mud which can be invisible from the outside. Air pockets may be present between the joined surfaces. THz NDE may have the capability to characterize these different defects post joint fusion and pre-use unlike visual inspection.

2.3 Amber Specimens

Amber, to which has many different names including succinite, resinite, fossil resin, and Baltic gold, is most importantly referred to as nature's time capsule. Amber is created from resin that is extruded from certain botanical sources such as Fabaceae and Araucariaceae: the samples used in this research. This resin is different from sap, which transports a solution of minerals and nutrients used to produce food for plants growth [32]. Resin is a liquid mixture of terpenoid and/or phenolic compounds, that exudes from a plant as a defensive measure against damage, whether due to disease or physical harm [33]. Different plants will secrete different compositions of resin, creating a basis for amber classification. As these resins are exposed to air and sunlight, the polymerization process begins [34]. When this resin becomes buried in sediment, where multiple factors such as temperature and pressure begin to affect the polymerization and chemical transformation process, the resin effectively begins to fossilize, also known as amberization. This chemical transformation can take place over millions of years, but there is currently no set period as to when resin has polymerized [35]. The polymerization process is what is responsible for trapping materials, organic and inorganic, within the amber. Any materials, crack, or void within polymerized amber is called an inclusion.

2.3.1 Inclusion Detection and Birefringence Imaging

Since inclusions in amber are not mineralized versions of the original entrapment such as other fossil types, study of the inclusions can lead to accurate conclusions about the palaeobotanical information, ancient organisms, or early climate and environment depending on the specimen studied [36]. Before any observations or measurements can be taken using traditional evaluation techniques, the amber must be prepared by first removing

an encompassing opaque matrix to visually inspect for significant inclusions within the specimen. This process is not only extremely time consuming but more importantly can damage inclusions before they are discovered. Some amber is entirely opaque to visible light and cannot be visually screened. THz NDE is the perfect candidate to locate these inclusions within amber before opaque matrix removal and visual screening needs to be performed. THz NDE is safer and faster than the other most commonly used amber evaluation techniques such as X-ray imaging, Raman spectroscopy, infrared spectroscopy, and light microscopy [37]. There are very few examples of characterization or imaging of amber in the THz range, such as the research done by T. Sasaki, which only characterized one amber deposit's dielectric constants with no imaging [38]. If correctly implemented THz NDE can be used for inclusion detection, while also having the capability of creating 3D reconstructions of the amber specimens.

Outlined by Snell's law, a major problem that THz imaging faces is refraction at materials boundaries due to differences in refractive index. Index matching materials can be used to reduce this refraction allowing for more precise and accurate images. Index matching materials are usually liquids or gels that have a similar real refractive index to the object of interest. When submersed, the index matching material allows light to pass through from the index matching material into the sample with minimal reflection or refraction. This technique has been applied previously to THz imaging using liquid paraffin and benzocyclobutene (BCB) in attempt to create custom characterized index matching fluid for 2D and 3D imaging [39]–[41]. Applying this methodology to amber samples allows for faster and more accurate imaging of the specimen while also increasing the accuracy and decreasing the time needed for inclusion detection.

Since amber is extruded from plants, there is a flow associated with its creation. This flow, as the amber polymerizes over millions of years, will create a birefringence within the material due to varying levels of stress within the resin, creating what is known as a photoelastic material. This birefringence can aid in both the understanding of the origins of the amber as well as in the detection of inclusions since varying levels of birefringence are seen to encapsulate most inclusions, both in the visual and THz frequency ranges. Measuring the birefringence can also allow for the determination of the direction of the stress within the amber, which can further be used to obtain insight on the extrusion and origin of the amber measured.

2.4 Terahertz Spectroscopy and Imaging

2.4.1 System Overview and Configuration

To generate short quasi-single-cycle THz pulses, on the order of several picoseconds, a biased photoconductive antenna (PCA) emitter is illuminated with a short pulse of infrared light. This light, with higher photon energy than the bandgap of the antenna material, is used to generate electron-hole pairs within the semiconductor. In the presence of the applied electric field in the circuit, a transient current created by the acceleration of the photo-injected carriers generates a pulse of electromagnetic radiation in the THz frequency range, illustrated in Figure 2.1. The pulse of radiation is collected using a series of lenses into a collimated THz beam to be emitted from the transmitter.

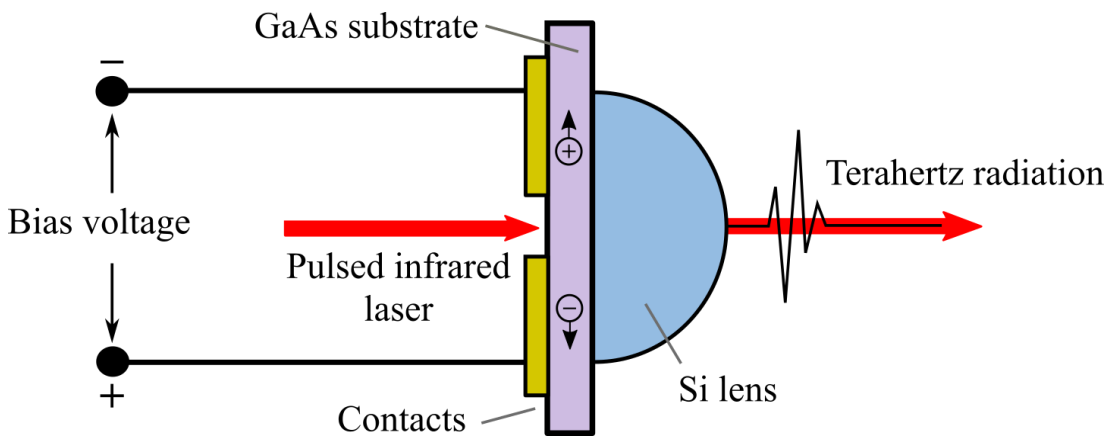

Figure 2.1 Photoconductive antenna emitter used to generate short quasi-single-cycle THz pulses.

The pulse is then focused back down onto a very similar PCA within the receiver after propagation. The detector does not have an external bias, because the incoming pulse induces a transient bias voltage across the gap in the antenna. Part of the laser pulse used in generation is sent to the detector through an optical delay line and focused onto the antenna, effectively turning on the receiver. When the incoming pulse and photocarrier impulse created by the laser overlap in time, a photocurrent that is proportional to the instantaneous antenna voltage, which is proportional to the strength of the THz electric field, is measurable. Sweeping the delay line allows for a temporal profile of the THz pulse to be measured and displayed. Since the electric field is directly measured in the time domain, the amplitude and phase information of the incident pulses can be measured. Further details of THz pulse generation and detection can be found in the following references [42], [43].

This research uses a TeraMetrix T-Ray 5000 Series Intelligent THz Control Unit as the main THz spectroscopy and imaging system. This system can produce up to 1000 individual THz waveforms per second. In the case of THz time domain spectroscopy, it

provides measurements of the THz electric field as opposed to its intensity as in other forms of THz detection, such as bolometer measurements [44]. Since the system measures the electric field of the THz pulse, all phase information is preserved including the real and imaginary parts of the wave.

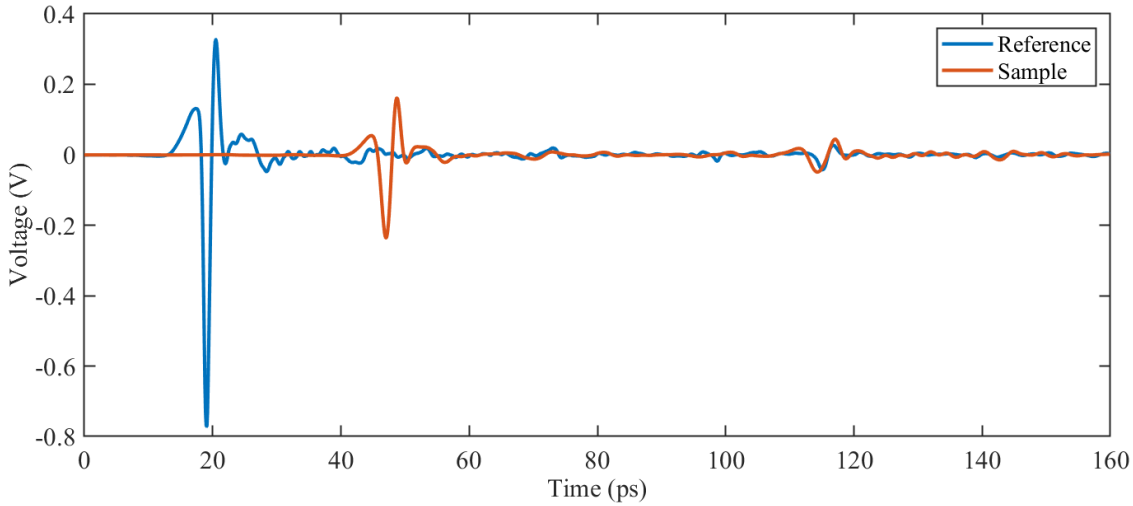

Figure 2.2 Example voltage data in the time domain showing the difference between the reference waveform (blue) and the waveform after transmission through a sample (orange).

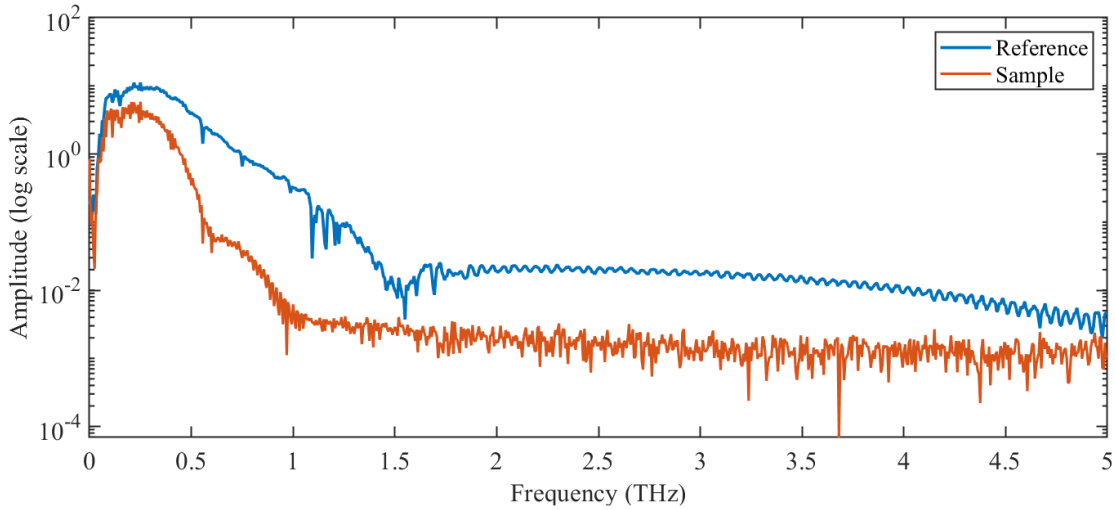

Figure 2.3 Example amplitude data in the frequency domain showing the difference between the reference waveform (blue) and the waveform after transmission through a sample (orange).

Analysis of the THz waves can be implemented in the time-domain, for example, by measuring the time delay a waveform or in the frequency domain via the Fourier transformation of the time versus THZ electric field measurements [2]. Example data showing reference and transmitted wavefroms in the time and frequency domains is shown in Figures 2.2 and 2.3.

2.4.1.1 System Configurations. The THz system can be setup in multiple different configurations to accommodate various applications. The most common setup for this research was a transmission-based setup. When the system is in a transmission setup, the transmitter and receiver face each other either 6 in or 12 in apart depending on the focal length of the 1.5 in diameter, high-density PE aspherical lenses being used. This allows for a maximum spot size of 17.1 mm at 100 GHz down to 1.1 mm at 1.5 THz. While in transmission, the object of interest is placed directly in the center of Gaussian beam within its depth-of-focus, which is two times the Raleigh range: the distance from the beam waist where the beam radius is increased by a factor of the square root of two. A spot measurement can be performed, or images can be created by using a "T-image" XY raster scan gantry. For THz CT, a LabVIEW controlled rotation stage is added to both the transmission and reflection setups in combination with the raster scanning gantry to create 3D reconstructions of 3D printed structures and amber samples.

The second most common system configuration used in this research is the reflection setup. In reflection, the transmitter and receiver are mounted to a collinear adapter to form a collinear reflection transceiver. This allows for the transmitter and receiver to share the same lens. In this configuration the object is placed either 3 in or 6 in forward of the transceiver's lens, allowing for the THz beam to reflect off the sample back

into the collinear adapter and into the receiver. This configuration permits for measurements of multi-layer stacks, spectroscopy of materials too thick for the THz waves to transmit through, as well as create images similar to in transmission mode using the raster scanning gantry.

For THz time-domain measurements in which the timing of the arrival of THz pulses needs to be accurately determined, the accuracy of the timing measurement is determined partially by the timing jitter of successive optical pulses which generate the THz pulses. The added noise of the timing jitter can be reduced by measuring the arrival time of a THz pulse relative to a reference pulse within the same time window. A common practice is to design the experimental configuration such that a reference pulse is included in the averaged analyzed waveform. An improvement to the THz system, an external reference mirror (ERM), is designed and fabricated to increase the precision of the THz peak arrival times, illustrated in Figure 2.4 and shown in Figure 2.5. This ERM allows for the creation of another THz reflection peak within the systems time window. With two trackable THz peaks within the time window, the system can track the arrival times of the reflected pulses off the sample more precisely using the mirror reflection peak arrival time as a reference. This additional peak is ideal for samples that are too thick to have both the front and back surface reflections within the time domain window. The ERM consists of a kinematic platform mounted mirror attached to a 3D printed linear rail structure for timing adjustment all mounted to the alternate unused port of the collinear adapter.

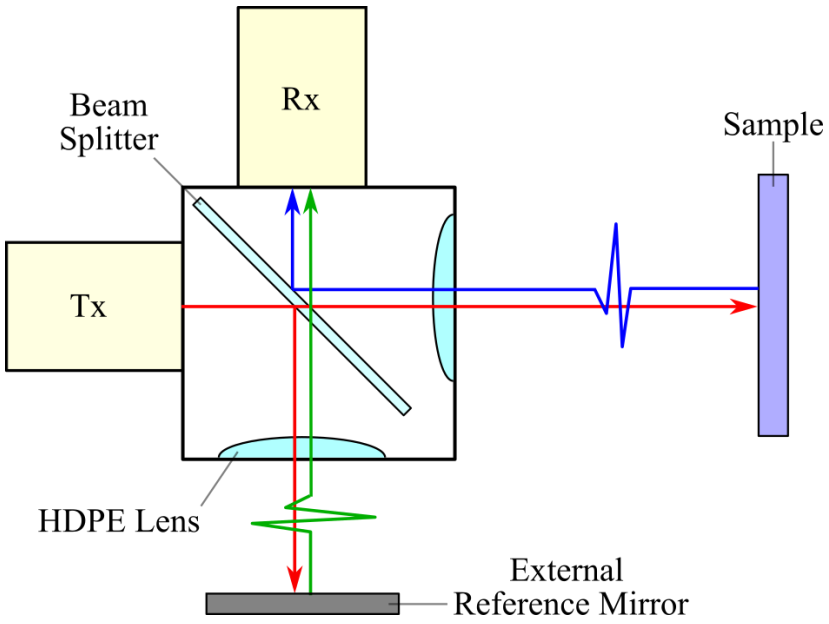

Figure 2.4 Illustration of collinear adapter with external reference mirror and resulting THz paths. The red path is incident pulse sent by the transmitter (Tx) split by the beam splitter. The green path is the reflected pulse from the reference mirror. The blue path is pulse reflected from the sample. The blue and green pulses arrive at the receiver (Rx) at different times, allowing the mirror pulse to be used as a reference within the resulting time window.

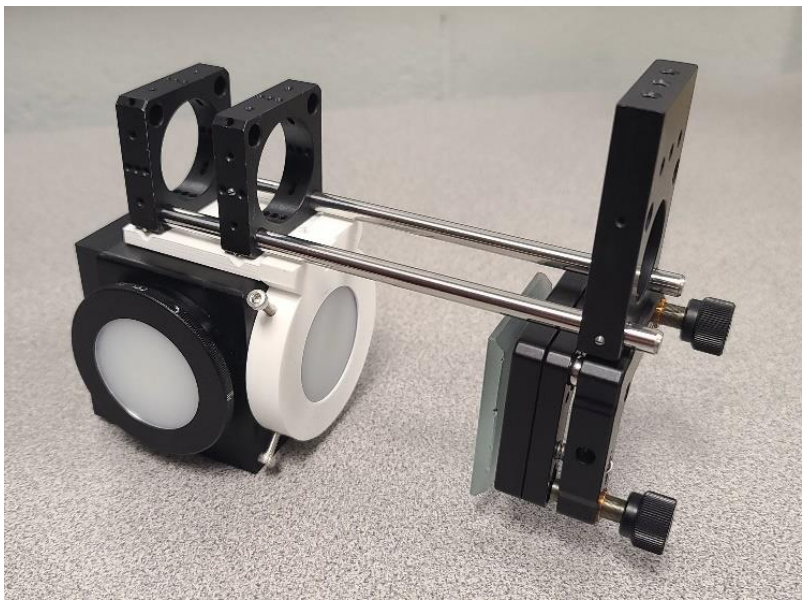

Figure 2.5 Custom external reference mirror (ERM) consisting of a 3D printed linear rail and adjustable mirror mounted to a collinear reflection transceiver to create a separate reference peak within the THz system's time window.

Birefringence measurements are successfully taken using the ERM and collinear adapter in combination with a free-standing wire grid linear polarizer with 10 µm wires and 25 µm period mounted to a LabVIEW automated rotation mount, illustrated in Figure 2.6. The increase in precision of the arrival times using the ERM allows for the measurement of birefringence in both 3D printed structures and amber samples in both transmission and reflection configurations. By measuring different polarization axes pulse arrival times, the level of birefringence in the samples is calculated.

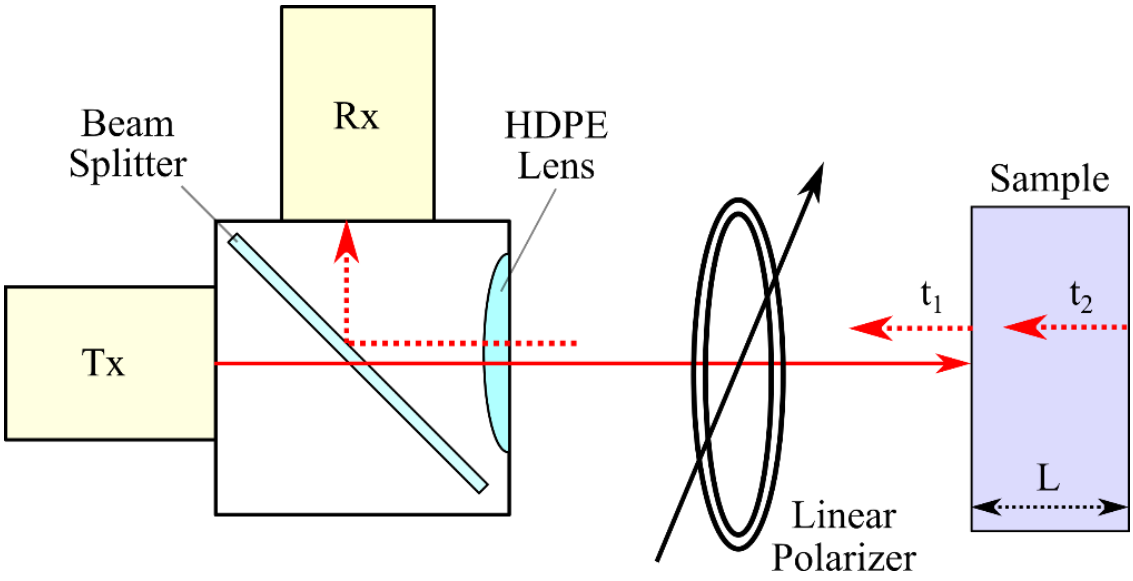

Figure 2.6 Illustration of collinear adapter with linear polarizer in the beam path. The solid red path is incident pulse sent by the transmitter (Tx). The dotted red paths are the reflected pulses from the front (t_1) and back (t_2) surfaces of the sample.

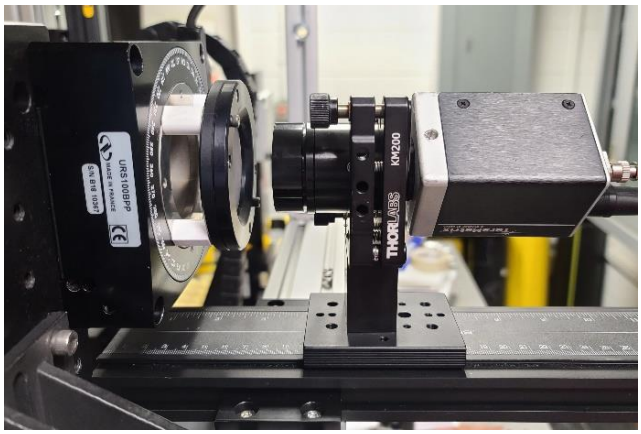

Figure 2.7 A linear wire grid polarizer mounted to LabVIEW controlled rotation mount in front of the T-ray 5000 transmitter configured in a transmission setup.

2.4.2 Optical and Physical Parameter Characterization

The T-ray 5000 saves individual averaged waveforms as PICOTD files, which are time domain waveform files in the style of a text document containing two columns corresponding to the measured voltages at 0.1 picosecond intervals over the course of the 160 ps time window. By taking the discrete Fourier transform (DFT) of these voltages, using a Fast Fourier Transform (FFT) algorithm, the time domain data can be represented in the frequency domain for analysis, like shown previously in Figure 2.3.

2.4.2.1 Complex Refractive Index, Transmission Coefficient, Attenuation Coefficient, Relative Permittivity, and Birefringence Magnitude and Direction Extraction.

For calculation of the complex refractive index of a material while considering the samples' thickness, three THz waveforms are required: an averaged sample waveform, a reference waveform, and a background waveform. The time-domain waveform data is converted to the frequency domain via a Fourier transform to calculate both the real and imaginary parts of the refractive index as a function of frequency. The phase angles as a function of frequency are calculated for both the averaged sample and reference waveforms using the

"angle" and "unwrap" functions in MALTAB to eliminate larger than π angle jumps. Due to the nature of the unwrap function, the resulting phase difference calculation does not always approach zero at 0 Hz. To rectify this, the slope of the resulting phase difference is calculated, and if the difference did not approach zero, a position adjustment in multiples of π are added to or subtracted from the phase difference to correct this. Once the phase difference approaches zero, it is used to calculate the frequency dependent real refractive index ($n_r(\nu)$) using the relationship

$$n_r(\nu) = 1 + \frac{c\Delta\phi(\nu)}{2\pi L\nu} \tag{2.1}$$

where c is the speed of light, $\Delta\phi(\nu)$ is the frequency dependent phase difference between the waveforms, L is the thickness of the sample measured, and ν is the frequency. Once the frequency-dependent real refractive index is calculated, it is possible to select a specific frequency at which to compare the real refractive indices.

Since the samples in this research are relatively transparent in the THz frequency range, the imaginary refractive index is small compared to the real refractive index. In this situation, the measured amplitude of the transmitted THz Fourier transform can be corrected for Fresnel reflection losses at the air-sample and sample-air interfaces [45]. The imaginary refractive index can be calculated while simultaneously be corrected for losses as the boundaries using

$$n_i = \frac{c}{2\pi\nu L} ln\left(\frac{|E_R(\nu)|}{|E_S(\nu)|} t_{12}t_{21}\right) \tag{2.2}$$

where $|E_R(\nu)|$ and $|E_S(\nu)|$ represent the magnitudes of the DFT of the electric field voltage measurements of the reference and sample waveforms, respectively. The Fresnel transmission coefficients at normal incidence between air and the sample and the sample and air are represented by t_{12} and t_{21} and are calculated using

$$t_{12}(\nu) = 2/\big(1 + n_r(\nu)\big) \tag{2.3}$$

and

$$t_{21}(\nu) = 2n_r(\nu)/(n_r(\nu) + 1). \tag{2.4}$$

Using the resulting corrected imaginary refractive index, the attenuation coefficient is given by

$$\alpha = 2\pi\nu n_i/c. \tag{2.5}$$

Birefringence induces a relative phase difference between beams polarized perpendicular to one another transmitted through a sample [46]. It can therefore be straightforwardly measured in an experiment like that employed to measure sample thickness. By comparing two linear polarization measurements perpendicular to one another, a difference in the time-of-flight of THz pulse reflections off the front and back surface of the sample can be measured. Thus, it is possible to measure the birefringence

within a material, whether intrinsic or induced. To present a normalized level of birefringence, $\frac{\Delta n}{n}$ was calculated by

$$\frac{\Delta n}{n} = \frac{t_2 - t_1}{\left(\frac{t_1 + t_2}{2}\right)} \tag{2.6}$$

where t_1 and t_2 are the timing differences between the front and back surface reflections received at the detector at the two perpendicular polarizations. In the denominator, the times t_1 and t_2 must be measured relative to the arrival time of a reference pulse with no sample present. This birefringence measurement is composed of the difference in the refractive indices between the two principal axes divided by the average refractive index. This representation allows for a birefringence measurement that is independent of the thickness of the sample and solely dependent on the birefringent properties of the material. The smaller the value of $\frac{\Delta n}{n}$, the smaller the birefringence present within the material.

Also, by measuring the time delay $\Delta t = t_2 - t_1$ between the arrival of the two pulses off the front and back surface of the sample, if thickness is known, the related refractive index experienced by the THz pulse within the sample can be calculated using

$$n(\theta) = \frac{c_o(t_2 - t_1)}{2L} = \frac{c_o}{2L}\Delta t \tag{2.7}$$

where c_o is the speed of light in a vacuum and L is the thickness of the sample at the measured position.

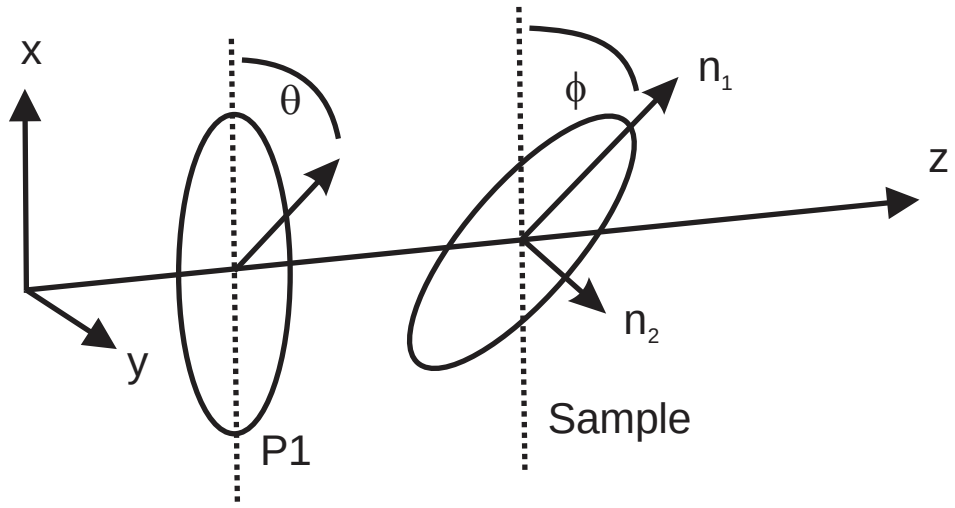

Figure 2.8 Diagram of the polarization geometry and relative orientation of principle stress axes. The incident light is travelling in the Z direction. The transmission axis of polarizer P1 is oriented at a rotation angle θ with respect to the X axis. The sample is described by two principal axes corresponding to a refractive index n_1 along one axis and a refractive index n_2 along an orthogonal axis. The rotation angle φ denotes the orientation of the sample's n_1 axis relative to the X axis.

To determine the stress direction within a material from THz birefringence measurements, geometry shown in Figure 2.8 is used. The incident THz pulse propagates in the z direction. Polarizer P1 defines the angle θ of the incident THz pulse's linear polarization relative to the *x* axis. The angle between the principle refractive index axis n_1 is at an angle ϕ with respect to the *x* axis. Following the theoretical analysis for an optical uniaxial crystal [47], for which the birefringence is caused by intrinsic stress in one direction in the x-y plane, the refractive index as experience by the THz pulse is

$$n(\theta-\phi)=\frac{n_1 n_2}{\left(n_1^2\,sin^2(\theta-\phi)+n_2^2\,cos^2(\theta-\phi)\right)^{1/2}}\,. \tag{2.8}$$

To extract the strength of the birefringence as well as the direction of the intrinsic stress, measurements of the pulse arrival times are required for incident THz pulses

launched with linear polarization in the x direction (i.e., θ=0), the y direction (i.e., θ=$\pi/2$), and θ=$\pi/4$. The corresponding refractive indices experienced by the three different THz polarization angles are then

$$n_x = n(0-\phi) = \frac{n_1 n_2}{\left(n_1^2\, sin^2\,\phi + n_2^2\, cos^2\,\phi\right)^{1/2}}\,, \tag{2.9}$$

$$n_y = n(\pi/2-\phi) = \frac{n_1 n_2}{\left(n_1^2\, cos^2\,\phi + n_2^2\, sin^2\,\phi\right)^{1/2}}\,, \tag{2.10}$$

and

$$n_{\pi/4} = n(\pi/4-\phi) = \frac{\sqrt{2}n_1 n_2}{\left(n_1^2(cos\,\phi - sin\,\phi)^2 + n_2^2(cos\,\phi + sin\,\phi)^2\right)^{1/2}}\,. \tag{2.11}$$

By measuring n_x, n_y, and $n_{\pi/4}$, one can in principle use these equations to determine n_1, n_2, and ϕ.

2.4.2.2 Sample Thickness Measurements Using an External Reference Structure.

The thickness of a sample is key to accurately measuring the optical parameters just mentioned. Thickness of the FDM 3D printed samples in this research is determined from time-of-flight (ToF) delay measurements [48] using an external reference structure (ERS). An ERS consists of a partially reflecting surface and a metal surface as a reflector. When a THz pulse interacts with the structure, two main pulses are reflected: one reflection from the backside of the partially reflecting surface and one from the front of the metal. The ToF difference in the arrival time of the two pulses yields an accurate measurement of the distance between the backside of the partially reflecting surface and the front face of the metal. Figure 2.9a illustrates the arrival time of pulses, ${t_1}^o$ and ${t_4}^o$, with no sample present.

The distance between the backside of the reference surface and the front surface of the metal is calculated using ToF to be

$$L_{14} = c_o(t_4{}^o - t_1{}^o)/2. \tag{2.12}$$

Since the THz pulse reflected from the metal transmits through the distance L_{14} twice, the factor of two in the denominator is present. When the sample is inserted into the structure, four major peaks are created and measured in the resulting waveform. Based on the maximum amplitude of each peak, the arrival times of the four peaks t_1, t_2, t_3, and t_4 are measured. The distances L_{12} and L_{34}, which are calculated from the ToF measurements of the pulses, can be subtracted from L_{14} to determine the sample thickness *L* independent of the refractive index of the sample, shown in Figure 2.9b. Thickness *L* measured using the propagation time of THz pulses is more accurate than using other methods of measurement such as calipers. *L* was then calculated using

$$L = L_{14} - L_{12} - L_{34} = \frac{c_o}{2}[(t_4{}^o - t_1{}^o) - (t_2 - t_1) - (t_4 - t_3)]. \tag{2.13}$$

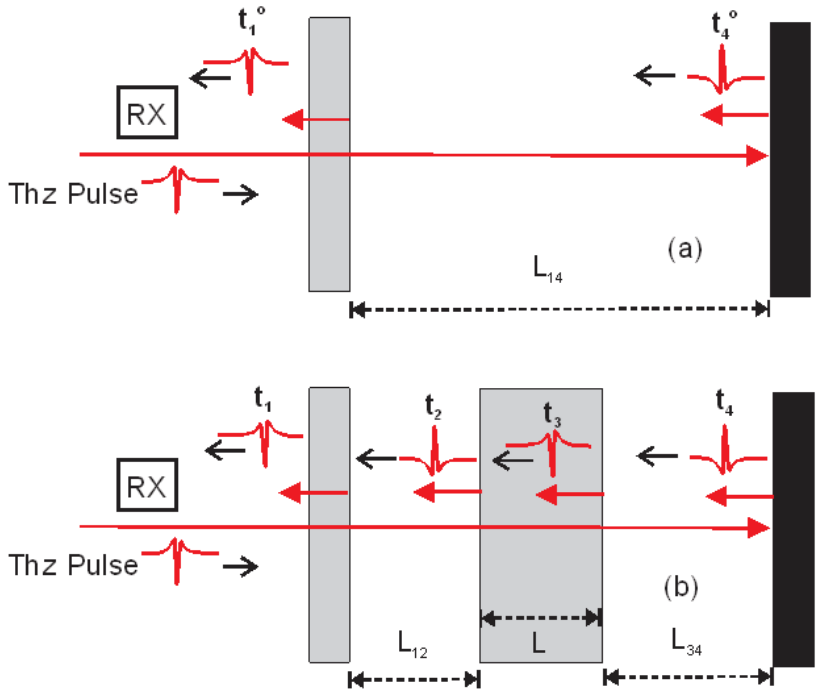

Figure 2.9 Illustration of the external reference structure (ERS) for simultaneous determination of sample thickness. a) Configuration for determining distance L_{14} in the absence of sample. b) Illustration of reflected pulses from the back surface of the reference surface, front surface of the sample, back surface of the sample, and reflecting metal mirror. *Source:* [49].

A specifically designed ERS was 3D printed to correctly hold the FDM 3D printed samples, designed after the ToF methodology illustrated in Figure 2.9. The tube structure attached directly to the collinear adapter output lens, as seen in Figure 2.10. An uncoated silica parallel window is used as the front reference surface. A polished aluminum disc acts as the mirror, placed at the focal point to allow for maximum reflected amplitude. The structure is designed and fabricated in such a way that it could be easily disassembled allowing each component to be swapped for accommodating different sample holders and partially reflecting surfaces depending on the application.

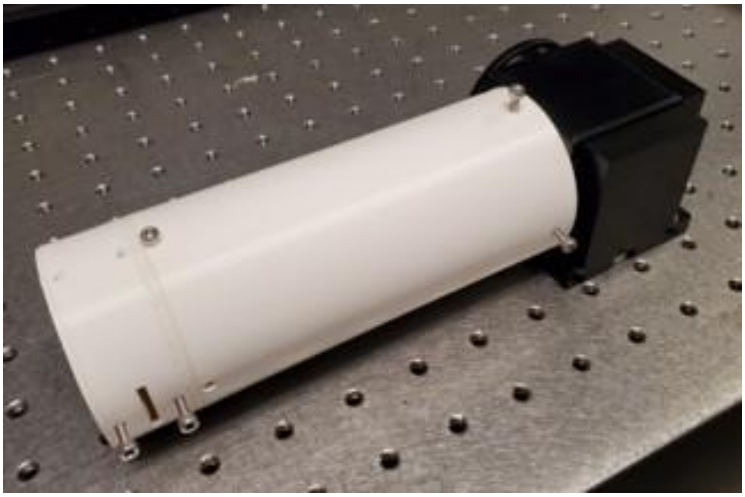

Figure 2.10 External reference structure (ERS) attached to a collinear adapter used for thickness measurements of FDM 3D printed samples.

2.4.3 Imaging and Tomography Techniques

Line scans or images can be taken using the XY raster scanning gantry. Since this THz time-domain spectrometer has a single transmitter/receiver pair, images are generated one pixel at a time by translating the sample in the XY plane through the focused THz beam, while recording averaged transmitted waveforms. Depending on the size of the structure being scanned, pixel size is determined by speed of platform translation and number of requested waveforms averaged per pixel. Each pixel in the resulting line scan or image is represented by both an averaged time domain waveform as well as a single output variable. These output variables are determined by "recipes" that are created based on the application. The recipes use deconvolution of the waveform to be able to measure and calculate values such as time between peaks or average amplitude over a certain frequency range. The more waveforms that are averaged per pixel, the more accurate the resulting output variable will be.

The system outputs these images as PICOIMAGE files which contain a compressed version of all the individual waveforms that make up that scan or image. The PICOIMAGE files are processed by a proprietary software called an API extractor. This extracts the individual waveforms into a CSV file containing the voltage measurements for each of the averaged waveform making up each pixel of the resulting image. A separate CSV output file is created for each output variable denoted in the recipe dependent on the application.

Using a series of line scans in combination with angular rotation of the sample a set number of degrees, THz CT images can be created. THz CT is similar to that of X-ray CT: the transmission, or any other optical property, is measured along a ray path through the object being scanned. In X-ray CT, pre-patient collimators are used to direct and correct the shape of the beam, so that only the necessary radiation passes through the patient and onto the active detector array [50]. In THz CT, the beam exiting the transmitter propagates through a high-density polyethylene aspherical lens. This lens focuses the gaussian beam down to a point where the sample being measured is within the depth-of-focus of the resulting beam. Each pixel size is determined by a combination of the XY translation speed and waveform averaging algorithm used for that scan.

The line scans, which are a collection of measurements along parallel ray paths, is called a projection measurement when used for CT. A projection measurement is a set of line integrals that represent the interaction between the THz radiation and the medium represented by a 2D function $f(x,y)$ that it interacts with and transmits through along one axis of measurement, illustrated in Figure 2.11. This measurement can be any measured optical parameter such as peak-to-peak THz pulse height, the time-delay of the THz pulse, transmission within a THz spectral band, or absorption within a specified frequency range.

These projection measurements are the main source of data for the tomographic reconstruction. Instead of performing a singular projection measurement for each angular rotation, a full 2D THz image is acquired at each angle, and then split into individual line scans based on the tomographic slice being reconstructed. This allows for faster full object reconstruction. In X-ray CT the gantry is rotated while in THz CT our sample is rotated using an indexed rotation stage controlled through a LabVIEW program.

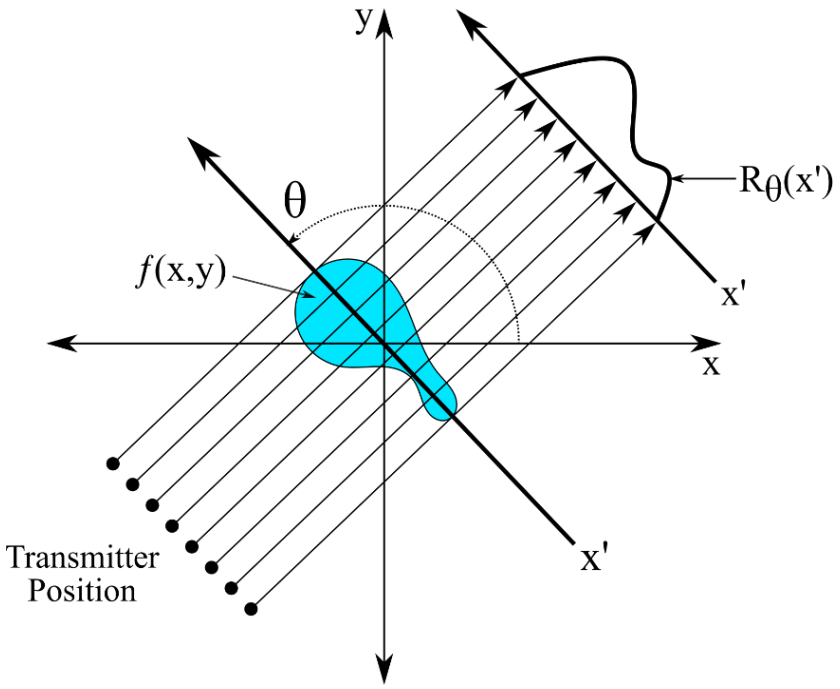

Figure 2.11 Illustration of a parallel beam projection measurement where $f(x,y)$ is the two-dimensional (2D) function representing the sample and $R_\theta(x')$ is the resulting projection measured at angle θ.

For proper tomographic reconstruction, it is crucial to find the center of rotation of the experimental setup. This is done premeasurement by using a thin metal rod of known diameter to obstruct the THz pulses from the receiver, allowing for the center of rotation position to be recorded. Once the center of rotation is found, the sample is rotated, and a

2D image is created at every set angle by measuring and calculating a chosen optical property of the sample or waveform attribute

A Radon transformation is a linear operator used to take a known function f in a 2D coordinate plane and represent it in what is known as the projection domain. A projection of an object can effectively be represented by the sum of several sine waves. At each Y value, a set of projections from discrete angles is then formed into a 2D representation of the object in the projection domain known as a sinogram [51]. A sinogram is essentially a stack of projection measurements that can be used to construct a tomographic image of the structure that was scanned.

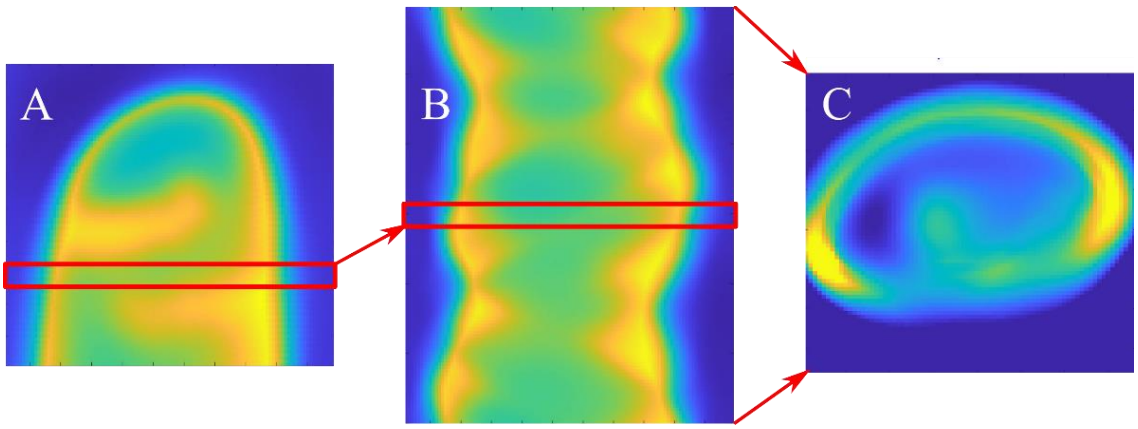

Figure 2.12 Example data for creating a tomographic image. (A) Transmission image of the scaled minimum waveform voltage at a singular θ value. Red box denotes a singular Y value line scan that will be taken from each θ angle to be assembled into a sinogram. (B) The resulting sinogram or collection of line scans of a certain Y value. (C) The resulting tomographic image after the sinogram is put through the inverse Radon transformation.

Going from the sinogram measurements to a reconstructed tomographic image is an inverse problem. These sinogram measurements can be used in various reconstruction methods such as the standard filtered back-projection (FBP) algorithm or iterative techniques such as the algebraic reconstruction technique (ART) or an even faster

simultaneous algebraic reconstruction technique (SART) to create 2D tomographic images or “slices” of the object [12], [52]. These slices are a top-down view of the selected plane through the object scanned. Iterative reconstruction methods generally result in more accurate reconstructions but require much more computational power and time. By stacking these tomographic images and utilizing reconstruction software such as ImageJ or 3D Slicer, it is possible to create a 3D reconstruction of the structure scanned based on the chosen optical property or waveform attribute that was measured.

CHAPTER 3

3D PRINTED SAMPLE IMAGING, CHARACTERIZATION, AND EVALUATION

3.1 Materials and Methods

3.1.1 Fused Deposition Modeling (FDM)

Fused Deposition Modeling (FDM) samples are printed using an Ultimaker S5 FDM 3D printer, a widely used commercially available printer controlled by G-code generated by Ultimaker Cura V4.4.1. Each sample is printed using a custom STL model designed in Autodesk Fusion 360. The filament materials used are copolyester (CPE), Nylon, polycarbonate (PC), polylactic acid (PLA), and polypropylene (PP): a comprehensive list of the available clear or natural filaments produced by Ultimaker that are compatible with the Ultimaker S5 3D printer. Clear and natural filaments were chosen to avoid the possibility of variations induced by pigments or dyes in the filament that might affect the THz measurements and resulting optical characteristics.

These filaments are thermosoftening polymers, or thermoplastics. Upon heating, these filaments are melted to a point where they can be reshaped, molded, or extruded. Once cooled down, the material will hold its resultant shape due to the chemically independent macromolecules within. This process of heating and cooling can be repeated with minimal damage to the material [53]. These different thermoplastic filaments are the building blocks of FDM printing. More information on FDM 3D printing can be found at the following reference [54].

3.1.1.1 Samples for Measuring the Refractive Index, Attenuation Coefficient, and Birefringence based on 3D Printing Parameters. Samples were designed to measure 20 x 106 x 2 mm, a size large enough to allow measurements to be taken at a variety of locations on each, as well as let ample THz radiation through to obtain proper signal-to-noise ratios, while keeping printing time to a minimum. Depending on the print parameters, each sample took roughly one hour to print. Each sample is measured at three separate locations denoted by the labels A, B, and C corresponding to the tic marks incorporated into the design, as shown in Figure 3.1. The other four tic marks are used for mounting reproducibility. This allows for consistent measurements for both the thickness of the sample as well as the refractive index, attenuation coefficient, and birefringence at those three locations.

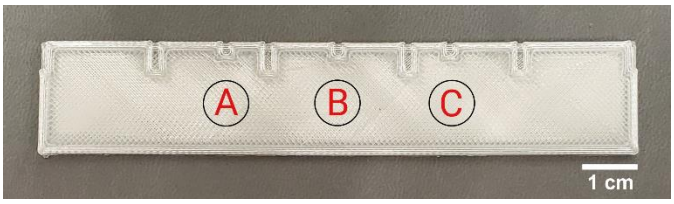

Figure 3.1 3D printed sample used for refractive index, attenuation coefficient and birefringence measurements dependent on printing parameters. Spots A, B, and C correspond to three measurement locations and with circles representing the average THz beam size.
Source: [49].

It is common in FDM printing for designs to vary from one another in their choices of infill percentage, printer nozzle size, print layer height and print orientation. The infill percentage is the amount of repeating structure printed within the object to create strength and rigidity. Generally, a printed structures strength is increased with an increase in infill percentage due to the increase in the amount of plastic extruded. For this research, 100 %

infill is used throughout to eliminate that variability. The effect of nozzle size, layer height, and print orientation on measured THz optical parameters is the primary emphasis of this research.

Most commercially available 3D printers can swap between a variety of nozzle sizes. The nozzle size, usually between 0.25 mm and 1.5 mm, determines the size of the individual print lines within the raster pattern: the repeating pattern of parallel lines that are combined to create a 3D object employed in the printing process. Nozzle sizes of 0.4 mm and 0.8 mm are used in this research. Nozzle size is important for printing THz components because roughness and boundaries on the printed structure will be created differently both on the surface and internally that may affect the optical properties of the structure and may need to be removed during a post-printing-process procedure, such as polishing [55].

The layer height of a print is the thickness of the individual layers laid down by the nozzle during each raster pass. Layer heights have limitations based on the nozzle size utilized, so layer heights of 0.1 mm, 0.2 mm and 0.3 mm are used because of nozzle size choice in this research. The layers throughout the structure will be extruded on a certain plane depending on the object's orientation. Horizontal and vertical print orientations are tested, as shown in Figure 3.2. When the vertical samples were printed a thicker region routinely formed at the bottom as a consequence of this printing orientation due to spreading of the material on the build plate. This had no effect on the measurements reported because that thicker part of the sample was not within the regions measured. The THz beam is always perpendicular to the front face of the sample during the THz transmission measurements. A set of standard printing parameters is established for

uniformity between filaments. The parameters chosen were a 0.4 mm nozzle, 0.2 mm layer height, a horizontal printing orientation, and Cura recommended heat and speed settings based on the filament used for that sample. The printing speed and temperature of the nozzle and build plate utilized are those recommended by the filament and printer manufacturer for optimal printing results [49].

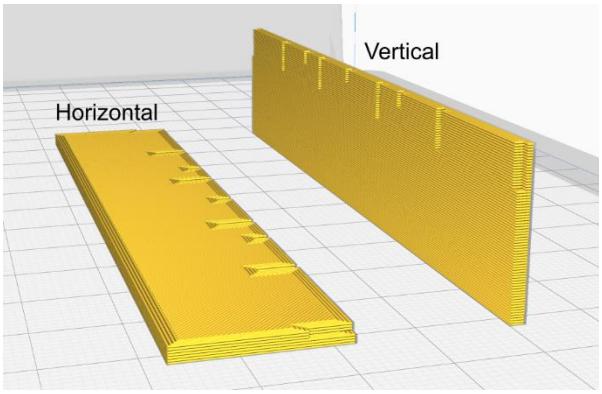

Figure 3.2 Computer-aided design (CAD) models showing the difference in print orientation for the FDM 3D printed samples. (Left) "Horizontal" orientation. (Right) "Vertical" orientation.
Source: [49].

3.1.1.2 FDM Samples for THz CT. Cylindrical structure samples were designed and printed for the initial trial of THz CT, shown in Figure 3.3, using Autodesk Fusion 360. The samples include two white PLA cylindrical structures measuring 1 cm and 2 cm in diameter, respectively. The other sample is an 8 mm wide increasing to 28 mm wide by 3 cm tall six tier cylindrical structure with a 4 mm hole throughout the height. Cylindrical structures are chosen for the initial measurements for their simplicity in the tomographic reconstruction using the inverse Radon transformation.

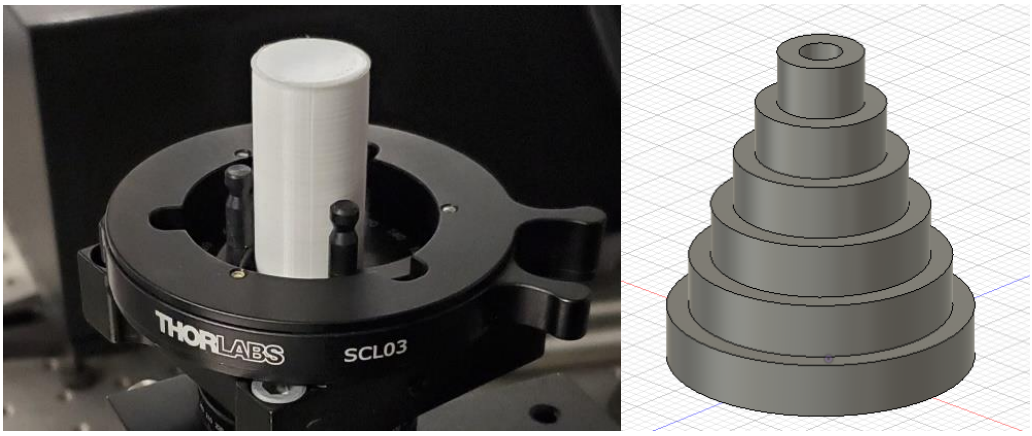

Figure 3.3 Samples used for THz CT and 3D reconstruction of 3D printed structures. (Left) 2 cm diameter 3D printer cylinder mounted in a LabVIEW controlled rotation stage. (Right) Autodesk Fusion 360 CAD model of a 28 mm wide by 3 cm tall six tier cylindrical structure with 4 mm uniform hole throughout.

3.1.2 Nanoparticle Jetting (NPJ)

All ceramic samples were fabricated using nanoparticle jetting, a proprietary printing technology developed by XJet, which falls under the category of binder jetting additive manufacturing. ZrO_2 nanoparticles are suspended in a polymer binder and carrier agent to form an ink that is deposited layer by layer on top of one another. As the multiple print nozzles deposit these layers of the ZrO_2 dispersion, as well as support structure material, the layers are dried using heat lamps and hot air dryers to evaporate the carrier agent. Once completed, the samples are submerged in water to dissolve the support material. After a period of drying in a desiccating chamber, the samples are considered green and ready for sintering. Sintering is required to join the individual ZrO_2 particles into one dense structure at temperatures above 1200 °C. During firing, the binder decomposes leaving voids of varying size depending on the maximum temperature reached.

3.1.2.1 Ceramic Samples for Relative Permittivity Measurements and Defect Detection. Cuboid ceramic samples were fabricated using an XJet Carmel 1400 printer. The samples provided were all printed with identical printing parameters, but experienced different maximum sintering temperatures varying from 750 °C to 1450 °C in increments of 100 °C. The samples were 50 mm^2, 2-3 mm thick, layer thicknesses of 10 μm, and a jetting resolution of roughly 20 μm. The ceramic samples characterized in this research were provided by Dr. Paul Parsons from the University of Delaware.

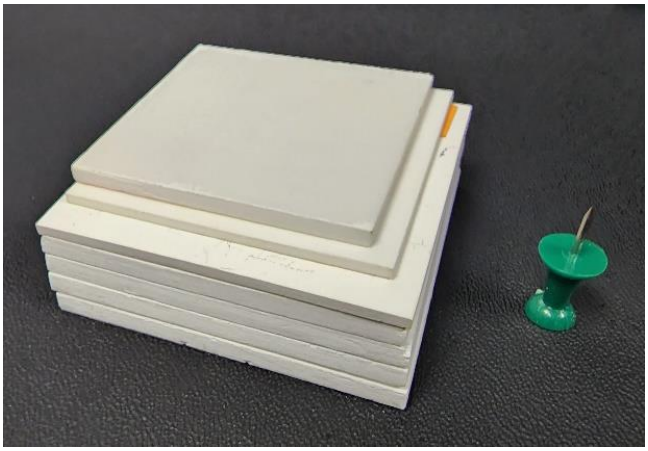

Figure 3.4 Stack of nanoparticle jetted ceramic samples varying in size and thickness due to their maximum sintering temperatures used for relative permittivity and dielectric constant measurements. The thumbtack is for size reference.

3.2 Results and Discussion

3.2.1 FDM 3D Printing Parameters

Refractive index, attenuation coefficient, and level of birefringence are measured for a set of 3D printed samples printed with various printing parameters. Changes in the optical properties of these printed structures are observed and compared.

3.2.1.1 Infill Correction. After the initial sample printing process, during visual inspection, the structures appeared more opaque than expected when printing with pigment free filaments. The non-transparent samples in the visible range lead to the investigation as to why this was occurring. To look at the internal structure of the samples, sacrificial samples are printed and cut. The cross sections are observed under a digital microscope. It was determined that due to the infill pattern and polymer extrusion amount set by Cura during slicing, the samples did not contain a true 100 % infill. To correct this under-extrusion issue, the extrusion percentage is increased to 105 %. This increase allowed for the slicing software to produce a true 100 % infill structure when printed with the different filaments. In Figure 3.5 where the pre-correction is shown on the left, clear gaps between the individual raster lines are visible, showing under extrusion. On the right, after the correction was implemented, true 100 % infill is obtained. Gaps are no longer visible in the cross section, and the samples have increased visual transparency due to the lack of air gaps between the raster lines, leading to less refraction. The infill percentage correction is used throughout the sample printing process for all filaments.

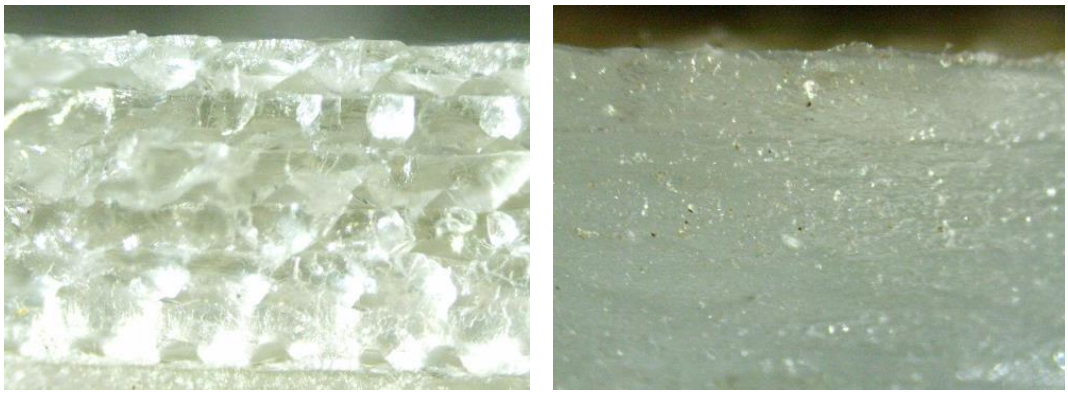

Figure 3.5 Digital microscope images of two cross sections of 3D printed samples. (Left) Sample before infill correction was implemented showing under extrusion. (Right) Sample after the infill correction was implemented showing true 100 % infill.

3.2.1.2 Uncertainty. When measuring optical properties and characteristics of materials, there will be an associated uncertainty. The data presented for comparison of printing parameters in Subsection 3.2.1.5 is characterized around 500 GHz. The uncertainty in the measured value of the real refractive index at 500 GHz is calculated by differentiating and squaring Equation (2.12) and then taking an ensemble average (noting that the covariance terms vanish). The uncertainty in the real refractive index is

$$\left(\frac{\sigma_{n_r}}{n_r - 1}\right)^2 = \left(\frac{\sigma_L}{L}\right)^2 + \left(\frac{\sigma_{\phi_s}}{\Delta\phi}\right)^2 + \left(\frac{\sigma_{\phi_r}}{\Delta\phi}\right)^2 \tag{3.1}$$

where the σ values refer to the standard deviations of the respective measured quantities. The uncertainty in the thickness L and phase difference $\Delta\phi$ is determined by performing the same measurement on a chosen sample ten times with 1000 waveform averages each. This allows for the calculation of the thickness and phase difference between the reference scan and sample scan ten times normalized using the central limit theorem. The thickness value L is determined by Equation (2.13) and its uncertainty by

$$\left(\frac{\sigma_L}{L}\right)^2 = \frac{\left((\sigma t_{14}^o)^2 + \sigma t_{12}^2 + \sigma t_{34}^2\right)}{(t_{14}^o - t_{12} - t_{34})^2}. \tag{3.2}$$

The uncertainty in the thickness measurements using the ERS is calculated to be 0.6 %. Propagation of errors using Equation (3.1) yields a relative uncertainty of 0.3 % for the frequency dependent real refractive index measurements at 500GHz. The attenuation coefficient measurement uncertainty is calculated to be 0.7 %. A similar propagation of

error analysis is followed for birefringence using Equation (2.6). This leads to a relative uncertainty of 2.7 % for the birefringence measurements. A 2σ threshold (95 % confidence interval) is used to determine if changes in refractive index, attenuation coefficient and birefringence resulting from variations in the printing parameters are statistically significant [49].

3.2.1.3 Refractive Index Decreases Below 200 GHz. The calculated refractive index below approximately 200 GHz for all samples is observed to drop off and decrease with frequency. Refractive index measurements on various bulk non-printed plastics are taken for comparison and this phenomenon is not observed as it was in the 3D printed samples. To investigate the refractive index drop off, samples are printed with varying thicknesses. Four samples are printed with the standard printing parameters but with thicknesses varying from 2 to 8 mm. The real refractive indices are calculated for these samples: the results are shown for frequencies below 0.25 THz. Figure 3.6 shows that the decrease below 200 GHz becomes successively less prominent as the thickness of the samples increases. This observation suggests that the surface roughness of the sample is responsible for this effect in the thin samples. The relative contribution of the surface roughness to the refractive index is much larger in the thinner sample and will decrease as the thickness increases. Since this drop off is only seen at the lower frequencies below 200 GHz, the majority of the frequency range measured for the samples is unaffected [49].

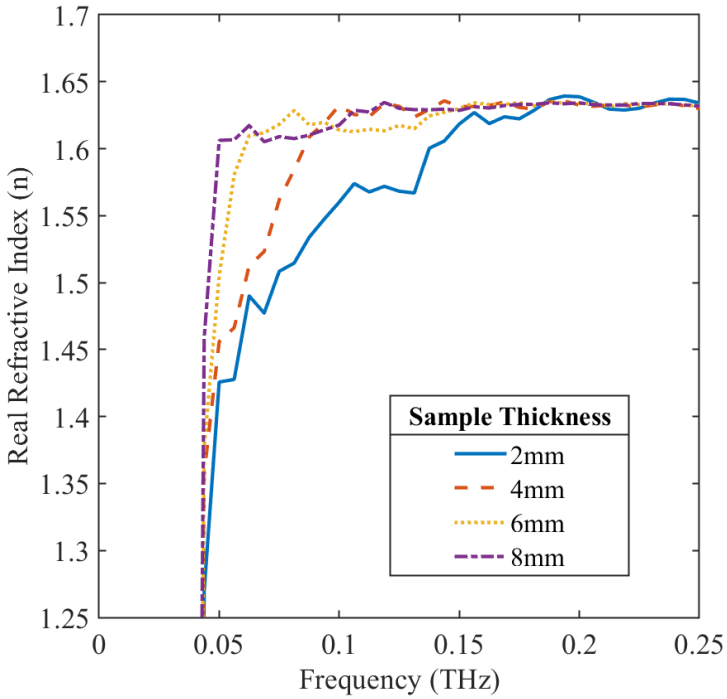

Figure 3.6 Extracted frequency-dependent real refractive index drop-off below 200 GHz. As the thickness of the printed samples increases, the effect decreases. Data below 0.05 THz is unreliable because of negligible detectable signal.
Source: [49]

3.2.1.4 Filament Comparison of Real Refractive Indices and Attenuation Coefficients.

Figures 3.7 and 3.8 show the frequency dependence of the real refractive indices and the attenuation coefficients of the five 3D printing filaments, respectively. Each sample is printed with the standard printing parameters described in Subsection 3.1.1.1 and characterized using the MATLAB code in Appendix A. The fluctuations in each curve are induced by Fabry-Pérot oscillations; the frequency interval between oscillations is consistent with the thickness of the measured samples. Of note is the extremely low value of polypropylene's attenuation coefficient. The presence of ranges within the curve that trend to an unphysical value below 0 cm^{-1} indicate that, to properly measure the extremely low attenuation coefficient of polypropylene within this frequency range, much thicker samples than the ones printed in this research would need to be fabricated. Consequently,

polypropylene's attenuation coefficients are omitted from the tables below. The attenuation coefficients for PLA and Nylon measured here agree with previously published results, as referenced in Table 2.1 [24]. Our PC measurement of refractive index was 0.1 higher than measured in Reference [27]. This could be due to a different chemical formulation of the filaments from differing manufacturers. CPE measurements for this frequency range have not been previously published.

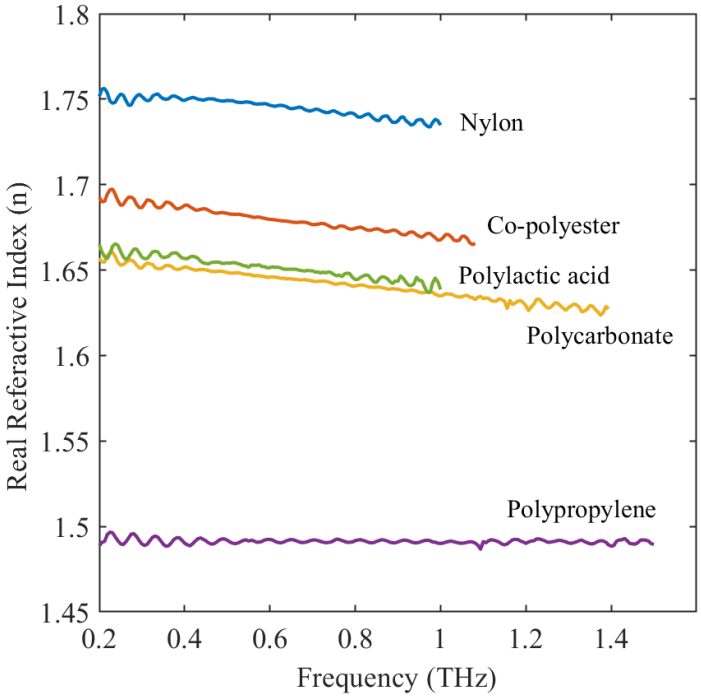

Figure 3.7 Extracted frequency dependent real refractive indices of the five 3D printing filaments used in this research.
Source: [49].

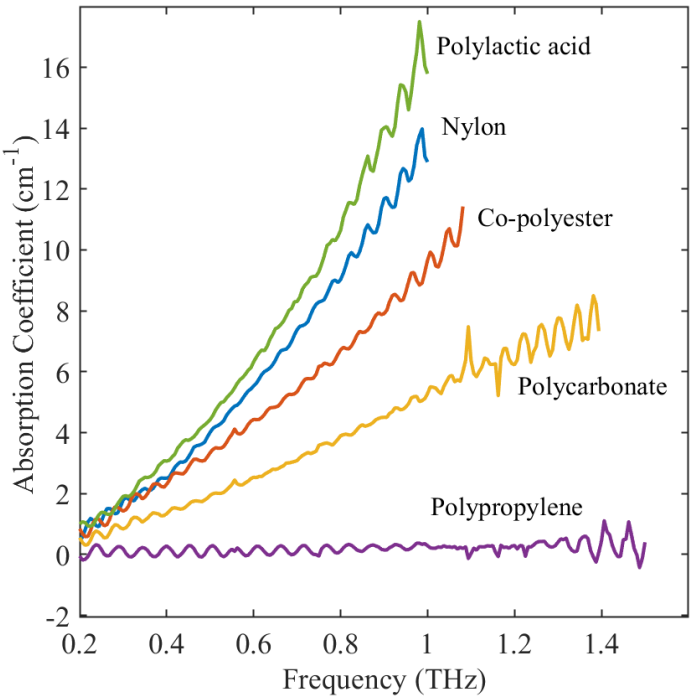

Figure 3.8 Extracted frequency-dependent attenuation coefficients of the five 3D printing filaments used in this research measured using electric field.
Source: [49].

3.2.1.5 Effect of Printing Parameters on Real Refractive Index and Attenuation Coefficient. The THz optical properties of the materials studied here have previously been demonstrated to be frequency dependent. We chose to isolate and quantify changes in the THz optical properties due to variations in printing parameters at a frequency of 500 GHz, chosen for its good signal-to-noise ratio and lack of interference oscillations in the measured data. Tables 3.1, 3.2, and 3.3 show the measured real refractive indices and attenuation coefficients for our samples as their printing parameters are varied. Cura recommended heat and speed settings are used for all printed samples.

Table 3.1 Real Refractive Indices and Attenuation Coefficients at 500 GHz Based on Variation in Printer's Nozzle Size

Filament Material	Nozzle Size (mm)	Real Refractive Index (n)	Attenuation Coefficient (cm^{-1})
PLA	0.4	1.654	4.429
	0.8	1.657	4.587
Nylon	0.4	1.749	4.015
	0.8	1.758	3.921
PC	0.4	1.649	1.944
	0.8	1.654	1.924
CPE	0.4	1.683	3.343
	0.8	1.691	3.461
PP	0.4	1.492	N/A
	0.8	1.495	N/A

Note: Standard printing parameters of a 0.2 mm layer height and a horizontal printing orientation were used. Uncertainties in the real refractive index: $2\sigma = \pm 0.010$ and attenuation coefficient: $2\sigma = \pm 0.025$.
Source: [49]

Table 3.2 Real Refractive Indices and Attenuation Coefficients at 500 GHz Based on Variation in the Print's Layer Height [49]

Filament Material	Layer Height (mm)	Real Refractive Index (n)	Attenuation Coefficient (cm^{-1})
PLA	0.1	1.658	4.455
	0.2	1.654	4.429
	0.3	1.641	4.543
Nylon	0.1	1.755	3.961
	0.2	1.749	4.015
	0.3	1.753	4.020
PC	0.1	1.663	2.104
	0.2	1.649	1.944
	0.3	1.663	2.123
CPE	0.1	1.689	3.161
	0.2	1.683	3.343
	0.3	1.670	3.675
PP	0.1	1.493	N/A
	0.2	1.492	N/A
	0.3	1.492	N/A

Note: Standard printing parameters of a 0.4 mm nozzle and a horizontal printing orientation were used. Uncertainties in the real refractive index: $2\sigma = \pm 0.010$ and attenuation coefficient: $2\sigma = \pm 0.025$.
Source: [49]

Table 3.3 Real Refractive Indices and Attenuation Coefficients of Samples at 500 GHz Based on Variation in Print Orientation [49]

Filament Material	Print Orientation	Real Refractive Index (n)	Attenuation Coefficient (cm^{-1})
PLA	horizontal	1.654	4.429
	vertical	1.604	5.092
Nylon	horizontal	1.749	4.015
	vertical	1.741	4.099
PC	horizontal	1.649	1.944
	vertical	1.623	2.444
CPE	horizontal	1.683	3.343
	vertical	1.650	3.191
PP	horizontal	1.492	N/A
	vertical	1.457	N/A

Note: Standard printing parameters of a 0.4 mm nozzle and 0.2 mm layer heights were used. Uncertainties in the real refractive index: $2\sigma = \pm 0.010$ and attenuation coefficient: $2\sigma = \pm 0.025$.
Source: [49]

As seen in Table 3.1, as the nozzle size on the printer is increased from 0.4 mm to 0.8 mm, there is a slight consistent increase in the real refractive index in every pair of samples: at an average of 0.33 %, this result is not statistically significant as this increase is within the uncertainty of the mean. The attenuation coefficients for PLA, nylon, and CPE were outside of the uncertainty, but no correlation could be drawn between a change in nozzle size and a change in attenuation coefficient. Therefore, the refractive indices and attenuation coefficients are not correlated with a change in nozzle size.

Table 3.2 shows the variations caused by changes in layer heights between the samples. Again, the differences measured in refractive index are within the uncertainty. Some materials experience slight increases, while others experience slight decreases, and there is no correlation between layer height and refractive index. Nor is there any correlation with the attenuation coefficients, even though some of the measurements lie outside of the calculated uncertainty. To further investigate this result, an additional set of

samples is printed, this time with a vertical print orientation rather than a horizontal print orientation. With the print orientation changed, there is still no correlation between layer height and the change in refractive index or attenuation coefficient observed.

Table 3.3 shows the variation based on changing the print orientation. There is a clear correlation between print orientation and change in refractive index: an average increase of 1.9 % in the real refractive index at 500 GHz when the samples are printed horizontally compared to vertically. Three of the four measurable attenuation coefficients have increases greater than the calculated uncertainty. Because air gaps might have caused to the change in refractive index, after the measurements are taken, the samples are cut and their cross sections are viewed using a light optical microscope (similar to the infill correction process), but no air gaps within the prints are discovered. It is plausible that the surface texture differences between the horizontal and vertical samples might cause these correlations. In a vertically printed sample, the THz beam is interacting with a repeating structure surface layer with features of similar size to its wavelength. It has been previously reported that increasing the surface roughness of various samples measured in the THz range has an increase in the uncertainty of thickness measurements as well as increase the measured values of real refractive indices [56], [57].

3.2.1.6 Effect of Printing Parameters on Birefringence. Horizontally printed samples show birefringence levels below the calculated uncertainty in the measurement. Vertically printed samples however, show birefringence levels above the uncertainty and are shown in the figures below. The lack of measurable birefringence in the horizontally printed samples is plausibly due to the cancellation of any induced stresses in the alternating raster pattern during printing because of the crosshatch pattern that is performed while printing

in this direction. This cross-hatch pattern is perpendicular to the THz beam during transmission, and therefore each opposing layers' stresses will be effectively nulled during the phase change. Shown below in Figures 3.9 and 3.10, as the layer height of the samples increases, using both a 0.4 mm and 0.8 mm nozzle, the birefringence present in the sample also increases. This trend is seen in every filament material.

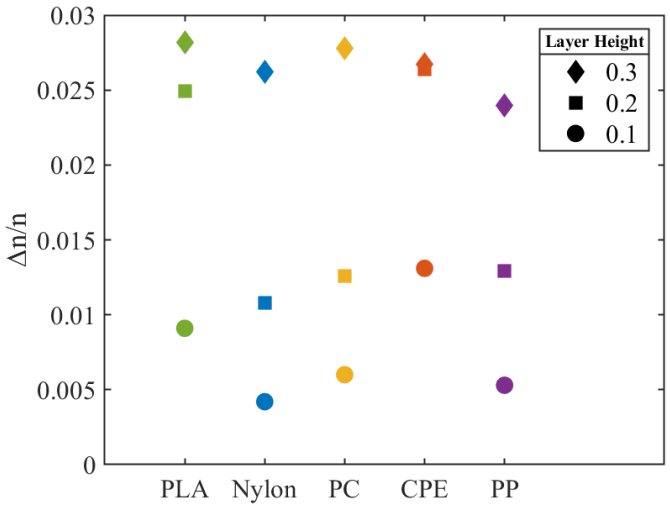

Figure 3.9 Level of birefringence ($\frac{\Delta n}{n}$) measured at 250 GHz in vertically printed samples using a 0.4 mm nozzle and standard printing parameters with variation of print layer height. *Source:* [49].

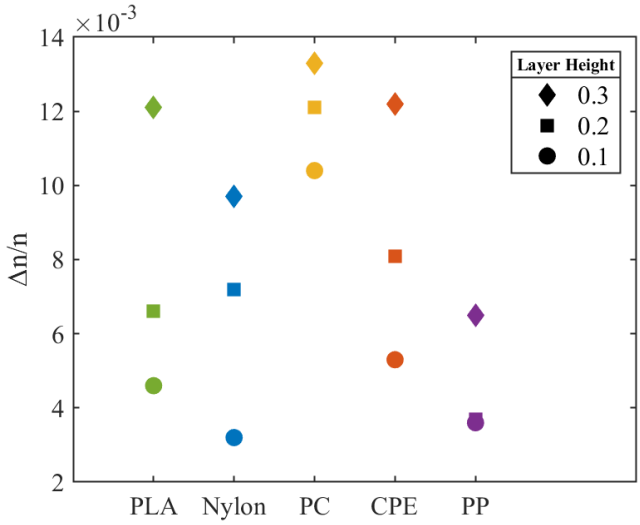

Figure 3.10 Level of birefringence ($\frac{\Delta n}{n}$) measured at 250 GHz in vertically printed samples using a 0.8 mm nozzle and standard printing parameters with variation of print layer height. *Source:* [49].

Additional stresses may be induced into the material as it is rapidly heated and cooled from printing temperature back to room temperature during the FDM 3D printing process. These large thermal fluctuations combined with forced extrusion could create a birefringence within the final structure as the layers are deposited on top of one another. As seen in Figures 3.9 and 3.10, the increase in nozzle size from 0.4 mm to 0.8 mm causes an average of 125 % decrease in birefringence. One possible explanation for this decrease is that with the larger nozzle size each layer of the sample is printed faster and, since each layer is printed faster, there is less elapsed time for that layer to cool, decreasing the introduction of residual stresses into the material due to thermal differences between layers. Consequential thermal differences between layers will create larger measurable birefringence, such as seen in the slower printing 0.4 mm nozzle samples [49].

3.2.2 FDM Tomography

Preliminary THz CT data is taken on the cylindrical and tier stacked 3D printed structures using an FBP algorithm, parallel beam projection data. and the MATLAB code that is in Appendix B. This code is written to take the resulting waveforms, convert the voltage measurements into frequency domain amplitude data, and average the corresponding amplitudes over the entire measured frequency range (min to max). This gives an average measured electric field as the beam passes through the sample at the different angles to be used for tomographic image and 3D structure reconstruction.

The code utilizes the built-in inverse Radon transformation (iRadon) function which assumes parallel beam projection data. This assumes that each line integral in the projection data is parallel to each other and that each pixel (i.e., averaged output waveform) corresponds to a singular summation on that line. This function allows for adjustment of

the back projection interpolation, and a choice of filter used for the frequency domain filtering. In these reconstructions, 'linear' (default) interpolation is used as no difference in the resulting reconstructions is observed. Optimal results are shown using the 'Ram-Lak' (default) filter with no frequency scaling.

3.2.2.1 Solid Cylinder Structures Tomography. The two samples imaged first are solid PLA cylinders with 1 cm and 2 cm diameters, respectively. Figure 3.11A has a lower resolution than Figure 3.11B due to the number of horizontal projection scans and angular rotations performed. Figure 3.11A was a 360-degree rotation scan comprised of a projection measurement taken every 12 °. Each horizontal projection contained 30 averaged waveforms (pixels) for a total of 900 individual waveforms taken to create the resulting tomographic image of the 1 cm cylinder. Figure 3.11B was also a 360-degree scan but comprised of 90 pixels per projection taken every 4 ° of rotation for a total of 8100 individual waveforms taken on the 2 cm cylinder.

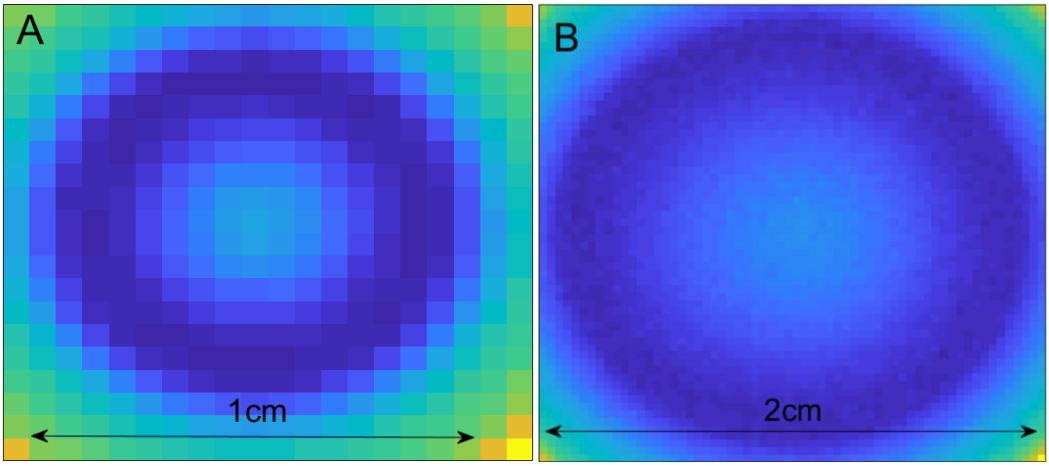

Figure 3.11 THz tomographic images of cylindrical structures. (A) 1 cm solid PLA cylinder tomographic image at 30x30 resolution. (B) 2 cm solid PLA cylinder tomographic image at 90x90 resolution.

The difference in tomographic resolution between the two scans is obvious, but both scans showcase the same resulting problem: clearly visible boundary effects in both images. These boundary effects are mainly caused by refraction as the THz both enters the plastic cylinder and again enters the air upon exit. This refraction is the reason the edge of the cylinders tomographic image is “soft” and not a sharp edge. Since the cylinder is a solid structure with consistent density and transparency to the THz beam throughout, the center of the tomographic slice should be the same color as the edges, denoting equal amplitude of the resulting electric field.

The centers of these images appear a lighter color due to beam hardening or cupping. Beam hardening effectively alters the attenuation profile so that the attenuation is projected as lower in the middle and increased along the edges, illustrated in Figure 3.12. The inverse radon transformation reconstruction perceives this as higher transparency due to the assumption of parallel beam projection measurements, hence the lighter color.

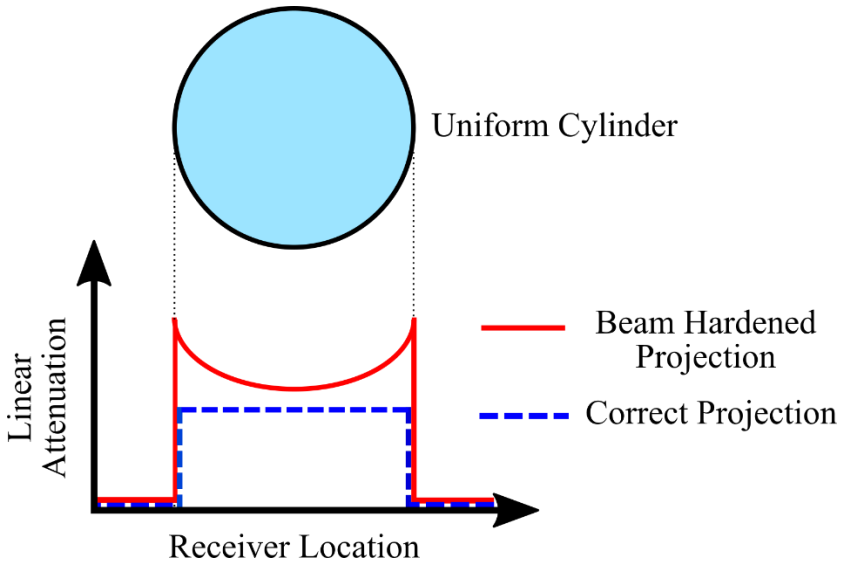

Figure 3.12 Illustration of the effect on the linear attenuation measurement projection of a uniform density cylinder due to beam hardening compared to a correct projection.

There is also an unmeasurable effect of beam deflection to the point that the THz beam is missing the detector completely due to the plastics strong refractive effect at these frequencies. The THz beam is so strongly refracted as it transmits through the cylinder, it does not pass through the second lens to be collimated into the receiver upon exit. This also contributes to the variation in the perceived attenuation due to the variable decrease in light received after transmission. Similar results have also been shown in THz tomography images of wine corks and foam blocks [12], [58].

3.2.2.2 Tier Stacked Structure Tomography and 3D Reconstruction. The tier stack structure with the hole throughout the height is imaged next. A total of 19 tomographic images are created, one every 0.5 mm vertically, to create a 3D reconstruction of a small section of the structure. Resulting tomographic images are created similar to that of the solid cylinder structures. Due to the uniform hole running through the center of the structure, there is a clear hole in the center of each tomographic image, as opposed to just a lighter intensity as seen with the solid structures. The issue presented is that this hole increases in size with increase in structure diameter even though the hole diameter does not change throughout the height. We can once again attribute this to the same conclusion as with the solid cylinders. Beam hardening and beam steering/deflection cause the reconstruction method to interpret the results as a decreased attenuation through the central portion of the structure, effectively increasing the perceptive size of the hole.

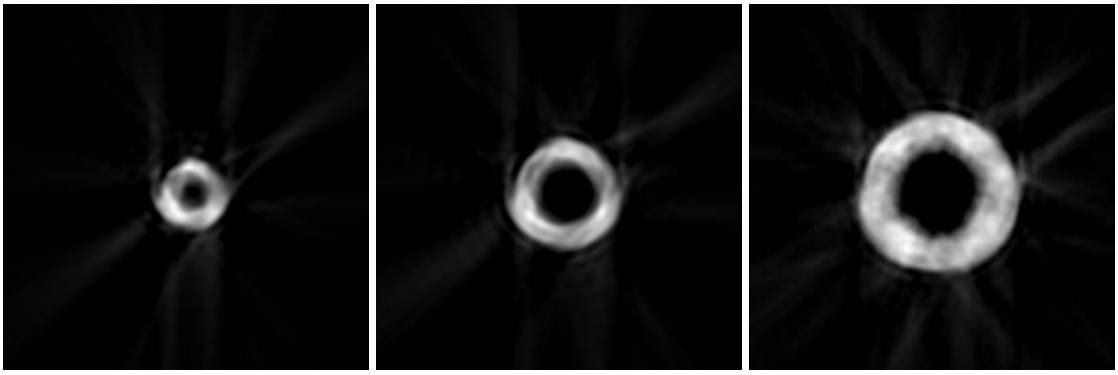

Figure 3.13 Tomographic images of the tier stack structure at three decreasing heights with clear signs of beam hardening and beam steering with refraction losses.

It is possible to adjust the resulting contrast boundaries of the image. This allows for removal of some stray artifacts in the resulting tomographic images, but also reduces the accuracy of the dimensions of the structure reconstruction. Throughout all tomographic images, there are repeating artifacts, specifically streaking, in the images. Artifacts like these are poor for reconstruction but do show consistency between the individual scans. The tomographic images are uploaded to ImageJ which is a Java based image processing software. Using the 3D Volume Viewer 2.0 plugin, a full 3D reconstruction is created using the 19 tomographic images.

Figure 3.14 shows what section of the tier stack model is scanned. A transmission image is included to show the image that was created at a singular θ value and to be compared to the central cross section of the 3D reconstruction. The hole grows larger as more material is transmitted through, and the beam hardening effect increases. This reconstruction does not visualize the differences in diameter between each tier on the outside of the structure, but instead reconstructs it as a gradually increasing structure while scanning towards the bottom, like an upside-down cone shape. This result can be caused by two issues with the experiment. First, due to the beam diameter, there are many resulting

artifacts caused by refraction. The beam could not be “seeing” the individual steps as different sections of the THz beam may be transmitting through different sizes tiers, resulting in an averaged value between the two. This consequence could also be greatly amplified if the structure was not properly within the depth-of-focus of the gaussian beam. Another probable cause for this is if the structure was not centered both on the rotation stage and within the horizontal scan axis. If not properly centered, this would cause an averaging of values horizontally as the structure was rotated throughput the scan. This averaging would visualize structure in the recreation that was not present on the print.

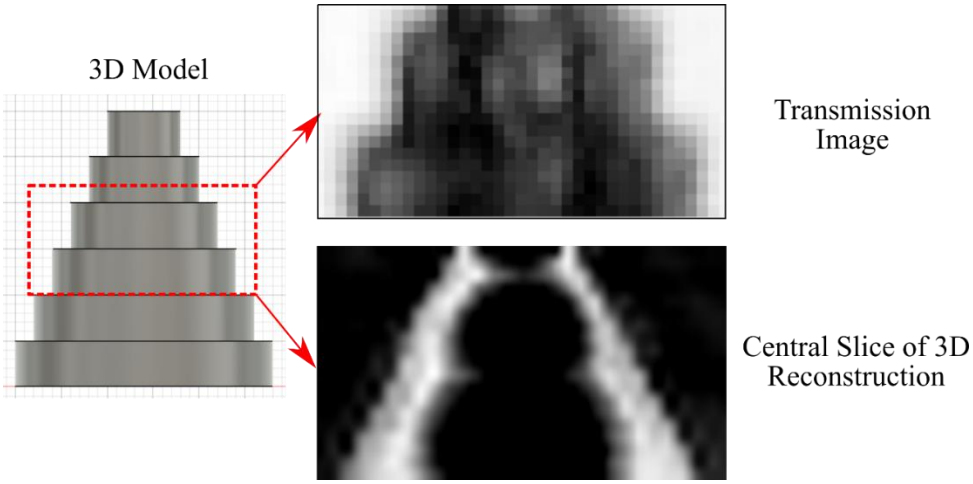

Figure 3.14 Comparison of the 3D model to a transmission image and 3D reconstruction. (Left) 3D model of the tier stack structure with an outline of the scanned section. (Right Top) Transmission image at $\theta = 0°$. (Right Bottom) Central slice of the 3D reconstruction showing false internal voids and gradually changing outer structure.

A full 3D reconstruction is created shown in Figure 3.15. This reconstruction unfortunately does not completely resemble the proper shape of the 3D printed tier stack. Streaking and beam hardening artifacts, resulting in small dense “particles” around the main structure are shown, along with individual scan lines due to the vertical step size. However, the reconstruction is able to create a form that contains a gradually decreasing diameter structure with a hole running through the center: two distinct characteristics of

the 3D printed structure. This reconstruction does set the basis for further 3D reconstruction attempts using this THz system and transmission setup on amber seen later in this research.

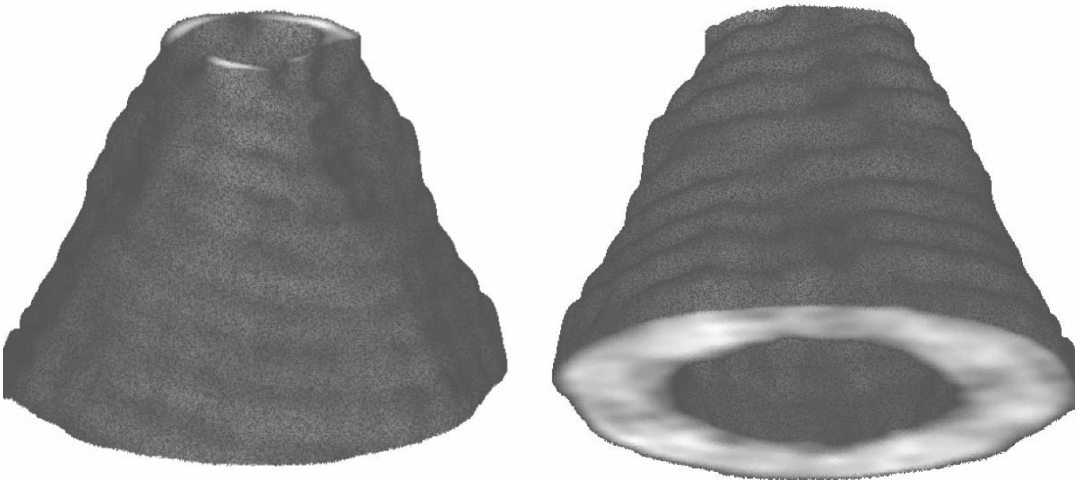

Figure 3.15 3D reconstruction made from 19 individual THz tomographic images of a section of the 3D printed tier stack structure assembled using ImageJ.

3.2.3 Ceramic Relative Permittivity and Defect Detection

To measure the relative permittivity of the extruded ceramics, the samples are mounted to the XY gantry away from the focal point of the lens, to create a larger spot size interacting with the samples in a transmission configuration. This averages the relative permittivity of the samples over an area of roughly 6.25 cm^2. The samples are measured between 60 GHz and 3 THz using the T-ray 5000 system using an average of 2000 acquired THz waveforms. Due to the low signal to noise ratio, valid data is extracted between 110-550 GHz. To verify that this data is accurate, the samples are also measured between 75-110 GHz by Dr. Paul Parsons using a free-space focused beam system constructed at the University of Delaware. The benefit of using two different systems to measure the relative permittivity, is to show that the data is both accurate and repeatable.

As you can see from Figure 3.16, the data from the free-space system matches the T-ray 5000 data very well, confirming that these are accurate measurements. This data confirms that as the sintering temperature is increased, the relative permittivity increases, while not varying over a relatively large frequency range. In the results, “Green State” refers to an un-sintered sample. At temperatures above 1200 °C, the relative permittivity reached a value where the increase between samples decreased dramatically, essentially becoming nil.

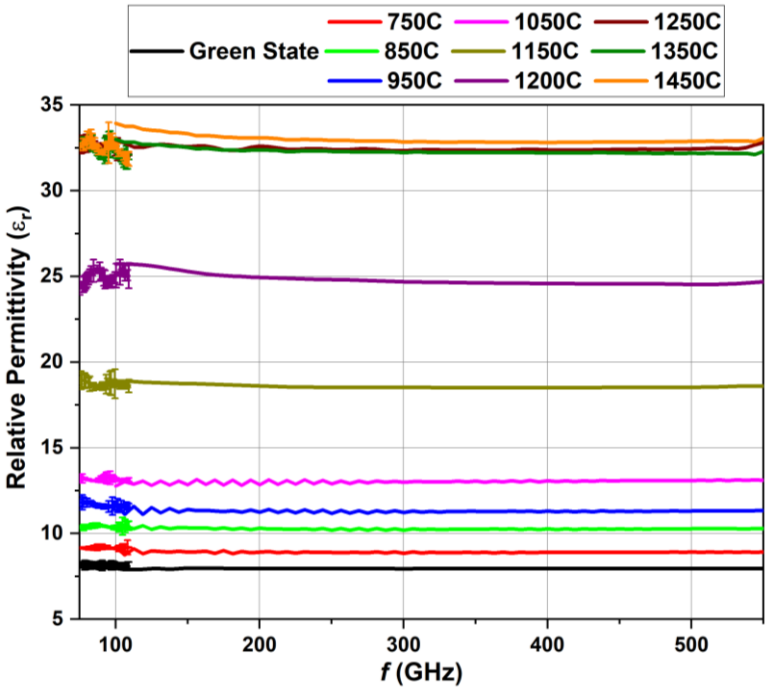

Figure 3.16 Relative permittivity of the various sintered ceramic samples at different sintering temperatures showing data between 75-550 GHz provided by Paul Parsons.
Source: [59].

During these measurements, slight variations in the relative permittivity depending on location were observed when the THz beam was focused over a smaller spot size on the sample. As a result of this observation, images are created by raster scanning the samples

with 0.5 mm^2 pixels, each comprised of an average of four waveforms, in a transmission configuration. The contrast of the images shows the variations in the dielectric constant of the material at that point. Each sample shows clear isotropic volume reduction as the sintering temperature is increased, as to be expected as the particles begin to sinter, and voids begin to disappear with increased temperature. The samples decrease in volume from 1 % up to 18 % at the highest sintering temperature of 1450 °C. Also visible are the numerous horizontal striations seen in all the samples. These striations turned out to be an alignment issue with the XJet printer, verified by XJet staff. The XJet has 24 printheads which are composed of 512 print nozzles per head. Half of the heads spray support material, while the other half spray the ceramic dispersion. By imaging these samples, flaws within all the prints are clearly detectable. That flaw ended up being misaligned print heads, effectively causing an inhomogeneity in the dispersion of the ZrO_2 particles, shown in Figure 3.17.

In the 1450 °C sample, a clear nonlinear horizontal line about two thirds of the way up is visible. This line is a crack that runs throughout the entire length of the sample and suspected to be a product of a combination of material shrinkage and inhomogeneous particle density caused by the misaligned print heads. Notably, this crack is not fully visible under visual inspection, as it can only be seen on one side of the sample and only about one third of the way across that sample. The full extent of the crack was only observed post THz imaging.

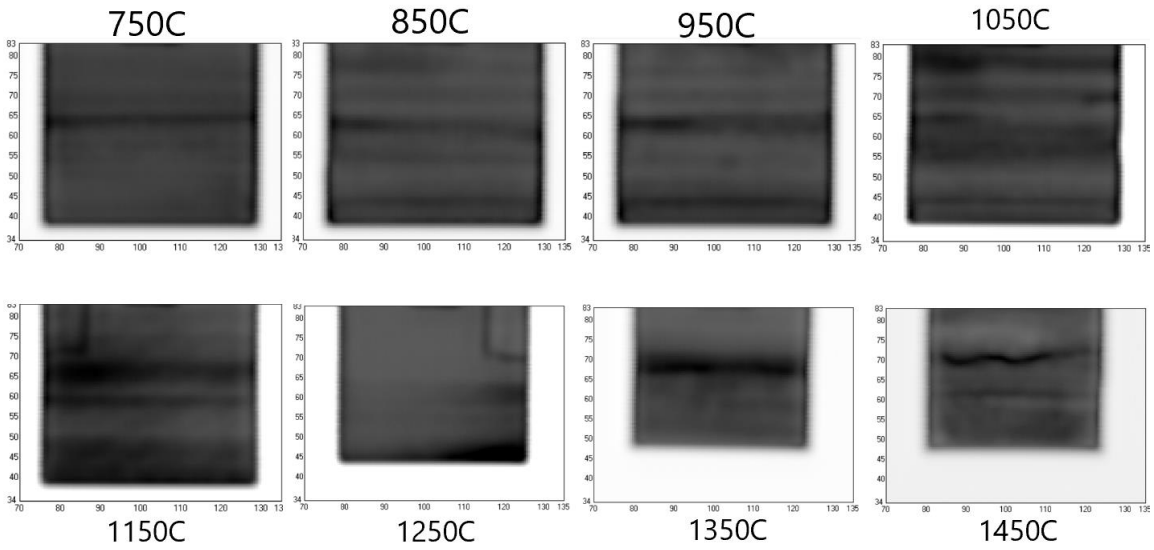

Figure 3.17 Raster scan images of the dielectric constants of varying sintering temperature ZrO_2 samples. Horizontal striations seen throughout are a result of print head misalignment during the printing process.

Of note, on the 1150 °C and 1250 °C samples, the outlines on the upper lefthand and upper righthand corners of the samples, respectively, are a product of leaving the sample identification sticker on during scanning.

3.3 Conclusions

Variations in the printing parameters of 3D printed structures are shown to alter the resulting THz refractive index, attenuation coefficient, and birefringence of the structure. The variations in the printing parameters that alter the THz optical properties can lead to variations in the performance of 3D printed device components as well as potential misinterpretation of THz NDE of 3D printed components. Based on these results, depending on the degree of precision in the real refractive index, attenuation coefficient, and birefringence needed, performance variations in FDM 3D printed structures that rely on tailored optical properties such as microwave and THz based optical components

including lenses, waveguides, and antennas should therefore be taken into consideration by altering certain printing parameters or by establishing a set standard of parameters during the fabrication process. Nozzle size and layer height are not correlated to changes in refractive index and attenuation coefficient, effectively reducing the parameters of concern for these tailored characteristics. The birefringence of the structure is affected by both print orientation and nozzle size. Print orientation has a measurable effect on the refractive index, attenuation coefficient, and birefringence and should always be taken into consideration during the FDM 3D printing process of various optical based application structures.

Upon creating tomographic images and 3D reconstructions of 3D printed structures using THz imaging, several issues presented themselves. There are two major factors that create smearing, boundary effects, and stray artifacts in the resulting tomographic images. First, this style of filtered back projection assumes that all THz beams travel straight through the sample into the receiver in a perfectly parallel beam projection. This is simply not the case, due to the strong refraction and material boundaries that are encountered as the THz beam transmits through the structure being scanned. This reconstruction techniques also assumes that the THz source has an infinitely small focal point, which is also not true. The entire sample is within the depth-of-focus of the beam which helps, but the spot size is on the order of millimeters, resulting in reconstruction that lacks the required detail. Using shorter focal length lenses can partially correct for this issue, as for these reconstructions, 6 in focal length lenses were being used. To also increase the accuracy of the reconstructions, smaller step sizes and decreased angles between projection measurements could be used.

For the tier stacked reconstruction, the scan was most likely not centered on either the rotation stage or horizontal axis, creating an averaging effect on the outer edges, showing how important centering is unless otherwise accounted for. Based on the resulting images and reconstructions, it is concluded that for THz tomography to be useful for THz NDE of 3D printed structures, the combination of corrective algorithms and different reconstruction methods besides standard FBP need to be implemented. ART's, which apply the Kaczmarz's method to Radon's integral equation in which a system of linear equations is solved by converging on solution based on iterative results, have been previously shown reduce beam hardening and improve the resulting THz tomographic images, while simultaneously taking into account refraction and reflection losses [60].

For the ceramic 3D printed samples, by measuring the relative permittivity, it is confirmed that as the sintering temperature is increased, the relative permittivity of the material increased as well, while being non-dispersive over a relatively large frequency range. The largest jump in permittivity is between the 1200°C and 1250°C samples, which leads to the conclusion that within that temperature range, most of the sintering of the ceramic particles occurred. The resulting data also shows that temperatures above 1250°C up to 1450°C, the maximum recommended sintering temperature by XJet, does not substantially increase the relative permittivity and the large jumps between temperatures stops. These measurements showcase THz spectroscopy as a method of electromagnetic response NDE for printed ceramics.

It is also shown that this type of ceramic structure's final size is dependent on maximum sintering temperature due to isotropic volumetric shrinkage which must be accounted for in the structural design. If this shrinkage is not accounted for pre-printing,

post-sintering structural dimensions will not match the ones needed for the application. By imaging the samples as a function of their dielectric constant, observations of linear striation defects are made. These defects are confirmed as print head misalignment, confirming real flaw detection. Also, a full-length crack, not visible under visual inspection, is detected as yet another example of flaw detection using THz as a manufacturing and structural quality NDE method.

CHAPTER 4

GAS PIPE DEFECT IMAGING, CHARACTERIZATION, AND EVALUATION

4.1 Materials and Methods

Polyethylene (PE) gas pipes were supplied by NYSEARCH (www.nysearch.org) for defect detection, imaging, and characterization. The pipes have a 58 mm outer diameter, 4 mm wall thickness, and come in differing lengths. The pipes come in two colors: yellow and black with yellow stripes. The different colors indicated the density of the pipe. Yellow pipes indicate medium density polyethylene (MDPE) while black pipes with yellow stripes indicate high density polyethylene (HDPE). These extruded pipes contain various forms of defects or characteristics including scratches, dents, and butt fused joints.

Normal incidence reflection measurements are taken in attempt to detect and visualize these defects. The scans are taken using the collinear adapter mounted on a custom XY gantry, separate from the T-image, specifically constructed for this application. The pipes are clamped vertically to a LabVIEW controlled rotation stage to allow the collinear adapter to always be perpendicular to the length of the pipe during the scan, maximizing the reflection amplitude. The following reflection peak amplitude and timing images are created using a custom MATLAB code shown in Appendix C.

4.2 Results and Discussion

For the following THz reflection images, figures represented by (A) are the amplitudes measured in volts of the peak reflected from the front surface of the pipe. Images labeled (B) are the amplitudes measured in volts of the peak reflected from the inner surface of the

pipe. Images labeled (C) are the time differences measured in picoseconds between the arrival times of the reflected peaks. Figure 4.1 illustrates the reflected pulses from the two surfaces of the pipe. The change in the sign of the measured amplitude between the front and back peaks are due to the 180 ° phase changed as the pulse reflects off the higher refractive index material of the pipe.

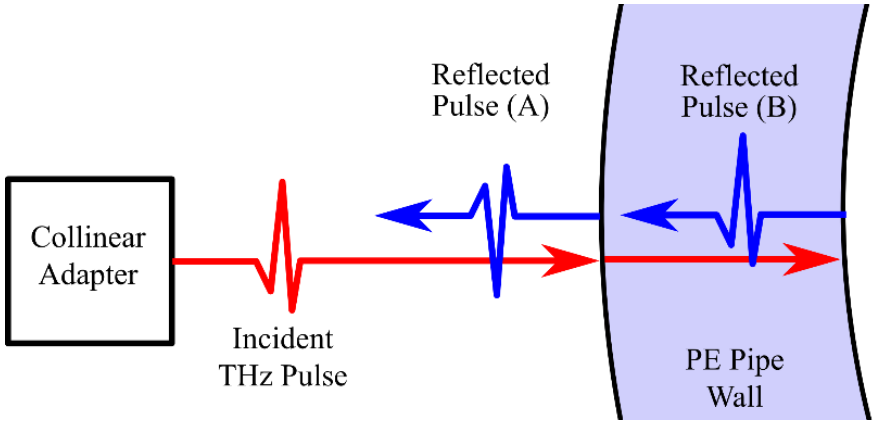

Figure 4.1 Illustration of the incident and reflected pulses (A) and (B) from the front and inner surface of a cross section of polyethylene gas pipe.

It is important to note that since the resulting images are created from the peak amplitudes and timing differences, direct color limit and numerical comparison between the different pipe samples is not applicable. The following images are created solely to assess and confirm THz NDE as a usable method for defect detection and visualization of PE gas pipes.

The first scan, shown in Figure 4.2, comprises of imaging a defect free section of pipe taken as a baseline to compare to the other pipes with known defects. No defects are detected, but there are clear banding artifacts seen throughout all the reflection images. These banding artifacts are seen through all the images taken on the four pipe samples. The

strongest contribution to this effect is from the pipe not being perfectly parallel to the Z scan axis. As the gantry moves up and down, the pipe is then moving closer or further away during the scan affecting both the timing and amplitude of the reflected peaks. This effect is minimized in the other scans due to the larger amplitude difference seen in the defects compared to the smaller variations due to misalignment. Surface texture of the pipe is another factor that may be causing the banding affects, specifically with the amplitude of the reflections. There are sections within the resulting images with high levels of noise due to the lower amount of averaging within each pixel used for this scan.

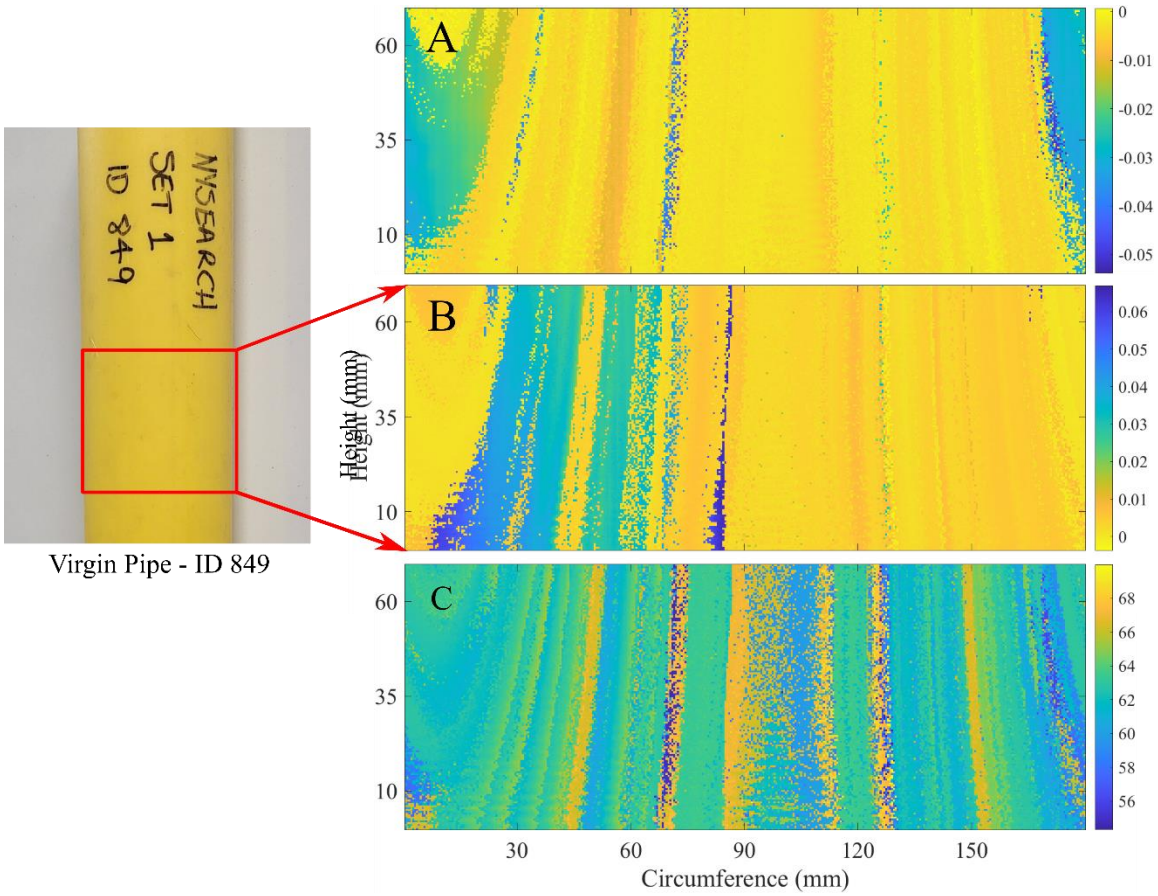

Figure 4.2 70 mm tall and full circumferential scan of a defect free section of MDPE pipe. (A) Front surface reflection peak amplitude (volts). (B) Rear surface reflection peak amplitude (volts). (C) Timing difference between front and back surface reflected peaks (picoseconds).

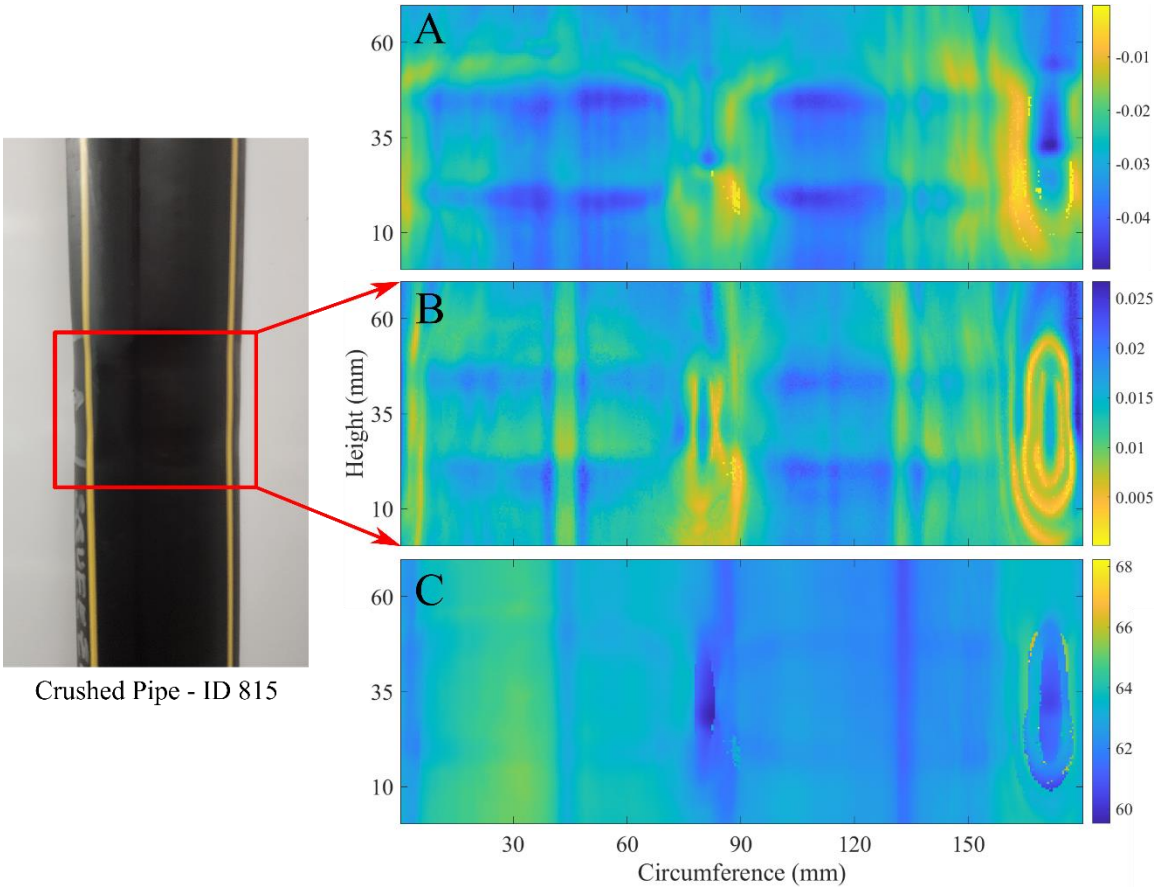

Figure 4.3 70 mm tall and full circumferential scan of a HDPE pipe crushed by over-clamping 70(A) Front surface reflection peak amplitude (volts). (B) Rear surface reflection peak amplitude (volts). (C) Timing difference between front and back surface reflected peaks (picoseconds).

Figure 4.3 shows the resulting reflection images from a section of pipe that was clamped shut. If a section of pipe needs to be replaced, a special type of clamp is used that crushes the pipe to the point where flow is halted. In the photograph on the left, the section of pipe outlined in red is permanently deformed due to the clamping force applied surpassing the pipes yield point where plastic deformation occurred. This type of defect could easily be overlooked during a visual inspection. Since the pipe sustains permanent damage during clamping, it is advised that these pipes are not clamped more than once within a certain distance relative to each other, and if overlooked, could result in total failure of that pipe at the crush location.

In (A), (B), and (C) of Figure 4.3 the area that was crushed becomes clearly visible. Amplitude images (A) and (B) show the horizontal banding equal to the width of the clamp used for deformation. The two distinct points at roughly 80 and 170 mm around the circumference where the most force was applied are clearly visualized. Areas of both increased and decreased amplitude are shown depending on how the pulse was reflected from the indented portions. Image (C) confirms this defect as the result of a crush. The decreased timing differences between the reflected pulses at the points of peak applied pressure visualize areas of decreased thickness due to the material being pressed away from those areas, effectively thinning the wall of the pipe.

Also of note, is that throughout all three images, there are visible vertical lines at roughly 45 mm and 135 mm around the circumference. These vertical lines in the reflection scans correspond to the yellow lines within the picture on the left. The yellow lines are MDPE while the main black pipe polymer is HDPE. Different colors and markings indicate the different specifications and uses for the PE pipes.

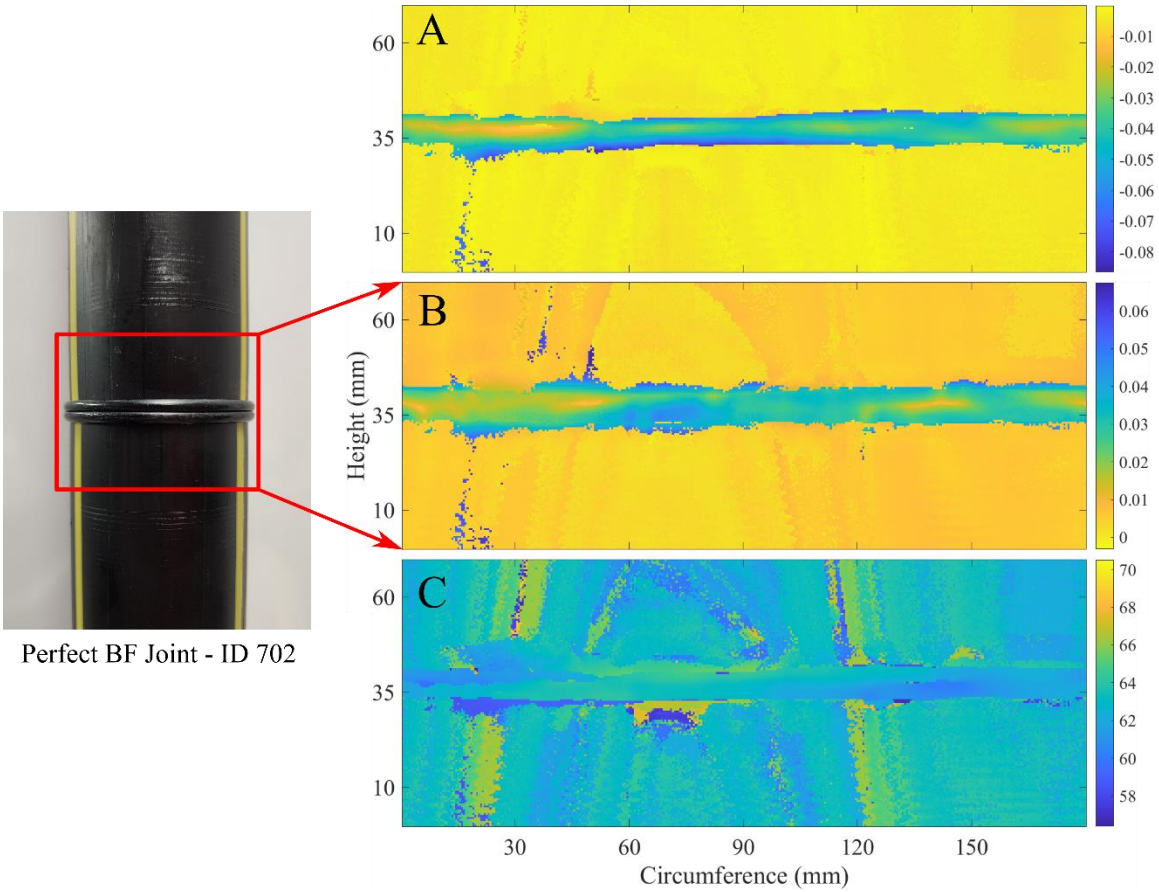

Figure 4.4 70 mm tall and full circumferential scan of a perfect butt fused joint between two HDPE pipes. (A) Front surface reflection peak amplitude (volts). (B) Rear surface reflection peak amplitude (volts). (C) Timing difference between front and back surface reflected peaks (picoseconds).

Figure 4.4 shows scans of a perfect butt fused joint. This scan is where this modality begins to fall apart. Even though this sample is considered to be a perfect joint, defects can occur between the two faces of the pipes that are being joined together. A reflection scan at normal incidence does not have the capability to detect or visualize defects within butt fused joints of the polyethylene pipes, as seen in the resulting images. The main issue with this technique is the diffuse reflection caused by the varying angles on the fusion melt bead. These reflections make it impossible for normal incidence reflection measurements to be used for internal joint based defects. Due to this consequence, another technique must be

used for the NDE of butt fused joints, such as non-normal reflection measurements combined with the use of prisms.

A 300 mm vertical scan is taken on a pipe that contained multiple defects. Four defects are present including blunt force indents, gouges, and two sections caused by over-clamping. The different defects are shown in a front surface reflection amplitude image with their corresponding photographs in Figure 4.5. All the different defects are easily detectable and visualized in the resulting color mapped image of the front surface reflection amplitude.

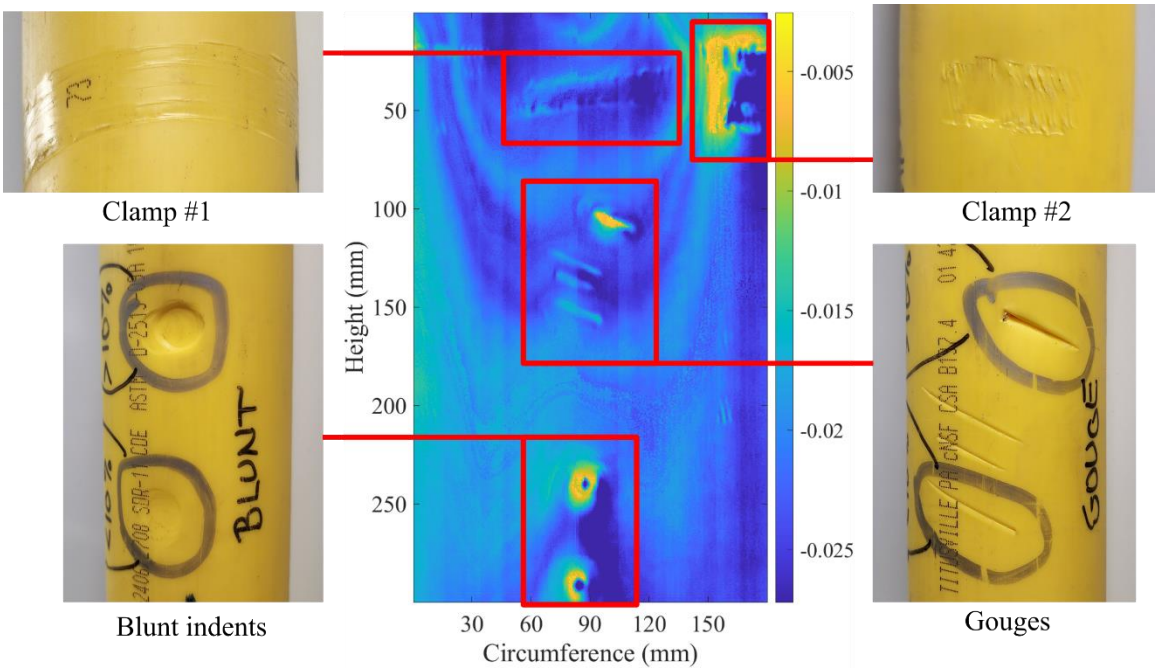

Figure 4.5 300 mm tall and full circumferential normal incidence reflection scan of front surface reflection peak amplitude (volts) on a MDPE pipe containing defects: blunt force indents, gouges, and two sections caused by over-clamping outlined in red with their corresponding photographs.

Figure 4.6 shows the front surface and inner surface reflections together. Three of the four gouges and clamp #1 are essentially not visible in the inner surface reflection. This

is because those defects do not affect the material at the back surface enough to be detectable by an observable change in amplitude. Clamp #2, one of the gouges, and the blunt force indents caused enough damage where they are detectable at the inner surface of the pipe. The material was damaged enough where the profile of the inner surface is affected, and the resulting amplitude varies at those locations.

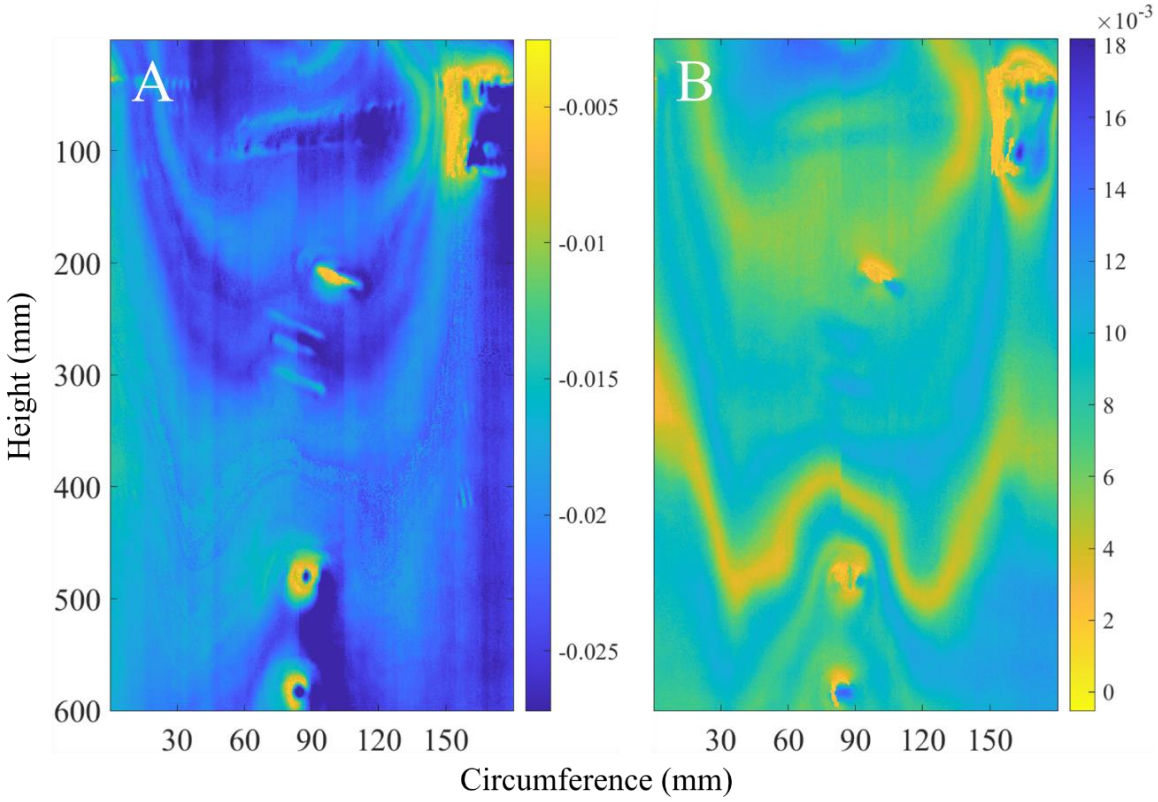

Figure 4.6 300 mm tall and full circumferential normal incidence reflection scan on a MDPE pipe containing defects: blunt force indents, gouges, and two section caused by over-clamping. (A) Front surface reflection peak amplitude (volts). (B) Rear surface reflection peak amplitude (volts).

Using the reflection-based images, a MATLAB code is written to create an interactive 3D visualization model of the surface of the pipe showing the exact location of the defects on the volume, shown in Figure 4.7. This allows for accurate location mapping of the defects detected by the THz NDE. This approach is useful for detecting and creating

an interactive map locating defects present on the inner surface that may not be visible from the outside of the pipe. Using this technique, lengths of pipe could be scanned post-manufacturing and defects could be detected pre-use, eliminating the possibility of manufacturing defects passing quality control.

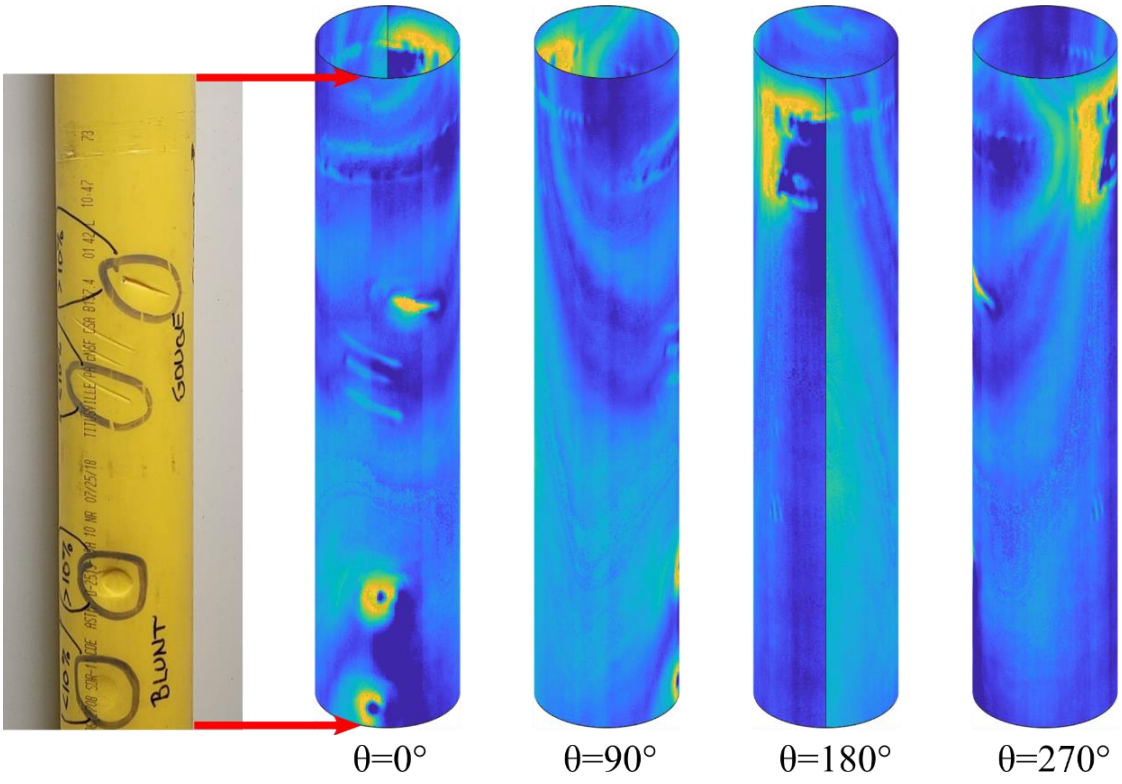

Figure 4.7 3D pipe model viewed at φ=30° at various θ values based on the amplitude measurements of the front surface THz reflection on a MDPE pipe.

4.3 Conclusions

THz NDE is shown to be a promising method for defect detection and visualization on both MDPE and HDPE gas pipes with 4 mm wall thicknesses. Using reflection imaging, multiple defects including cuts, scrapes, dents, and crushed sections are easily visualized using both amplitude and timing measurements. The front surface reflections are able to

detect all external defects on the pipes. The inner surface reflections can detect defects severe enough to cause deformation of the inner pipe wall surface. These normal incident reflection measurements however are not usable for joint based defects. Due to the diffuse reflection from the melt beads, direct reflection data is unusable. Defects within joints are not detectable using this methodology, and other setups must be explored. Also, if thicker wall pipes were to be scanned, this system may not be able to obtain front and inner surface reflections within the same time window due to the timing delay caused by the material. The T-ray 5000 utilizes a 160 ps time window, meaning that to have both reflection peaks within that window, a 4.4 cm thick pipe wall would be the max measurable thickness at a refractive index of n=1.54.

MATALB code is written to create interactive 3D surface maps of the resulting pipe scans, creating a new way to visualize surface level defects. These different visualization techniques allow for accurate detection and location mapping of surface level and thickness variation defects, while also allowing for the detection of inner surface defects without visual inspection.

CHAPTER 5

AMBER IMAGING AND TOMOGRAPHY

5.1 Materials and Methods

An amber sample from the Dominican Republic dated to the Miocene, roughly 16 million years (Ma) old, is used for THz imaging, index matching material testing, THz tomography, and 3D reconstruction. This specimen is specifically used for both its distinct shape and present inclusions of two termite workers from the species Mastotermes electrodominicus. For visual and THz birefringence measurements, three different amber samples are imaged: amber from Santiago in the Dominican Republic deposited in the Miocene (16 Ma), amber from Chiapas, Mexico also deposited during the Miocene (16 Ma), and amber from Bcharre, Lebanon deposited during the Early Cretaceous (119 Ma). All amber samples were provided by Dr. Phillip Barden of New Jersey Institute of Technology (NJIT).

There were various chemicals and materials used in attempt to create an index matching material to match that of the Dominican termite amber. Vaseline brand petroleum jelly as well as CVS, Walgreens, and Fisher Scientific brand mineral oils were purchased as base testing materials. Vaseline and mineral oil were chosen as base materials due to their low attenuation in the THz frequency range, viscosity, and real index of refraction close to that of the amber samples. Different additive powders were selected in attempt to adjust the index matching materials refractive index. The powders, purchased from Sigma Aldrich, include 5 μm zinc oxide powder (ZnO) (semi-conductive), 2 μm barium titanate (IV) powder ($BaTiO_3$) (dielectric), and 21 nm titanium oxide nano-powder (TiO_2) (semi-

conductive). All the powders have higher refractive indices than that of the mineral oil and amber matrix. To effectively disperse these powders throughout the mineral oil, nonionic surfactants, including Span 80 and Triton X-100, were purchased from Sigma Aldrich. To further assist in the dispersion process, cyclohexane was also purchased. These powders, surfactants, and chemicals were selected based on previous work performed in altering liquids refractive indices in the THz range, characterization measurements, and creating microemulsion and suspensions from the following references [41], [61]–[64].

Clear plastic display boxes in two sizes were purchased from TAP Plastics to be used as index matching material vessels. These boxes allowed for the THz beam to enter and exit the material and sample at normal incidence, minimizing refraction. These boxes, filled with the resulting index matching materials, are attached to the T-image XY gantry using a 3D printed mount along with a LABVIEW controlled rotation stage to image the amber samples as shown in Figure 5.4. Tomographic images and 3D reconstructions are created using the methodology, MATALB code shown in Appendix B, and ImageJ software that were discussed in Section 2.4.3.

For the visual birefringence images, sheets of linear polarizing film, glass photography polarizers, and a light box were purchased to create a visual adjustable polarization imaging setup, shown in Figure 5.1. The linear polarizing film was cut to fit into the light box to create a linearly polarized light source and backdrop. For the birefringence images, the amber is placed onto the linearly polarized film while a polarizer is attached to the digital camera, allowing for easily adjustable polarization angles.

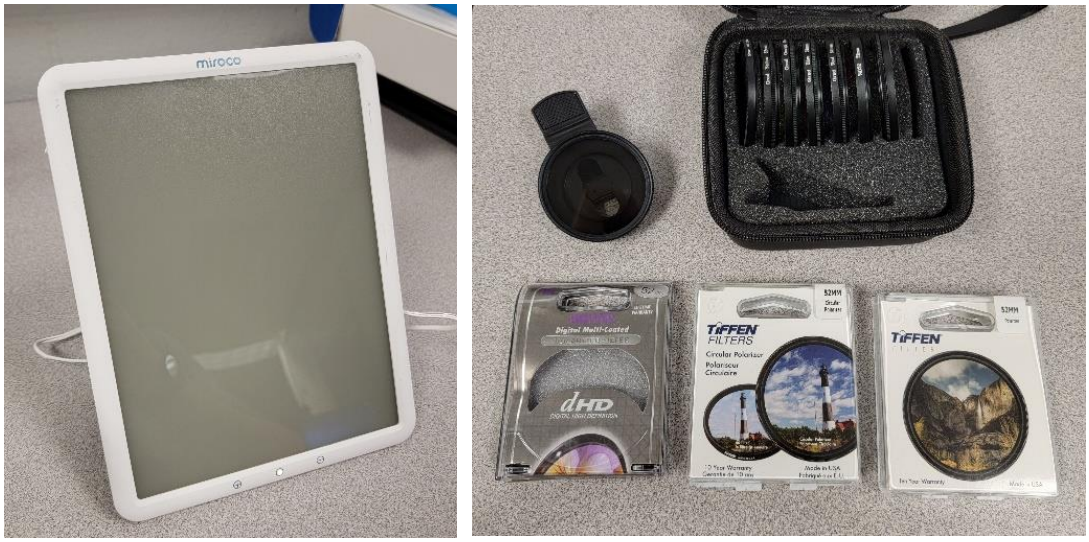

Figure 5.1 Linearly polarized light box and glass photography polarizers used for amber visual birefringence measurements.

5.2 Results and Discussion

5.2.1 Refractive Index Matching Material, Imaging, and Tomography

To create an index matching material, the real refractive index of the sample must be measured. The Dominican amber matrix was measured to have a refractive index of n=1.581±0.003. The first attempts at using an index matching material for THz imaging was using Vaseline. Vaseline is a combination of petroleum jelly, microcrystalline wax, and minerals with a measured refractive index of n=1.511±0.003. The Vaseline is heated to its melting point, poured into the plastic vessel, and the amber sample was inserted into the liquid before it solidified. This process allows for the removal of air bubbles in the material and allows for the liquid Vaseline to fully surround the sample. Once solidified, the amber is imaged multiple times while being rotated at discrete angles for computed tomography and 3D reconstruction.

The results of the imaging process using Vaseline are shown below, along with an image of the specimen for comparison. The blur of the images is a product of the frequency

integration range chosen for each pixel value. As the frequency increases, the effective spot size of the beam decreases allowing for a sharper image. Also, the peak power of the THz system is located around 225 GHz, meaning that a frequency integration around that frequency is dominated by the lower frequencies. Figure 5.3 shows the difference in image quality using both a frequency integration over 0.1-2 THz and 0.5-2 THz represented by the figures contrast. A frequency integration range of 0.5-2 THz is chosen for the amber imaging due to its increase in image sharpness without power sacrifice.

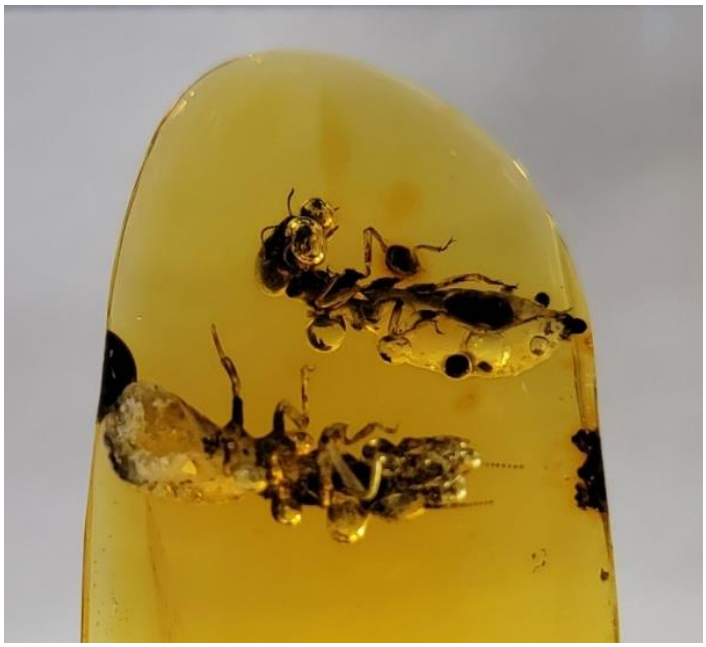

Figure 5.2 Closeup reference picture of the two termite workers in the Dominican amber framed similarly to the frequency integration images created using the THz system.

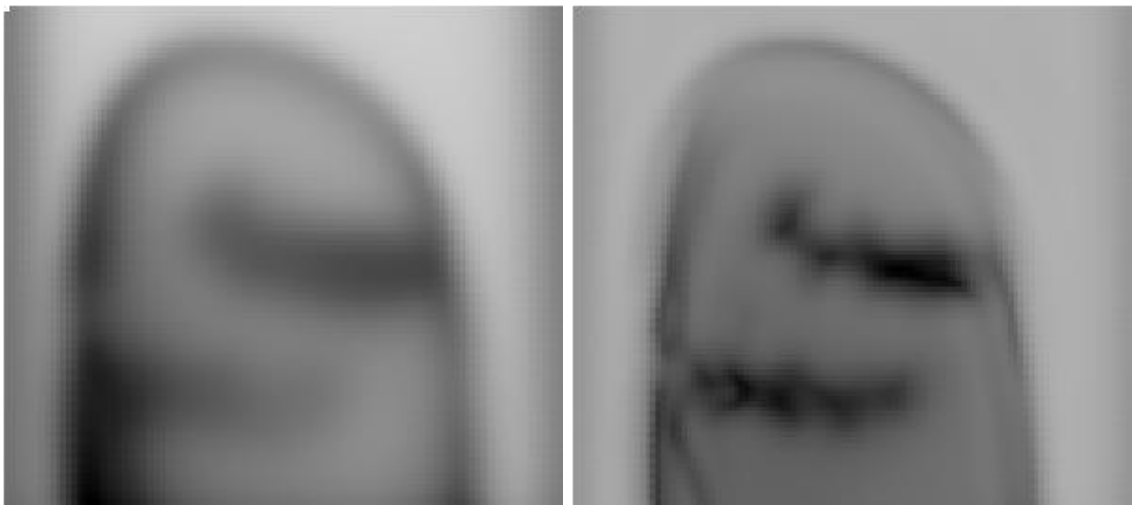

Figure 5.3 Frequency integration comparison of the Dominican amber specimen. (Left) 0.1-2 THz amplitude integration. (Right) 0.5-2 THz amplitude integration. Excluding the lower frequencies that dominate the peak power of the system allows for increased resolution.

The resulting images show the termite inclusions and the outer structure of the amber sample. The contrast of the Vaseline background and the amber matrix is similar but different because the real refractive indices are not a perfect match to each other ($\Delta n=0.07$). This mismatch in real refractive index is also responsible for the "ghosting" effect around the edges of the sample. Refraction at the edges is strong enough to cause artifacts in the resulting images, similar to that seen in the tomography of the 3D printed structures. Even though the image distortion, due to refraction at the edges of the sample, is stronger within the higher frequency range, the 0.5-2 THz frequency range integration is used for imaging of the Dominican amber sample to increase the resolution of inclusions in the resulting images.

The sample is then rotated a set number of degrees in attempt to create tomographic images and a 3D reconstruction using the Vaseline as the closely index matched material. Once the imaging is complete, it was observed that the consistency of the Vaseline is not ideal for this imaging modality. As the amber rotated, the Vaseline would stick in some

spots and create air gaps in others. As seen in Figure 5.4, the Vaseline began to ball up around the unsubmerged portion of the amber. As the amber was removed from the Vaseline, it was also clear that due to the samples spoon-like shape, a specific portion of the Vaseline was being rotated with the sample ultimately creating air bubbles and gaps in its path, shown in Figure 5.5. These air gaps completely ruin the effectiveness of an index matched material as the material is no longer homogeneous. Figure 5.6 is a before and after frequency integration image of a full 360-degree rotation in the Vaseline. Comparing the two pictures, they should look identical if no air gaps were created, but clearly that is not the case. In attempt to fix this issue, the amber was fully submerged in a larger container of freshly heated and solidified Vaseline. This led to similar and unusable results.

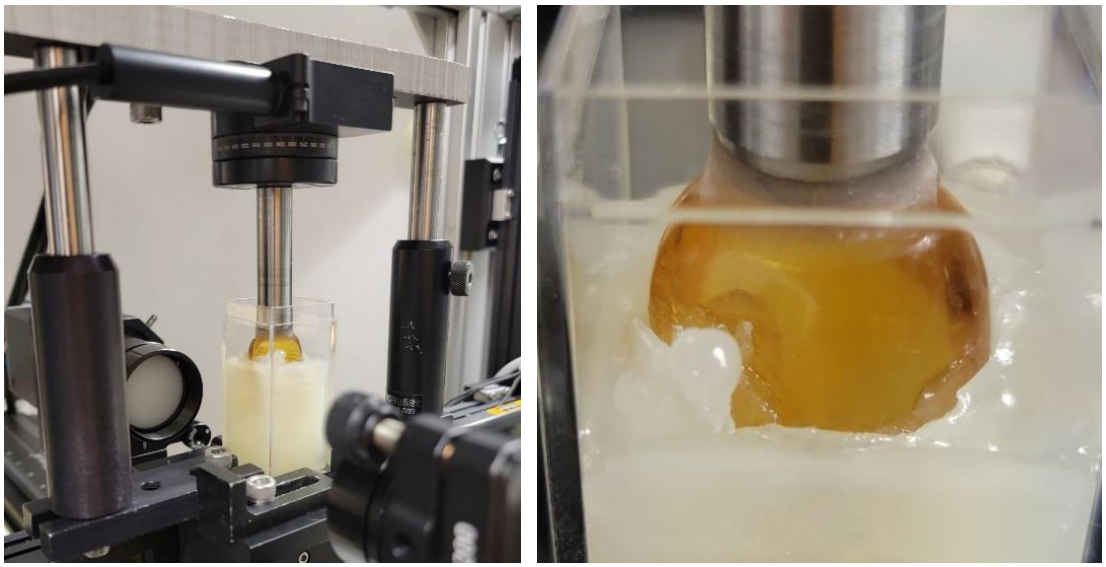

Figure 5.4 (Left) Amber sample mounted to rotation stage half submerged in Vaseline as a refractive index matching material used for THz imaging. (Right) Showing the poor viscosity of the Vaseline after rotation.

Figure 5.5 Before (Left) and after (Right) images of the Dominican amber sample showing how a large portion of Vaseline adhered to the sample's left surface due to its spoon-like shape causing air gaps in the Vaseline during rotation.

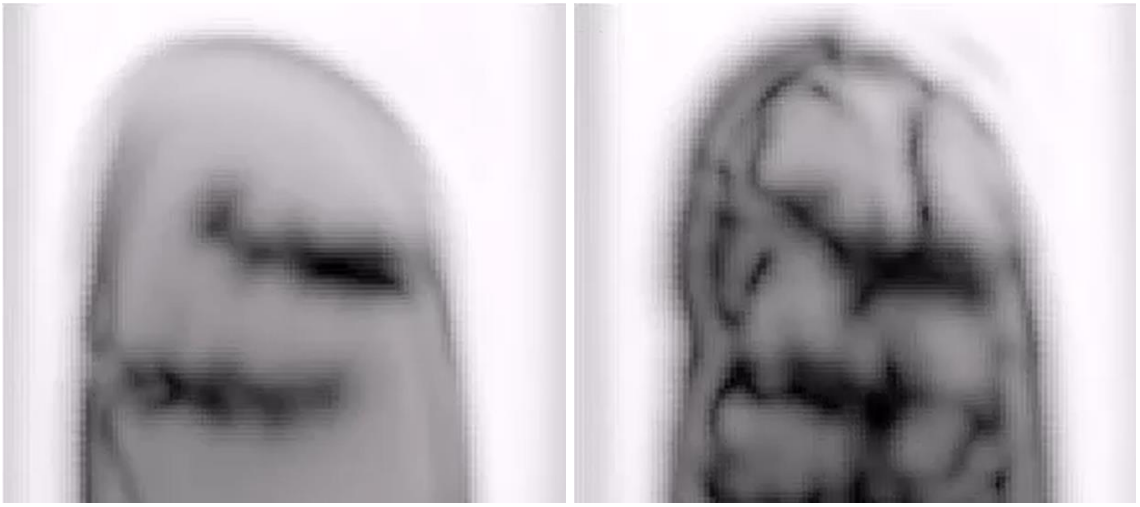

Figure 5.6 THz images taken before (Left) and after (Right) a full 360-degree rotation in an attempt to use Vaseline as an index matched material for THz imaging and CT. Air gaps became present within the material as the sample rotated effectively ruining the index matching effect creating many artifacts in the resulting transmission image.

Since the viscosity of the Vaseline caused it to be unusable for THz CT of the amber, another base material for a refractive index matched liquid is chosen. Two different brands of mineral oil, CVS and Walgreens, were purchased and their real refractive indices are measured as n = 1.466 and n = 1.468, respectively. The Walgreens brand mineral oil having a slightly higher refractive index is chosen as it exhibited a closer refractive index to that of the amber, with a difference of $\Delta n=0.113\pm0.006$. Preliminary scans are taken using the Walgreens brand mineral oil until upon further inspection, it contained Vitamin E added as a stabilizer. This added ingredient was increasing the attenuation of the liquid: the exact opposite of what is needed for an index matching liquid. Fisher Scientific brand pure mineral oil was purchased and characterized as n=1.462.

Before imaging the Dominican amber in the mineral oil, a spare amber sample was placed in the mineral oil for 24 hours. No change in mass was observed, the amber had no visual surface defects, and the mineral oil was easily removed using isopropyl alcohol. Knowing that the mineral oil will not affect the amber, the Dominican amber was imaged once again.

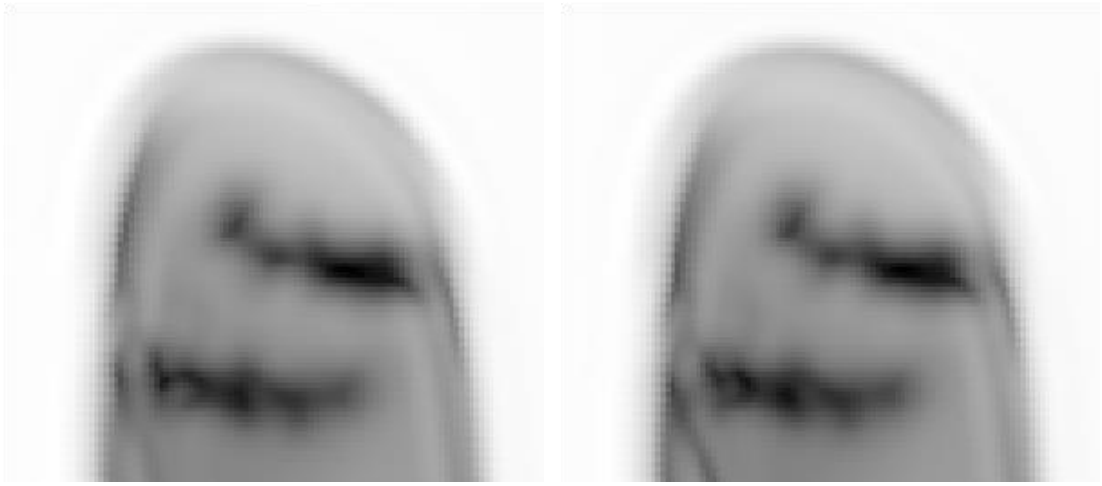

Figure 5.7 Comparison of 0.5-2 THz frequency range integration images of the amber sample before (Left) and after (Right) a 360-degree spin in Fisher Scientific pure mineral oil. No differences are observed.

As seen in Figure 5.7, the mineral oil worked very well as an index matched material, and even after a full rotation, because of its viscosity, did not create any air gaps or bubbles around the amber sample. There were little to no visual differences in the images pre (Left) and post (Right) rotation.

Using the full 360 degree set of transmission images, a set of sinograms and tomographic images are created using the MATLAB code. The tomographic images are turned into a 3D reconstruction of the amber, shown in Figure 5.8, using the Volume Viewer plugin in ImageJ. Below is a comparison of the 3D reconstruction and an image of the amber from the same angle. The 3D image shows an accurate structural reconstruction with fairly accurate edge detection. In the lower middle portion of the reconstruction, the different shade of orange is due to that portion of the reconstruction being cut off due to limited scan size, as well as the left and right lower edge. When the resulting sinograms of a scan are put into the inverse Radon transformation, the resulting image becomes truncated at the edges depending on the discrete angles between projection measurements. The horizontal scan length during imaging should have been larger for a full reconstruction in both the X and Y directions, resulting in a complete reconstruction of the structure. There is a clear improvement in the shape of the reconstruction compared to that of the 3D printed tier stacked structure, thanks to the use of the index matching material, increased scan resolution, and more accurate centering of the sample within the horizontal scan axis.

Figure 5.8 3D reconstruction (Left) and picture (Right) of the Dominican amber sample. 3D reconstruction shows good outer edge detection. The lower middle portion (lighter orange) of the reconstruction is incomplete due to small scan size.

In attempt to image the inclusions separately, adjustments to the luminance of the transfer function within the 3D reconstruction, more of the internal structure was able to be imaged. Shown in Figure 5.9, the reconstruction with the adjusted luminance values, allows for visualization of different parts of the internal structure. The lower termite has been completely loss due to the high amount of refraction on that part of the amber due to a combination of a mismatch in the refractive index as well as the rounded shape of the amber creating a non-normal reflection at that location, seen in the side profile. This does show a partial reconstruction of the upper termite, specifically the head, that may be caused due to the increased density within. There is a lighter region of decreased refraction in the upper portion of the sample surrounding the upper termite due to parallel faces of the sample within that region allowing for close-to-normal incidences reflection measurements.

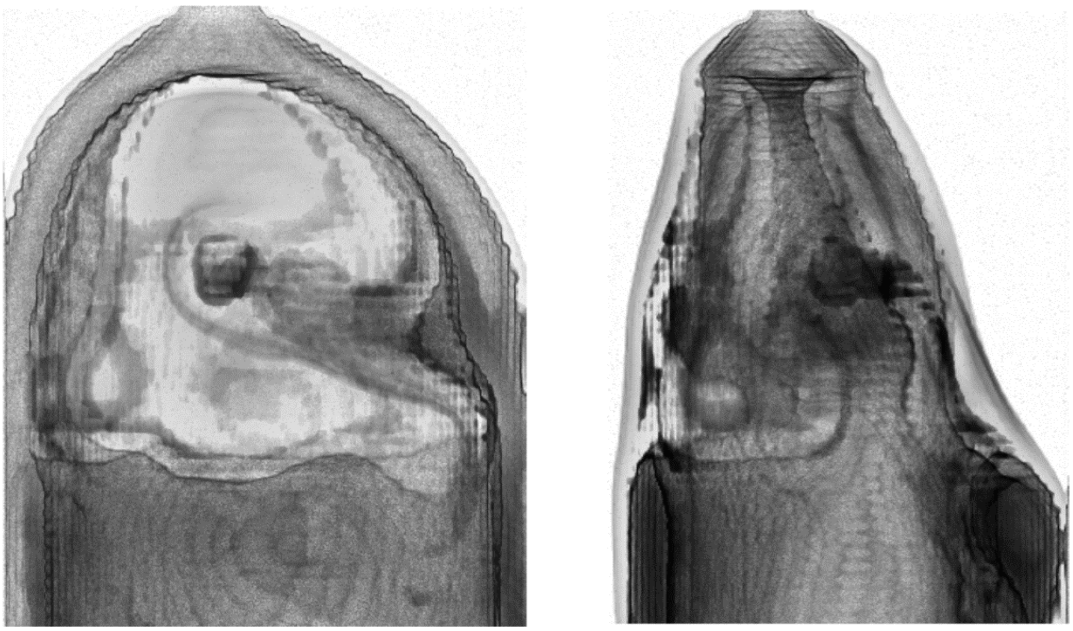

Figure 5.9 3D reconstruction of the Dominican amber sample with adjusted transfer function luminance allowing for internal structure observation. (Left) Front profile. (Right) Side profile.

Since there was still a substantial difference in the refractive indices of the amber and mineral oil, a closer index matching material needed to be used to decrease the refraction effects. In attempt to create a closer index matched liquid to that of the amber, two batches of index matching fluid were created. The first was a 4 % w/w TiO_2 concentration comprised of 1 g of TiO_2, 1 g of Triton X-100, and 23 g of mineral oil. The second was a 4 % w/w $BaTiO_3$ concentration comprised of 1 g of $BaTiO_3$, 1 g of Triton X-100, and 23 g of mineral oil. The Triton was bar stirred in the mineral oil for five minutes before the powders were bar stirred in for an additional ten minutes. Since these powders were on the µm scale, probe sonication was suggested and implemented. The suspensions were characterized before and after the pulsed probe sonication with the refractive index and attenuation results shown in Table 5.1.

Table 5.1 Real Refractive Indices and Attenuation Comparison of Pure Mineral Oil and Mineral Oil Powder Suspensions Before and After Probe Sonication

Composition	Real Refractive Index (n)	Attenuation (cm^{-1}) at 225 GHz	Attenuation (cm^{-1}) at 500 GHz
Pure Fisher Mineral oil	1.462	1.357 (noise)	2.129 (noise)
4% TiO_2	1.504	14.59	54.72
4% TiO_2 (Sonicated)	1.480	23.74	47.42
4% $BaTiO_3$	1.487	18.20	63.24
4% $BaTiO_3$ (Sonicated)	1.479	29.51	54.38

Note: There were large Fabry-Pérot oscillations in the attenuation measurements. The (noise) label indicates that these oscillations caused major changes in the attenuation observed within a short frequency range around the given frequency.

The real refractive indices were frequency independent for each measurement. As seen in the table, there was a clear refractive index increase in both mixtures compared to pure mineral oil. Sonication caused a decrease in the refractive index while also almost doubling the attenuation of the liquid at the lower frequencies where the peak power of the THz system is located. The sonication method used greatly increased the temperature of the mineral oil, decreasing its viscosity. This caused the powder to move to the outside edges of the container and begin to clump and create a layer of powder as opposed to evenly disperse it throughout the mineral oil, even with the use of the surfactant. This condensed powder is the cause for the decrease in refractive index and increase in absorption because the powder is no longer homogeneously dispersed throughout the mineral oil.

There was suspicion that the major increase in attenuation was due to the choice and amount of surfactant used to disperse the powder particles. The surfactants needed to be characterized to make sure that they were not the dominating factor. Triton X-100's attenuation was too high to measure by itself so a 10 % mixture with mineral oil was prepared and measured. Span 80 was also characterized and compared to pure mineral oil in Table 5.2.

Table 5.2 Real Refractive Indices and Attenuation Comparison of Pure Mineral Oil, Triton X-100, and Span 80

Composition	Real Refractive Index (n)	Attenuation (cm^{-1}) at 225 GHz	Attenuation (cm^{-1}) at 500 GHz
Pure Fisher Mineral oil	1.462	1.357 (noise)	2.129 (noise)
10 % Triton X-100	1.469	13.71	29.45
Span 80	1.534	100.9	289.9

Note: There were large Fabry-Pérot oscillations in the attenuation measurements. The (noise) label indicates that these oscillations caused major changes in the attenuation observed within a short frequency range around the given frequency.

The Triton X-100 had very little effect on the refractive index but did increase the attenuation by an order of magnitude. Span 80, since it was not in a mixture of mineral oil, showed a very high attenuation and slight increase in refractive index compared to pure mineral oil. Triton X-100 was concluded to be the better option as it did not alter the refractive index as much, allowing for the powder ratio to be dominant in the refractive index alteration. It was also concluded that as little surfactant as possible would be used to keep attenuation at a minimum in the resulting mixture. $BaTiO_3$ was abandoned as a powder additive as 20 minutes after mixing was completed, separation of the powder from the mineral oil began. After 18 hours post-stirring, the $BaTiO_3$ was almost completely separated from the mineral oil. This is because $BaTiO_3$ is a polar ferroelectric material and mineral oil is nonpolar, causing quick separation.

In attempt to disperse the surfactant over the powder more uniformly, cyclohexane was added to the solutions during the stirring process. ZnO powder solutions were also mixed and characterized. Based on the previous results, half the volume percentage of surfactant was used. 2.5 % ZnO and 2.5 % TiO_2 mixtures were made. The powder, Triton X-100, and cyclohexane were first bar stirrer for ten minutes before the mineral oil was added. They were then bar stirred for three hours on low heat allowing the cyclohexane to

evaporate. After characterization was performed, TiO_2 was determined to be the optimal powder due to the increase in refractive index and moderate increase in attenuation. Another 3.3 % TiO_2 mixture was made and characterized in attempt to closely match the refractive index of the amber, all shown in Table 5.3.

Table 5.3 Real Refractive Indices and Attenuation Comparison of Mineral Oil, ZnO, and TiO_2 Powder Suspensions

Composition	Real Refractive Index (n)	Attenuation (cm^{-1}) at 225 GHz	Attenuation (cm^{-1}) at 500 GHz
2.5 % ZnO	1.495	14.17	27.18
2.5 % TiO_2	1.549	11.59	29.28
3.3 % TiO_2	1.592	15.52	39.47

Note: Mixtures made using cyclohexane to assist in surfactant dispersion onto the powder particles.

The 3.3 % TiO_2 mixture had the closest refractive index to the amber yet at n=1.592. Using this index matched mixture, transmission images were taken and the resulting power integration images from 0.5-2 THz are shown below in Figure 5.10. By adjusting the integration result boundaries, the termite structures were able to be separated from the amber matrix resulting in a fairly well-defined outline of the inclusions.

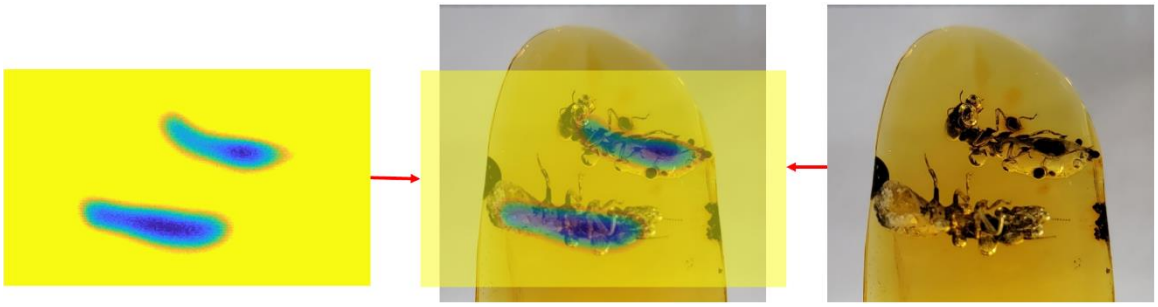

Figure 5.10 (Left) Transmission power integration image over 0.5-2 THz of the termite inclusions submerged in a 3.3 % TiO_2 mineral oil real refractive index matched fluid. (Middle) Overlap showing termite outlines. (Right) Amber image.

Post imaging the powder began to separate from the mineral oil once again. These mixtures, even though adjustable refractive index was obtained, still had substantial absorption, and quickly began to separate post stirring. A mixture that changes composition over short periods of time is unsuitable for the long measurements needed for tomography and 3D reconstruction. Attempts at making a perfectly matched refractive index fluid using powders were abandoned and the possible solution of purchasing premade adjustable refractive index fluids was proposed.

5.2.2 Visual and THz Birefringence Images

Since we know that amber is a photoelastic material, visual birefringence images can assist in determining the locations of various inclusions or detect areas of varying stress induced within the amber during its creation and polymerization process. Two samples, Dominican and Mexican Chiapas amber, were imaged using the polarized light setup mentioned previously. Three different images were taken for each, all shown in Figure 5.11. First, denoted by (A), the linearly polarized light source was placed behind the amber. Images denoted by (B) were taken using the linearly polarized light source as well as a linearly polarized camera lens in parallel. Images denoted by (C) were taken using crossed linear polarizers. Visualization of the birefringence in the structure using crossed polarizers is clear as the only light that reaches the camera has changed polarization due to the birefringence within the material, hence the strongest variations in color. The variations in color represent the varying levels of stresses within the amber.

Using this techniques, areas of highly localized stress are observed. In the Dominican amber, the inorganic inclusions are outlined in color variations due to the localized stresses induced during the amber's extrusion and polymerization process. The

Mexican Chiapas amber has similar areas of localized birefringence but at a much stronger level, denoted by the stronger color and contrast variation. The Chiapas amber seems to have multiple levels of birefringence throughout the structure. When the sample is rotated, the color variations rapidly change depending on the angle of observation.

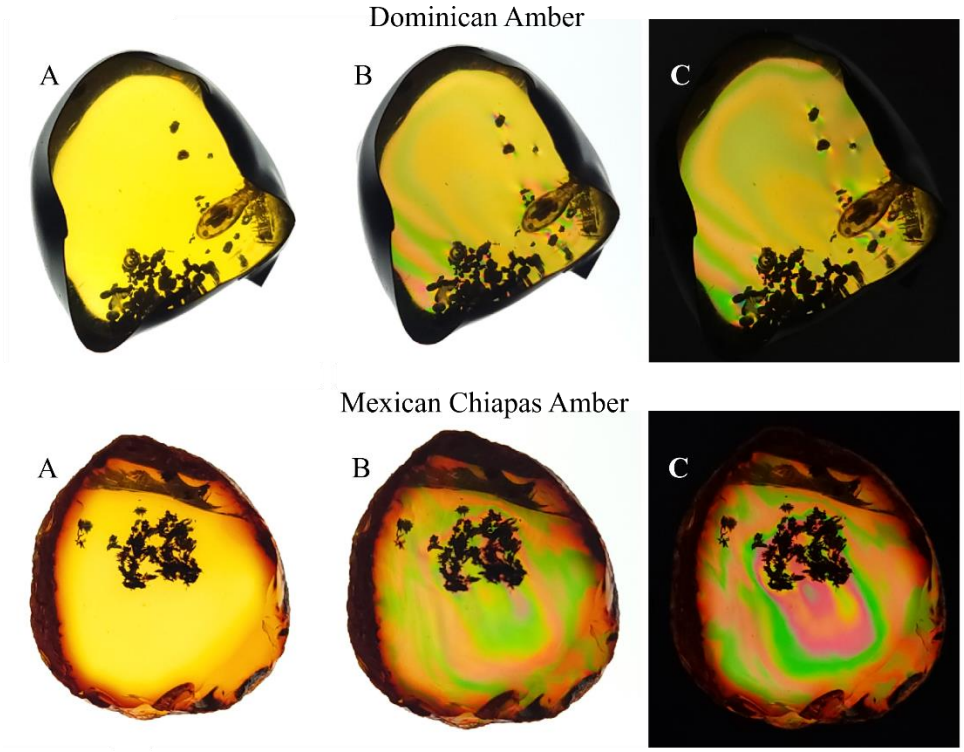

Figure 5.11 Visual Polarization Images of Dominican (Top) and Mexican Chiapas (Bottom) amber. (A) Using a vertically linear polarized light source behind the amber. (B) Using a linear polarized lens parallel to the polarized light source (C) Using a linear polarized lens perpendicular (crossed) to the polarized light source.

One amber specimen showed something that the other samples did not. If a sample had a uniaxial stress throughout, and under the assumption that the stress is in the plane perpendicular to the propagation of the polarized visible light, no polarization change would be observed when that stress direction is oriented either parallel or perpendicular to the direction of that linear polarization. Upon observation, the light through the sample is

blocked at two specific rotation angles by the second crossed linear polarizer due to the lack of polarization rotation. In theory, the two rotation angles at which the minimum light transmission is present are orthogonal if these conditions are met.

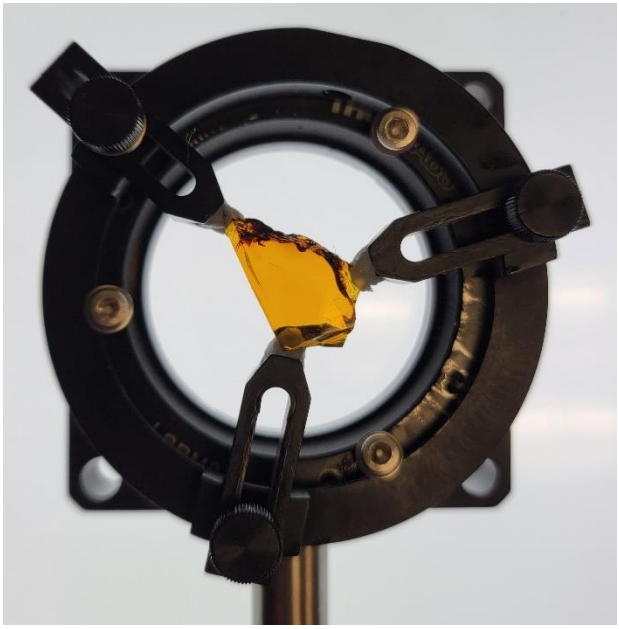

Figure 5.12 Lebanese amber sample held within a rotation stage used for visual and THz birefringence imaging and measurements.

The Lebanese sample met these conditions and was placed in a rotation mount shown in Figure 5.12. In Figure 5.13, (A) shows a visible photoelastic image of the amber sample at an angle that is not parallel or perpendicular to the direction of the stress, showing the resulting birefringence. Images (B) and (C) show the resulting angles corresponding to minimum polarization rotation. Using the sample's flattest side as a reference, the angular orientation of the sample relative to the vertical polarization was measured using ImageJ. The first rotation angle for minimum birefringence was found to be approximately 24.9 ° from vertical, while the second angle for minimum birefringence was approximately 114.4 ° from vertical: making the difference 89.5 ° between the two angles. The

measurements strongly align with the expectation that the two rotation angles corresponding to minimum polarization rotation should be 90° apart, illustrating that the two principal directions of stress in this sample are orthogonal.

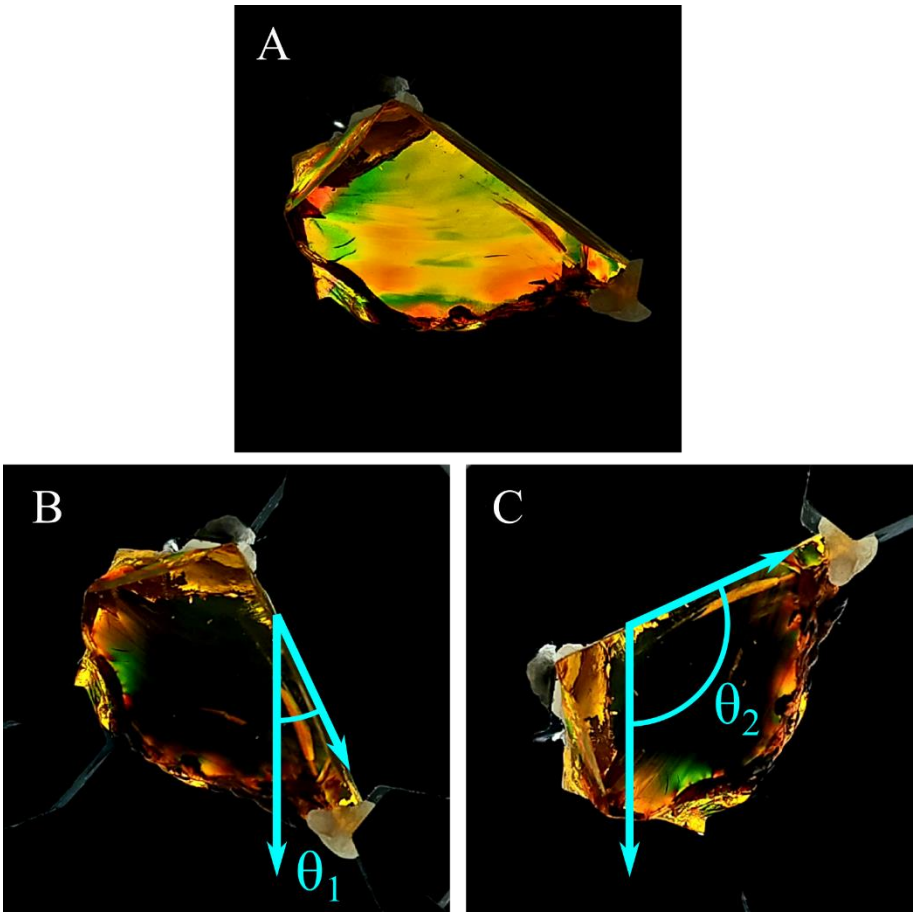

Figure 5.13 Visual birefringence images of the Lebanese amber specimen. (A) Crossed polarization image showing birefringence at an arbitrary angle. (B) Image showing minimum transmission at θ=24.9 ° from vertical. (C) Image showing minimum transmission at θ=114.4 ° from vertical.

To compare to the visual measurements, as well as confirm the methodology described in Subsection 2.4.2.1 on determining the birefringence magnitude and stress direction within a material, birefringence measurements were taken using the THz system. Using a MATLAB code written by Dr. John Federici of NJIT, shown in Appendix D, the

change in real refractive index between polarizations (Δn), thickness variations within the sample, and the resulting direction of stress (φ) could be extracted from the reflection data by measuring the reflected pulses at three polarization angles: θ=0, θ=$\pi/2$, and θ=$\pi/4$. A small block of extruded PE with uniform thickness, previously measured to have a birefringence due to its manufacturing process, was imaged at two different rotational orientations.

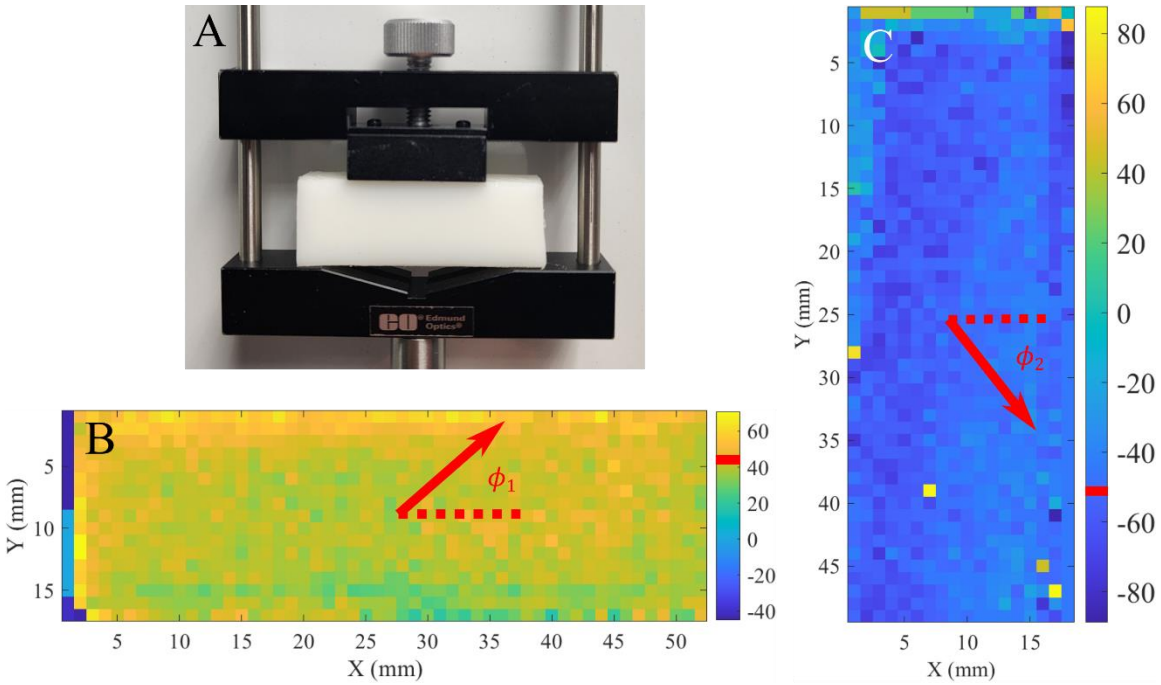

Figure 5.14 Stress direction determination on an extruded PE block. (A) Image of the block held in a mount. (B) Horizontal scan showing average resulting stress direction as ϕ=41.1 ° from horizontal. (C) PE block rotated 90 ° CW, vertical scan showing average resulting stress direction as ϕ=-51.7 ° from horizontal.

Shown in Figure 5.14, the direction of stress within the material was successfully calculated. The PE block was first imaged horizontally, and the average stress direction, or birefringence, was calculated to be ϕ=41.1 ° from horizontal. The block was then rotated 90 ° clockwise and imaged again. The resulting average stress direction in the vertical scan

was calculated to be ϕ=-51.7 ° from horizontal. This means that the experimentally measured direction of stress was observed to rotate by just about 90 ° when the sample was physically rotated by 90 ° in the experimental setup: a successful demonstration of stress direction determination. The four yellow pixels in Figure 5.13C are likely caused by the method used to extract the angles and are effectively rotated 180 ° from their true value since alternating stress directions can be interchanged. Adding 180 ° to these pixels would correct their value. It is also important to note that the thickness variations and Δn calculations between rotations had very small differences, as expected.

Using this data as a confirmation of methodology, the Lebanese sample was then imaged. To compare to the visual measurement's minimum transmission angles, the sample was scanned at two angles 90 ° relative to each other. Theoretically, the resulting direction of stress should change by 90 ° like seen in the visual measurements and the measurements taken on the PE block. The results for the Lebanese amber sample are shown below. Figure 5.15 shows the Δn measurements between the θ=0 and $\theta=\pi/2$ polarization angles across the sample pre and post a 90 ° rotation. Little to no differences are shown as expected. Figure 5.16 shows the thickness variation across the sample. This shows that the measurement was not consistent when the sample was rotated, clearly indicated by the greatly varying thickness values in the right side of the post rotation scan. Figure 5.17 shows the angle of stress (ϕ) pre and post rotation. The stress angle results were not consistent, meaning they did not rotate as expected with the sample when it was rotated 90 ° clockwise.

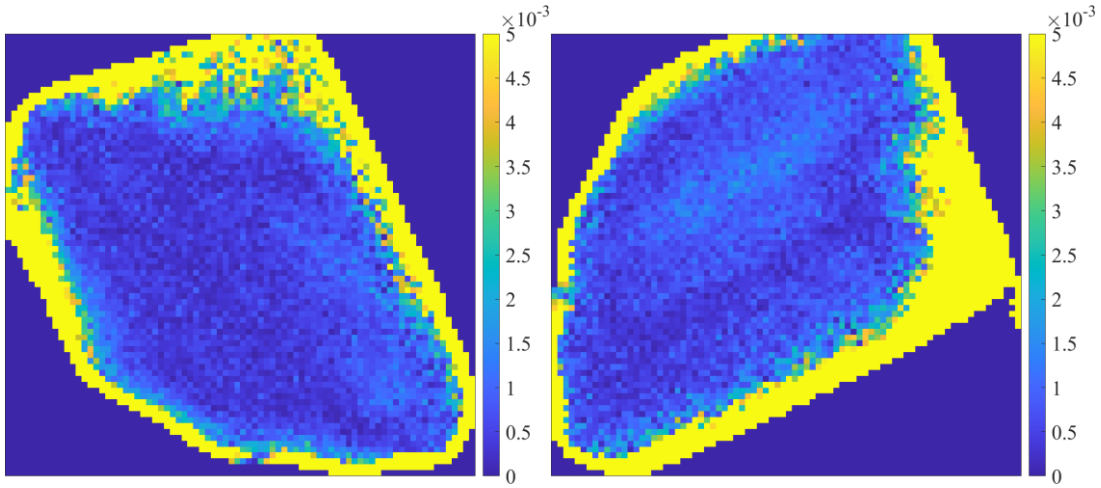

Figure 5.15 Birefringence (Δn) between the θ=0 and θ=$\pi/2$ polarization angles pre (Left) and post (Right) a 90 ° rotation. Little to no difference shown.

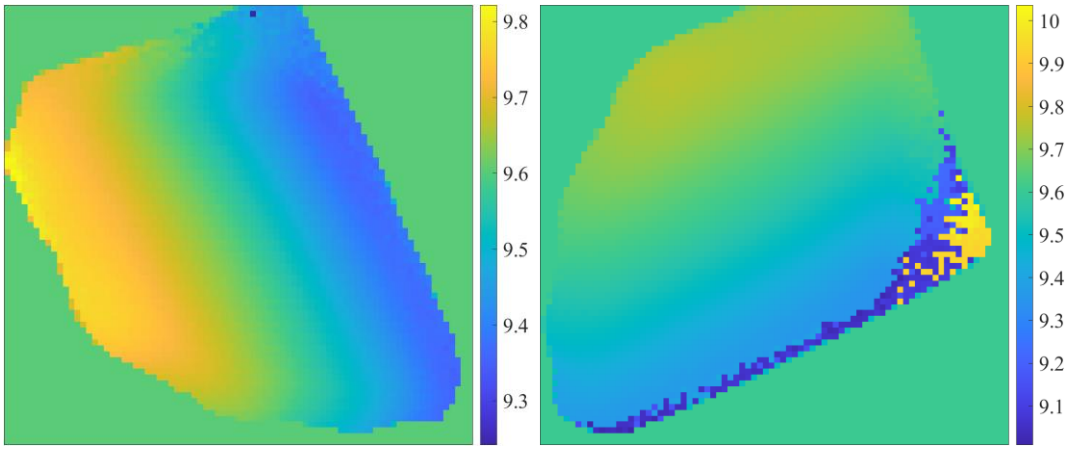

Figure 5.16 Sample thickness variations pre (Left) and post (Right) a 90 ° rotation. Some similarities are shown, but overall inconsistent results.

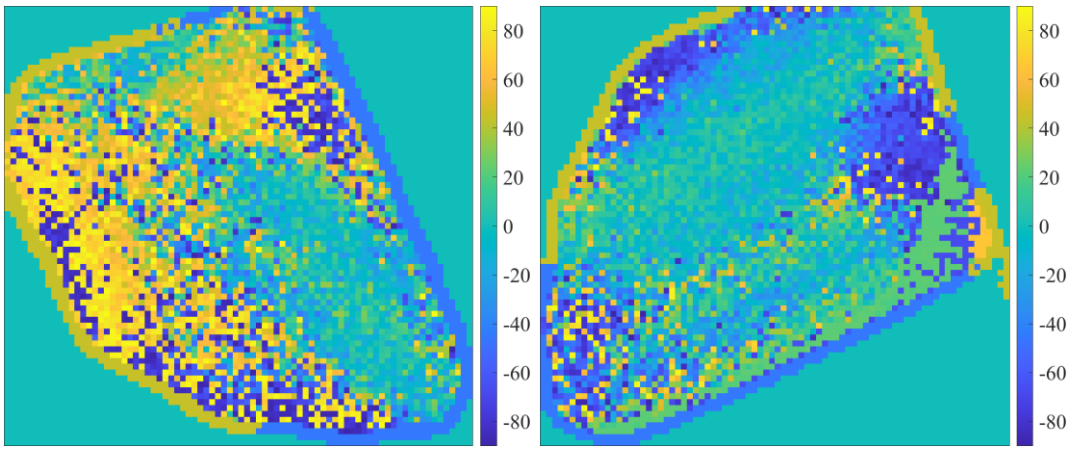

Figure 5.17 Stress angle (ϕ) measurements pre (Left) and post (Right) a 90 ° rotation. No clear 90 ° rotation of φ is observed.

Due to the lack of consistency, mainly in the thickness and stress angle measurements, the images were retaken on the sample at two different angles than the first measurements. The results are shown in the figures below.

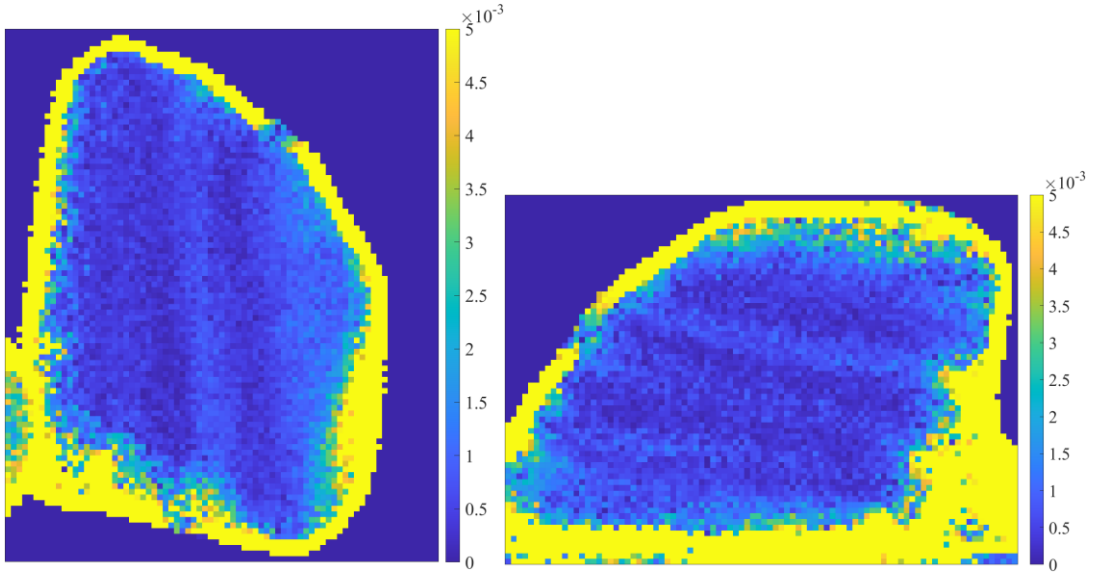

Figure 5.18 Birefringence (Δn) between the θ=0 and θ=$\pi/2$ polarization angles pre (Left) and post (Right) a 90 ° rotation. Similarities are shown. Striations of varying refractive index are visible.

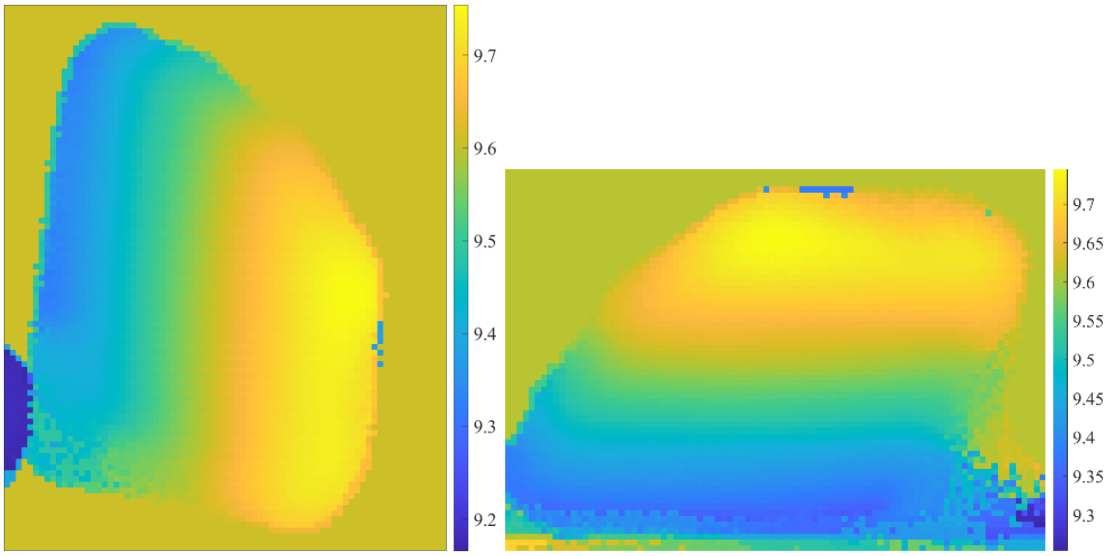

Figure 5.19 Sample thickness variations pre (Left) and post (Right) a 90 ° rotation. Similarities are shown.

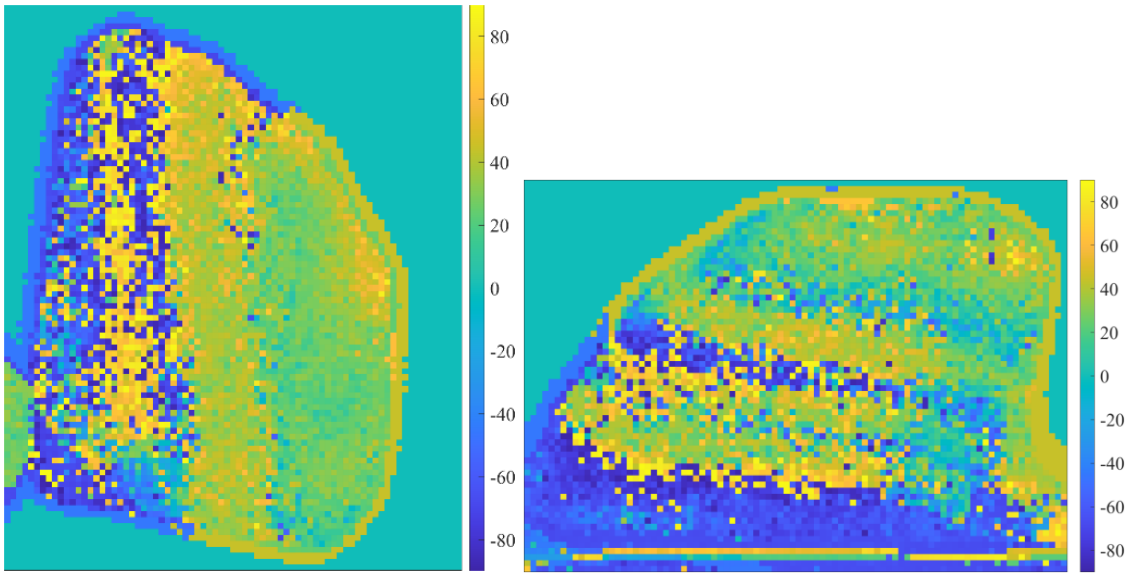

Figure 5.20 Stress angle (ϕ) measurements pre (Left) and post (Right) a 90 ° rotation. No clear 90 ° rotation of φ is observed.

The second round of tests shows different, but similarly flawed results. The birefringence magnitude (Δn) images were similar pre and post rotation, while also showing clear striations of refractive index variation throughout the sample. The thickness variations were also similar when rotated, an improvement over the first set of images. Unfortunately, the stress angle measurements still could not verify a 90 ° change when rotated. These inconsistencies with the original expectations for the experiment show that there is some flaw located in either the way the experiment was conducted, or with the original expectations based on the visual birefringence measurements.

5.3 Conclusions

THz imaging has been shown as an effective method and proof of concept for inclusion detection and NDE of amber. THz NDE does not require the removal of any encompassing opaque matrix to visually inspect for important or valuable inclusions within the specimen, eliminating the possibility of damaging the inclusion while also reducing the time needed

for detection. Index matching materials have been shown to aid in the imaging process of amber, allowing for visual inclusion separation from the surrounding amber matrix without having to physically alter the specimen. Vaseline was deemed unusable, while mineral oil is a plausible base material for an index matched material if powder separation could be handled properly.

THz CT has also been shown to be a plausible method for structural and inclusion visualization. Similar conclusions to that of the 3D printed structure reconstructions have been made. FBP assumes that all THz beams travel straight through the sample into the receiver in a perfectly parallel beam projection. Even though the refractive index matching material helps to reduce the refraction, the boundaries of the inclusions still cause refraction, damaging the parallel beam assumption. Smaller step sizes in the reconstructions were used compared to the 3D printed structures which did help structural reconstruction, but at the cost of time. It was concluded that for THz tomography to be useful for THz NDE of amber specimen, mainly due to the refractive nature of the polymers, the combination of corrective algorithms and different reconstruction methods besides standard FBP need to be implemented, just like as with 3D printed structures.

Since amber is a photoelastic material, the birefringence within was able to be visually imaged, showing the varying levels of stress within the material. Visual birefringence measurements can be effectively used for finding highly localized regions of stress within the material, while simultaneously locating inclusions within the matrix. Depending on the stress plane, it was shown that stress direction can be visually determined within a sample by comparing the amount of light transmitted through the sample using crossed linear polarizers. The Lebanese amber showed two angles corresponding to

minimum transmission, related to the stress direction. If the original orientation of the sample was noted and compared to this result, further insight on the extrusion and origin of the amber could be determined.

In attempt to determine stress direction within a material, a proof of concept was performed using an extruded block of PE. Birefringence, thickness variation, and stress angle maps were successfully created. Similar measurements were taken on the Lebanese amber sample in attempt to recreate the visual birefringence measurements minimum transmission angles. Consistent refractive index variation as well as thickness variation maps of the amber were created but the stress angle change was not consistent with the sample rotation. The idea that the birefringence should follow when a material is rotated 90 ° could only be true for certain materials, such as uniformly extruded polymer structures. Just as plausible, it could be a coincidence that the behavior was found in the PE bock. While these measurements worked accurately with the PE block, amber has a much less uniform stress distribution: containing varying layers and imperfections within. The variations in stress direction while the THz pulse transmits through the layers, may be interpreted differently depending on the angle. If the sample face is not perfectly perpendicular to the incoming pulse pre rotation, post rotation the pulse may interacting with the various regions differently, resulting in an inconsistent angle calculation. The inconsistencies presented show that there is some flaw located in either the experiment, sample, or with the original expectations and approach.

CHAPTER 6

OVERALL CONCLUSIONS AND FUTURE WORK

Many different conclusions and contributions have been made for using THz spectroscopy and imaging as a useful and effective method for the NDE of various polymer structures both mechanically and naturally extruded. Variation in the printing parameters of 3D printed structures were shown to alter the resulting THz refractive index, attenuation coefficient, and birefringence of the structure and these variations need to be accounted for when printing optical based THz components. Nozzle size and layer height are not correlated to changes in refractive index and attenuation coefficient but did alter the birefringence of the structure. Print orientation has a measurable effect on all three optical properties and should aways be taken into consideration during the FDM 3D printing process.

For creating tomographic images and 3D reconstructions of 3D printed structures using THz imaging, different aspects must be considered. FBP assumes that all THz beams travel straight through the sample into the receiver in a perfectly parallel beam projection and that THz source has an infinitely small focal point. Since this is not true in the case of THz CT, mainly due to the strong refraction and material boundaries that are encountered as the THz beam transmits through the structure being scanned, unlike methods that do not experience strong refraction, the combination of corrective algorithms and different reconstruction methods besides standard FBP need to be implemented.

THz spectroscopy has been proven as a method of electromagnetic response NDE for printed ceramics. It was shown that in the specifically used samples, as the sintering

temperature was increased, the relative permittivity of the material increased as well, while being non-dispersive over a relatively large frequency range. It was also shown that this type of ceramic structure's final size is dependent on maximum sintering temperature due to isotropic volumetric shrinkage which must be accounted for in the structural design. THz imaging was used to observe linear striation defects, confirmed as print head misalignment, and full-length cracks within the samples, confirming real flaw detection using THz as a manufacturing and structural quality NDE method.

THz NDE has been shown to be a promising method for defect detection and visualization on both MDPE and HDPE gas pipes. Reflection imaging was used to show defects including cuts, scrapes, dents, and crushed sections using both amplitude and timing measurements. A MATLAB code, shown in Appendix C, was written to create interactive 3D maps of the resulting pipe scans. These visualization techniques allow for accurate detection and location mapping of surface level and thickness variation defects, while also allowing for the detection of inner surface defects unlike visual inspection.

THz imaging has been shown as an effective method and proof of concept for inclusion detection and NDE of amber by imaging inclusions within an amber specimen. Index matching materials have been shown to aid in the imaging process of amber, allowing for visual inclusion separation from the surrounding amber matrix. THz CT has also been shown to be a plausible method for structural and inclusion visualization, but with similar conclusions to that of the 3D printed structure reconstructions, that a combination of corrective algorithms and different reconstruction methods besides standard FBP need to be implemented.

Visual birefringence images were taken on amber samples. Resulting images showed the varying levels of stress within the material while also outlining highly localized regions of stress surrounding inclusions. Planar stress direction can be visually determined within a sample by comparing the amount of light transmitted through the sample using crossed linear polarizers. Using this result, further insight on the extrusion and origin of the amber could be determined.

A proof of concept was performed using an extruded block of PE by determining its birefringence, thickness variation, and average angle of stress within the material. Similar measurements were taken on a Lebanese amber sample in attempt to recreate the visual birefringence measurements minimum transmission angles. Consistent refractive index variation as well as thickness variation maps of the amber were created but the stress angle change was not consistent with the sample rotation. The inconsistencies presented show that there is some flaw located in either the experiment, sample, or with the original expectations and approach for stress angle determination.

6.1 Future Work

For the continuation of using THz NDE on 3D printed structures, based on the results using the T-ray 5000 system, the combination of corrective algorithms and different reconstruction methods besides standard FBP need to be implemented. Previously created methods of multipeak averaging as well as correction algorithms for beam steering and Fresnel reflections should be applied [13], [14]. ART's and SART's, even though requiring more time and computational power, seem to be the next appropriate step in applying THz CT to 3D printed structures, as they have been shown useful on other

structures and materials, while also incorporating refraction corrections [60]. The corrections and alternate reconstruction methods could also be applied to amber samples, as similar difficulties in reconstruction were shown. Also, further inquiry into the effect of surface roughness on THz characteristic measurements should be made. Depending on how a sample in printed, the surface roughness may change, and this may cause distinguishable changes in spectroscopic characteristics of the resulting structure. This is shown to cause a drop off in the sample's refractive indices below 200 GHz, so there may be other associated effects that should be investigated.

For the continuation of gas pipe NDE, the reflection data for imaging pipe defects could be normalized to the amplitude data in such a way that the different defects could be characterized by their severity. The depth of the indents and gouges, the surface roughness, and the thickness of the pipe wall could effectively be extracted from the resulting data using parameters of the pipe such as pre-defect thickness and material refractive index. In the 3D pipe reconstruction using the reflection peaks, creating a model where the front surface reflection is shown on the outside and the inner reflection data is shown on the inside with the appropriate pipe thickness would be an extremely valuable tool for accurate defect location and mapping. Using spectroscopic characteristics of the pipe instead of waveform attributes should be explored. Birefringence measurements on the gas pipes may be a helpful tool in creating stress maps of the pipes and show variations in the extrusions not seen visually as well.

For continuation of the NDE of amber, creating a perfectly matched refractive index liquid would allow for better inclusion separation. Creation of a perfectly matched liquid by mixing different nonpolar liquids, as opposed to mixing in powders, would be ideal as

the possibility for separation of materials after a short time is reduced. Quantification of the visual birefringence amber measurements should be performed. For how quickly visual birefringence images can be taken for transparent amber samples, a MATLAB code could be written to effectively quantify the resulting colors, giving meaning to the color variation and strength. Lastly, further testing of the stress direction determination methodology could be performed. With the initial test on the extruded PE block working so well, there seems to be a very useful application for THz NDE within those measurements.

APPENDIX A

MATLAB CODE FOR THZ SPECTROSCOPY CHARACTERISTIC CALCULATIONS

Appendix A is the MATLAB code used to calculate and plot the time domain, frequency domain, phase information, refractive index, and attenuation coefficient using THz waveform data.

```
%Opens the 3 files needed for calculations (reference & background)
[file1, folder1] = uigetfile('FileLocation','Import Reference File');
[file3, folder3] = uigetfile('File Location','Import Background File');

%Creates name for reference, opens file, and creates data vectors.
FileName1 = file1;
TempFileName = fullfile(folder1, file1);
fid = fopen(TempFileName);
data=textscan(fid, '%f%f%*s%*s%*s%*s%*s%*s%*s%[^\n\r]',
'Delimiter','\t','headerlines', 5, 'ReturnOnError', false);
fclose(fid);
timeR=transpose(data{1});
voltageR=transpose(data{2});

%Creates name for background, opens file, and creates data vectors.
FileName3 = file3;
TempFileName = fullfile(folder3, file3);
fid = fopen(TempFileName);
data2=textscan(fid, '%f%f%*s%*s%*s%*s%*s%*s%*s%[^\n\r]', 'Delimiter',
'\t','headerlines', 5, 'ReturnOnError', false);
fclose(fid);
timeB=transpose(data2{1});
voltageB=transpose(data2{2});

c = 299792458; %speed of light in m/s

% Creates figure window for all the plots
figure1= figure('position', [0 0 1600 1000]);

%Subtracts the background data from the reference data to normalize..
voltageR = voltageR - voltageB;
a=1; d=1; answer2=1;

while answer2==1;
for b=1:3
[file2, folder2] = uigetfile('File Location','Import Object File');
```

```
%Creates name for object data, opens file, and creates data vectors.
FileName2 = file2;
TempFileName = fullfile(folder2, file2);
fid = fopen(TempFileName);
data1=textscan(fid, '%f%f%*s%*s%*s%*s%*s%*s%*s%[^\n\r]', 'Delimiter',
'\t','headerlines', 5, 'ReturnOnError', false);
fclose(fid);
timeS=transpose(data1{1});
voltageS=transpose(data1{2});
%Subtracts the background data from the object data to normalize
voltageS = voltageS - voltageB;

%Prompts for thickness of sample
answer = inputdlg('What is thickness of sample in mm?','Sample
Thickness (mm)');
Thickness = str2num(answer{1})*.001;

%Plots Time Domain
subplot(3,2,1); plot(timeR,voltageR,timeS,voltageS), title 'Time
Domain'; legend('Reference','Sample');
xlabel('time window (ps)', 'FontSize', 7); ylabel('Voltage (V)',
'FontSize', 7);

%Creates Frequency Domian
freqInterval = 0:0.00625:5; %Creates frequency range based on interval
thzScale = 5; %Change this number to display data from 0-thzScale THz
nthz = thzScale/0.00625;
freq = freqInterval(1:nthz); %truncates data up to nthz
val1 = abs(fft(voltageR)); %val1 is a placeholder (Sample)
val2 = real(val1(1:nthz)); %val2 is real values of amp in freq domain
val3 = abs(fft(voltageS)); %val1 is a placeholder (Reference)
val4 = real(val3(1:nthz)); %val4 is real values of amp in freq domain

%Plots frequency domain waveforms
subplot(3,2,2); semilogy(freq,val2), title 'Frequency Domain'; hold on;
axis tight
xlabel('Frequency (THz)', 'FontSize', 7); ylabel('Amplitude (log
scale)', 'FontSize', 7);
semilogy(freq, val4);
legend('Reference','Sample',"location", "best");
hold off;

%--------------------------------------------------------------------------
%Data Calculations begin below this line

%Phase Information
phaseTEMP = unwrap(angle(fft(voltageR)));
%phase angle of reference (unwrapped)
phaseR=transpose(phaseTEMP(1:nthz));
%only keep data for plotting from 0-nTHz
phaseTEMP = unwrap(angle(fft(voltageS)));
%phase angle of sample (unwrapped)
phaseS=transpose(phaseTEMP(1:nthz));
%only keep data for plotting from 0-nTHz
PhaseDifference=transpose(phaseR-phaseS);
%calculates difference between phases & transposes the data
```

```
PhaseDiffSlope = polyfit(freq(40:80),PhaseDifference(40:80),1);
%calculates slope of difference
IdealSlope = freq*PhaseDiffSlope(1);
%ideal line approaching 0 using slope of phase difference
PhaseDiffAvg = mean(PhaseDifference(40:80));
IdealSlopeAvg = mean(IdealSlope(40:80));

if PhaseDiffAvg<IdealSlopeAvg
%adds/subtracts slope adjustment if phase diff doesnt approach 0
    SlopeAdjustment = (IdealSlopeAvg-PhaseDiffAvg)/pi;
    SlopeAdjustment = round(SlopeAdjustment);
    PhaseDifference = PhaseDifference+(SlopeAdjustment*pi);
else
    SlopeAdjustment = (IdealSlopeAvg-PhaseDiffAvg)/pi;
    SlopeAdjustment = round(SlopeAdjustment);
    PhaseDifference = PhaseDifference-(SlopeAdjustment*pi);
end

%Plots the phase info
subplot(3,2,4); plot(freq,phaseR), title 'Phase Information'; hold on;
axis tight
plot(freq,phaseS);
plot(freq,PhaseDifference);
plot(freq,IdealSlope);
xlabel('Frequency (THz)', 'FontSize', 7); ylabel('Phase Angle
(radians)', 'FontSize', 7);
legend('Reference','Sample', 'Phase Difference', 'Ideal Slope',
"location", "best");
hold off;



%Real Refractive Index
nreal=1+(PhaseDifference.*c)./(2*pi*Thickness*freq.*10^(12));
%calculates nreal in frequency domain
subplot(3,2,3); plot(freq,nreal), title 'Real Refractive Index';
%plots nreal
xlabel('Frequency (THz)', 'FontSize', 7); ylabel('Real Index (n)',
'FontSize', 7);
legend('Real Index',"location", "best");

%Absorbance (negative log of transmittance)
MagA=log(abs(fft(voltageR))./abs(fft(voltageS)));
%Calculates the magnitude of absorbance
MagA=MagA(1:nthz); %truncate data so only upto n THz.
subplot(3,2,5); plot(freq,MagA), title 'Absorbance (Magnitude)';
%plots Magnitude of absorbance versus frequency
xlabel('Frequency (THz)', 'FontSize', 7); ylabel('Amplitude',
'FontSize', 7);
legend('Absorbance',"location", "best");
axis tight

%Attenuation Coefficient
t12=2./(1+nreal);
%transmission coefficient from air into material, normal incidence
```

```
t21=2*nreal./(nreal+1);
%transmission coefficient from material into air, normal incidence
%correct measured absorbance for fresnel reflection losses
temp=abs(fft(voltageS))./abs(fft(voltageR));
%Calculate the magnitude of absorbance creates matrix of averaged
values from 3 data points
temp1=temp(1:nthz); % truncate data so only up to n THz.
MagACorr=-log((temp1)./(t12.*t21))./Thickness;
subplot(3,2,6); plot(freq,MagACorr), title 'Attenuation Coefficient';
axis tight
xlabel('Frequency (THz)', 'FontSize', 7); ylabel('Amplitude',
'FontSize', 7);
legend('Attenaution Coeff',"location", "best");

allIndices(a,:) = nreal(1,:);
allAbsorbance(a,:) = MagA(1,:);
allAttenuation(a,:) = MagACorr(1,:);
allPhaseDiff(a,:) = PhaseDifference(1,:);
a=a+1;
end

%Creates matrix of averaged values from 3 data points
    allIndices(a,:)=(allIndices(a-1,:)+allIndices(a-2,:)+allIndices(a-
3,:))/3;
    avgIndices(d,:)= allIndices(a,:);
    allAbsorbance(a,:)=(allAbsorbance(a-1,:)+allAbsorbance(a-
2,:)+allAbsorbance(a-3,:))/3;
    avgAbsorbance(d,:)= allAbsorbance(a,:);
    allAttenuation(a,:)=(allAttenuation(a-1,:)+allAttenuation(a-
2,:)+allAttenuation(a-3,:))/3;
    avgAttenuation(d,:)= allAttenuation(a,:);
    allPhaseDiff(a,:)=(allPhaseDiff(a-1,:)+allPhaseDiff(a-
2,:)+allPhaseDiff(a-3,:))/3;
    avgPhaseDiff(d,:)= allPhaseDiff(a,:);
    a=a+1; d=d+1;
answer2 = inputdlg('Another Sample? 1=Y, 2=N');
answer2 = str2num(answer2{1});
end
```

APPENDIX B

MATLAB CODE TO CREATE TOMOGRAPHIC IMAGES BASED ON 2D THZ IMAGES

Appendix B is the MATLAB code used to create tomographic images from 2D Thz images taken at a series of individual angles around a sample. The output is a series of images depending on the number of horizontal scans performed.

```
%Code assumes that picoimages are x-y 2D images at FIXED angle of
sample and sample is rotated about the y axis.
%Center of rotation is center of x axis of 2D array.
%All the picoimage files in the directory are a fixed angular spacing
apart.

FilterSpec='File Location';
prompt='What is the File Name of the picoimage for the first rotation
angle?';
[FName,FPathName,FilterIndex] = uigetfile(FilterSpec,prompt);
initFileNum=sscanf(FName,'%d'); % initial file number (in case file
number doesnot strate at zero
FName=[FPathName,FName];
folder2=strcat(FPathName,'*.picoimage');
NpicoImageFiles=length(dir(folder2));
%number of picoimage files in directory
DeltaTheta=360/NpicoImageFiles; % angular rotation between picoimages

%change lines below depending on analysis methoc
deltanu=1/160; % frequency interval in THz.
fmin=round(0.5/deltanu); % index of lowest THz frequency for analysis
fmax=round(2.0/deltanu);% index of lowest THz frequency for analysis

for itheta=initFileNum:initFileNum+NpicoImageFiles-1
    FName=sprintf('%d.picoimage',itheta);% file name for picoimage file
    FName=[FPathName,FName]; % complete path name
    [Step,Scan,wfm,PicoIm] = read_picoimage_file(FName);
%read picoimage data
    if itheta==initFileNum % if first time through loop, allocate array
        AllSlices=zeros(Step.NumPix,Scan.NumPix,NpicoImageFiles);
    end
    disp(FName)
    for i=1:Step.NumPix
        for j=1:Scan.NumPix
            voltage=wfm((i-1)*Scan.NumPix+j,:);
%waveform at this pixel
            magS=abs(fft(voltage)); % magnitude of FFT
            myImage(i,j)=mean(magS(fmin:fmax));
%image corresponding to E strength in freq band.
```

```
        end
    end
    AllSlices(:,:,itheta)=myImage;
%save 2D x-y image of data based on analysis of each pixel
    imagesc(myImage); % display x-y image as processed for each theta
    pause(0.1);
%pause so that you get 'movie' of the images as they display
end

yNum=size(AllSlices,1); %number of y positions
path=uigetdir('*.txt'); %choose directory in which to store image data
for 'stack' structure in FIJI
fnamelist=[path,'\test.txt']; % name of file which will be LIST of
filenames. Each file name is a SLICE in the image
fileID = fopen(fnamelist,'w'); % open file which is the LIST of
filenames

for iy=1:yNum
    temp=AllSlices(iy,:,:);
%select out projection data for specific y position
    mydata=reshape(temp,size(AllSlices,2),size(AllSlices,3));
    myRecon=iradon(mydata,DeltaTheta);
%inverse radon transformation assuming DeltaTheta rotation angle
    imagesc(myRecon);
%plot slice so that you can see 'movie' of slices
    pause(0.1);
%pause so that you get 'movie' of the images as they display

formatSpec='slice%d.txt';
    slicename=sprintf(formatSpec,iy); % create file name of slice
    myName=[path,'\',slicename]; % complete path to the file
    writematrix(myRecon,myName);
%write the reconstructed image data to the file.
    formatSpec='%s\n';
    fprintf(fileID,formatSpec,myName);
%Print list of file path locations
end

fclose(fileID); % close file containing list of file path locations
```

APPENDIX C

MATLAB CODE TO CREATE IMAGES FROM PIPE REFLECTION DATA

Appendix C is the MATLAB code used to create and display images and renders of polyethylene gas pipes by combining multiple vertical scans at discrete angles along the length of pipe.

```
%TubeScan scans the tube data
prompt = {'How many SCANS are there?','What is the first number of the
SCAN?','What is the variable number? (OP0#)', 'How tall was the
verticle scan? (mm)','Pipe Diameter? (mm)','Degrees in each
rotation?'};
addpath(pwd) %add the working directory

title = 'Inputs'; dims = [1 50];
definput = {'360','1','2','300','58','1'}; %format of current files
answers = inputdlg(prompt,title,dims,definput);

answers = str2num(char(answers)); %#ok<ST2NM>

scanNum = answers(1); %number of verticle scans
shift = answers(2); %starting number for the excel sheets
variable = answers(3); %the variable scanned
height = answers(4);
diameter = answers(5);
degrees = answers(6);
radius = diameter/2;
theta = degrees*scanNum;
arc = theta/360;
arclength = @(radius,arc) 2*pi*radius*arc;
zscale = height/diameter;
startRow = 3; %start of data in txt file
endRow = 1026; %end of data in txt file

prompt = 'What folder contains the scan data?';
folder = [uigetdir(cd(),prompt),'/'];
%Use this if you want to choose a folder
addpath(folder)

for i=shift:scanNum+shift-1
scanName = 'scan%d_OP0%d.csv';
A1 = i;
A2 = variable;
str = sprintf(scanName,A1,A2);
Q(i,:)=csvread(str); %#ok<SAGROW>
disp(str)
```

```
end
% Visualize data
figure(1)
imagesc(flip(Q'))%, 'XData', [0 arclength], 'YData', [0 height]), axis
image
set(gca,'XTick',[]) % Remove the ticks in the x axis!
set(gca,'YTick',[]) % Remove the ticks in the y axis
set(gca,'Position',[0 0 1 1]) % Make the axes occupy the whole figure
saveas(gcf,'Figure1234','png')
%
figure(2)
imgRGB=imread('Figure1234.png');
[imgRows,imgCols,imgPlanes]=size(imgRGB);
[X,Y,Z]=cylinder(imgRows,imgCols);

for phi=0:5:720
    warp(X,Y,Z,imgRGB), colorbar, pbaspect([1 1 zscale])
    zlabel('height')
    view(phi,30),drawnow
    %creates gif of pipe map
    pause(0.001)
end
```

APPENDIX D

MATALB CODE FOR DETERMINATION OF BIREFRINGENCE MAGNITUDE AND DIRECTION

Appendix D is the MATLAB code used determine the direction of stress, thickness variations, and birefringence magnitude within the material scanned based of Dr' John Federici's personal notes written August 27th, 2020.

```
%Code to develop birefringence magnitude and direction from time delay
of pulses
%Reference is "Determine Stress Direction from Birefringence" Personal
notes of Dr. John federici 8/27/2020
%It is assumed that time delay of front surface reflection and back
surface reflection are already saved as images in comma separated value
(CSV) EXCEL files by TRAY 5000 system

FilterSpec='File Location';
prompt='What is the 0 degree polarization image File Name?';
disp(prompt)
[RefName,RPathName,FilterIndex] = uigetfile(FilterSpec,prompt);
FName=[RPathName,RefName]; disp(FName)
[ArrayData0] = ImportCSVimage(FName);

FilterSpec=[RPathName,'*.csv'];
prompt='What is the -45 degree polarization image File Name?';
disp(prompt)
[RefName,RPathName,FilterIndex] = uigetfile(FilterSpec,prompt);
FName=[RPathName,RefName]; disp(FName)
[ArrayDataM45] = ImportCSVimage(FName);

prompt='What is the +45 degree polarization image File Name?';
disp(prompt)
[RefName,RPathName,FilterIndex] = uigetfile(FilterSpec,prompt);
FName=[RPathName,RefName]; disp(FName)
[ArrayDataP45] = ImportCSVimage(FName);

prompt='Average Sample Refractive Index?';
disp(prompt)
answer=inputdlg(prompt,'Average Sample Refractive Index?', [1
50],{'1.57'});
Navg=str2num(answer{1}) % sample refractive index

LHS=(ArrayDataM45-ArrayData0)./(ArrayDataM45-ArrayDataP45);
%image array corresponding to values from LHS of equation
phiLimits = [0 pi/2]; % limits of direction of stress
phi=zeros(length(ArrayData0(:,1)),length(ArrayData0(1,:)));
%initialize solution array
```

```
DeltaT=phi; %initialize solution array
nxny=ArrayDataM45-ArrayDataP45; %define experimental values for
determining magnitude and direction of birefringence
nxnpi=ArrayDataM45-ArrayData0;
npiny=ArrayData0-ArrayDataP45;

for i=1:length(ArrayData0(:,1)); % number of rows in image
    for j=1:length(ArrayData0(1,:)) % number of columns in image
        disp(sprintf('i=%d j=%d',i,j))
        LHSValue=LHS(i,j); % LHS value for this pixel
        [mydeltan,myphi] =
BirefrMagDir(nxny(i,j),nxnpi(i,j),npiny(i,j),LHSValue);
        DeltaT(i,j)=mydeltan;
        phi(i,j)=myphi;
    end
end

Thick=(ArrayDataP45+ArrayDataM45)/2*1e-12*3e8/2/Navg*1e3;
%sample thickness (in mm)
Deltan=DeltaT*1e-12*3e8./(2*Thick*1e-3);
%Convert from time difference to refractive index different. need to
multiply thickness times 2 since in reflection measurement, light
passes through material twice. Try to remove variations in thickness in
calculation.

figure('Name','Delta N')
set(gcf,'position',[100,100,1100,700])
imagesc(Deltan); colorbar;
set(gca,'XTick',[]) % Remove the ticks in the x axis
set(gca,'YTick',[]) % Remove the ticks in the y axis
axis image

figure('Name','Phi');
set(gcf,'position',[100,100,1100,700])
imagesc(phi);  colorbar;
set(gca,'XTick',[]) % Remove the ticks in the x axis
set(gca,'YTick',[]) % Remove the ticks in the y axis
axis image

figure('Name','Thickness Variation');
set(gcf,'position',[100,100,1100,700])
imagesc(Thick);  colorbar;
set(gca,'XTick',[]) % Remove the ticks in the x axis
set(gca,'YTick',[]) % Remove the ticks in the y axis
axis image


%-------------------------------------------------------------------------
%Function "BirefrMagDir" inserted below this line


function [deltan,phi] = BirefrMagDir(nxny,nxnpi,npiny,LHSValue)
% Function to return the direction and birefringence (delta n) from THz
time-domain measurements

% Input parameters - If in units of ps, then "delta n" output is also
in units of ps.
```

```
% nxny - time difference between light polarized in x direction minus
light polarized in y direction.
% nxnpi - time difference between light polarized in x direction minus
light polarized at 45 degrees (mid way between x and y direction).
% npiny -  time difference between light polarized at 45 degrees (mid
way between x and y direction) minus light polarized in y direction.
% LHSValue - Left hand side value for equation to determine stress and
magnitude. Equation from "Determining Stress Direction From
Birefringence", Dr. John Federici personal notes 8/27/2020.

% One can use the following code to test code to make sure equations
for determining direction of strength of birefringence are correct.

% phi0=-45/180*pi; % direction of strength
% deltan=0.001; %magnitude of delta n. This needs to be a small number
because of approximation in theory.
% n1=1+deltan/2; % slow axis
% n2=1-deltan/2; % fast axis
% nx=n1*n2/sqrt(n1^2*sin(phi0)^2+n2^2*cos(phi0)^2);
% ny=n1*n2/sqrt(n1^2*cos(phi0)^2+n2^2*sin(phi0)^2);
% npi=n1*n2/sqrt(n1^2*sin(pi/4-phi0)^2+n2^2*cos(pi/4-phi0)^2);
% %
% % now define 'measured' values
% nxny=nx-ny;
% nxnpi=nx-npi;
% npiny=npi-ny;

%Start of main code for function
phiLimits=[0 0];
myfun1 = @(x,LHSValue) (1-sin(2*x)-2*sin(x).^2)./(2*(2*cos(x).^2-1))-
LHSValue;  % parameterized function
    % LHS value is for (nx-npi)/(nx-ny). Valid EXCEPT near x=+/- pi/4
myfun2 = @(x,LHSValue) (1-sin(2*x)-2*sin(x).^2)./(-
1+sin(2*x)+2*cos(x).^2)-LHSValue;  % parameterized function
% LHS value is for (nx-npi)/(npi-ny). Valid NEAR x=+/- pi/4
%use this angles are NEGATIVE between -pi/4 and -3pi/8 and Positive
% angles between pi/8 and pi/4

myfun3 = @(x,LHSValue) (-1+sin(2*x)+2*cos(x).^2)./(1-sin(2*x)-
2*sin(x).^2)-LHSValue;  % parameterized function
    % LHS value is for (npi-ny)/(nx-npi). Valid NEAR x=+/- pi/4
    % use this angles are NEGATIVE between -pi/4 and -pi/8 and Positive
    % angles between pi/4 and 3pi/8

%Handles cases where THz light not going through sample so that all
time delays = 0.
if nxny==0 && nxnpi==0 && npiny==0
    deltan=0; phi=0;
else
    if nxny > 0 % nx-ny>0 means angle magnitude < pi/4
        if (nxnpi >0 && npiny > 0)
            if nxnpi>npiny
                phiLimits=[-pi/8 0];
            else
                phiLimits=[0 pi/8];
            end
                LHSValue=nxnpi/nxny; % LHS value of equation
```

```
                fun = @(x) myfun1(x,LHSValue);
% use function 1 for this range of phi limits
        else
            if nxnpi>0 && npiny<=0
                phiLimits=[-pi/4 -pi/8];
                LHSValue=npiny/nxnpi; % LHS value of equation
                fun = @(x) myfun3(x,LHSValue);
% use function 3 for this range of phi limits
            else
                phiLimits=[pi/8 pi/4];
                LHSValue=nxnpi/npiny; % LHS value of equation
                fun = @(x) myfun2(x,LHSValue);
%use function 3 for this range of phi limits
            end
        end
    else
        if nxnpi>=0 && npiny <0
            phiLimits=[-3*pi/8 -pi/4];
            LHSValue=nxnpi/npiny; % LHS value of equation
            fun = @(x) myfun2(x,LHSValue);
%use function 1 for this range of phi limits
        end
        if nxnpi<0 && npiny>0
            phiLimits=[pi/4 3*pi/8];
            LHSValue=npiny/nxnpi; % LHS value of equation
            fun = @(x) myfun3(x,LHSValue);
%use function 1 for this range of phi limits
        end
        if nxnpi<0 && npiny<=0
            if nxnpi > npiny
                phiLimits=[-pi/2 -3*pi/8];
            else
                phiLimits=[3*pi/8 pi/2];
            end
            LHSValue=nxnpi/nxny; % LHS value of equation
            fun = @(x) myfun1(x,LHSValue);
%use function 1 for this range of phi limits
        end
    end
    x = fzero(fun,phiLimits);
%find direction of stress by determining zero of equation
    if abs(pi/4-x)>0.1 && abs(pi/4+x)>0.1
        deltan=nxny/(2*cos(x)^2-1);
%if not near phi=+/- pi/4 then us this to solve for delta n
    else
        deltan=nxnpi*2/(1-sin(2*x)-2*sin(x)^2);
%if near phi=+/i pi/4 then use this to solve for delta n
    end
    phi=x/pi*180; % return direction in units of degrees
end
end
```

REFERENCES

[1] N. Sathishkumar, A. S. M. Udayakumar, B. Vincent, and V. A. Kumar, "Study and Analysis of 3D Printed FDM Components by Non-Destructive Testing Techniques," *International Journal of Research and Review*, no. 5, p. 6, 2020.

[2] S. Wang and X.-C. Zhang, "Pulsed Terahertz Tomography," *Journal of Physics D: Applied Physics*, vol. 37, no. 4, pp. R1–R36, Jan. 2004, doi: 10.1088/0022-3727/37/4/R01.

[3] E. Seeram and P. C. Brennan, *Radiation Protection in Diagnostic X-Ray Imaging*. Burlington, MA: Jones & Bartlett Publishers, 2016.

[4] Y. Wang "Radiation Safety Guidelines," *X-ray Diffraction (XRD) Laboratory*, Analytical Centre, University of New South Wales, p. 8, 2007.

[5] N. S. Murthy, "X-ray Diffraction from Polymers," in *Polymer Morphology*, Hoboken, NJ: John Wiley & Sons, Ltd, 2016, pp. 14–36. doi: 10.1002/9781118892756.ch2.

[6] R. Alfattni, "Comprehensive Study on Materials used in Different Types of Additive Manufacturing and their Applications," *The International Journal of Mathematical, Engineering and Management Sciences*, vol. 7, no. 1, pp. 92–114, Jan. 2022, doi: 10.33889/IJMEMS.2022.7.1.007.

[7] B. Evans, "Practical 3D Printers: The Science and Art of 3D Printing," Netherlands, Apress, 2012, p. 321.

[8] S. Moylan, "Qualification for Additive Manufacturing Materials, Processes, and Parts," *Production Systems Group*, Gaithersburg, MD, Accessed on: Jan. 2020, [Online]. Available: https://www.nist.gov/programs-projects/qualification-additive-manufacturing-materials-processes-and-parts

[9] J. Fielding *et al.*, "Final Report - Department of Defense Additive Manufacturing Roadmap." Washington, D.C., Department of Defense, Accessed on: Feb. 2018. [Online]. Available: https://www.americamakes.us/wp-content/uploads/2021/10/Final-Report-DoDRoadmapping-FINAL120216.pdf

[10] Joint Defense Manufacturing Council, "Department of Defense Additive Manufacturing Strategy," Washington, D.C., Department of Defense, Accessed on: Jan. 2021, [Online]. Available: https://www.cto.mil/wp-content/uploads/2021/01/dod-additive-manufacturing-strategy.pdf

[11] M. Zhao, Y. Geng, S. Fan, X. Yao, M. Zhu, and Y. Zhang, “3D-Printed Strong Hybrid Materials with Low Shrinkage for Dental Restoration,” *Composites Science and Technology*, vol. 213, p. 108902, Sep. 2021, doi: 10.1016/j.compscitech.2021.108902.

[12] B. Recur *et al.*, “Investigation on Reconstruction Methods Applied to 3D Terahertz Computed Tomography,” *Optics Express*, vol. 19, no. 6, p. 5105, Mar. 2011, doi: 10.1364/OE.19.005105.

[13] E. Abraham, A. Younus, C. Aguerre, P. Desbarats, and P. Mounaix, “Refraction Losses in Terahertz Computed Tomography,” *Optics Communications*, vol. 283, no. 10, pp. 2050–2055, May 2010, doi: 10.1016/j.optcom.2010.01.013.

[14] S. Mukherjee, J. Federici, P. Lopes, and M. Cabral, “Elimination of Fresnel Reflection Boundary Effects and Beam Steering in Pulsed Terahertz Computed Tomography,” *Journal of Infrared, Millimeter, and Terahertz Waves*, vol. 34, no. 9, pp. 539–555, Sep. 2013, doi: 10.1007/s10762-013-9985-3.

[15] D. Rohrbach, B. J. Kang, and T. Feurer, “3D-Printed THz Wave- and Phaseplates,” *Optics Express, OE*, vol. 29, no. 17, pp. 27160–27170, Aug. 2021, doi: 10.1364/OE.433881.

[16] B. Zhang, W. Chen, Y. Wu, K. Ding, and R. Li, “Review of 3D Printed Millimeter-Wave and Terahertz Passive Devices,” *International Journal of Antennas and Propagation*, vol. 2017, p. e1297931, Jul. 2017, doi: 10.1155/2017/1297931.

[17] A. Siemion *et al.*, “THz Diffractive Lens Manufactured Using 3D Printer Working for 0.6 THz,” in *2020 23rd International Microwave and Radar Conference (MIKON)*, Oct. 2020, pp. 225–228. doi: 10.23919/MIKON48703.2020.9253821.

[18] A. Goulas *et al.*, “Microstructure and Microwave Dielectric Properties of 3D Printed Low Loss Bi2Mo2O9 Ceramics for LTCC Applications,” *Applied Materials Today*, vol. 21, p. 100862, Dec. 2020, doi: 10.1016/j.apmt.2020.100862.

[19] C. D. Morales, C. Morlaas, A. Chabory, R. Pascaud, M. Grzeskowiak, and G. Mazingue, “3D-Printed Ceramics with Engineered Anisotropy for Dielectric Resonator Antenna Applications,” *Electronics Letters*, vol. 57, no. 18, pp. 679–681, 2021, doi: 10.1049/ell2.12234.

[20] H. Yasuda and I. Hosako, “Measurement of Terahertz Refractive Index of Metal with Terahertz Time-Domain Spectroscopy,” *Journal of Applied Physics*, vol. 47, no. 3, pp. 1632–1634, Mar. 2008, doi: 10.1143/JJAP.47.1632.

[21] T. Yilmaz and O. b. Akan, “Attenuation Constant Measurements of Clear Glass Samples at the Low Terahertz Band,” *Electronics Letters*, vol. 56, no. 25, pp. 1423–1425, 2020, doi: 10.1049/el.2020.1593.

[22] A. J. Waddie *et al.*, "Terahertz Optical Thickness and Birefringence Measurement for Thermal Barrier Coating Defect Location," *Optiics Express, OE*, vol. 28, no. 21, pp. 31535–31552, Oct. 2020, doi: 10.1364/OE.398532.

[23] X. Ruan and C. H. Chan, "Terahertz Free-Space Dielectric Property Measurements Using Time- and Frequency-Domain Setups," *International Journal of RF and Microwave Computer-Aided Engineering*, vol. 29, no. 9, p. e21839, 2019, doi: 10.1002/mmce.21839.

[24] S. F. Busch, M. Weidenbach, M. Fey, F. Schäfer, T. Probst, and M. Koch, "Optical Properties of 3D Printable Plastics in the THz Regime and their Application for 3D Printed THz Optics," *Journal of Infrared, Millimeter, and Terahrtz Waves*, vol. 35, no. 12, pp. 993–997, Dec. 2014, doi: 10.1007/s10762-014-0113-9.

[25] M. Scheller, "Data Extraction from Terahertz Time Domain Spectroscopy Measurements," *Journal of Infrared, Millimeter, and Terahrtz Waves*, vol. 35, no. 8, pp. 638–648, Aug. 2014, doi: 10.1007/s10762-014-0053-4.

[26] A. D. Squires, E. Constable, and R. A. Lewis, "3D Printed Terahertz Diffraction Gratings And Lenses," *Journal of Infrared, Millimeter, and Terahrtz Waves*, vol. 36, no. 1, pp. 72–80, Jan. 2015, doi: 10.1007/s10762-014-0122-8.

[27] A. D. Squires and R. A. Lewis, "Feasibility and Characterization of Common and Exotic Filaments for Use in 3D Printed Terahertz Devices," *Journal of Infrared, Millimeter, and Terahrtz Waves*, vol. 39, no. 7, pp. 614–635, Jul. 2018, doi: 10.1007/s10762-018-0498-y.

[28] "Chapter 4 - PE Pipe and Fittings Manufacturing," in *The Plastics Pipe Institute Handbook of Polyethylene Pipe*, Irving, TX: Plastics Pipe Institute, pp. 105-123.

[29] "Practice for Heat Fusion Joining of Polyethylene Pipe and Fittings," West Conshohocken, PA, USA: ASTM International, 2019, doi: 10.1520/F2620-19.

[30] M. Shafiei Alavijeh, R. Scott, F. Seviaryn, and R. Gr. Maev, "NDE 4.0 Compatible Ultrasound Inspection of Butt-Fused Joints of Medium-Density Polyethylene Gas Pipes, Using Chord-type Transducers Supported by Customized Deep Learning Models," *Research in Nondestructive Evaluation*, vol. 31, no. 5–6, pp. 290–305, Nov. 2020, doi: 10.1080/09349847.2020.1841864.

[31] A. Ghavamian, F. Mustapha, B. T. H. T. Baharudin, and N. Yidris, "Detection, Localisation and Assessment of Defects in Pipes Using Guided Wave Techniques: A Review," *Sensors (Basel)*, vol. 18, no. 12, p. 4470, Dec. 2018, doi: 10.3390/s18124470.

[32] T. S. McKnight and E. J. Mullins, *Canadian Woods: Their Properties and Uses*. Toronto, UNKNOWN: University of Toronto Press, 1981. Accessed: Aug. 06, 2021. [Online]. Available: http://ebookcentral.proquest.com/lib/njit/detail.action?docID=4671317

[33] J. H. Langenheim, *Plant Resins: Chemistry, Evolution, Ecology, and Ethnobotany*. Portland, Or: Timber Press, 2003.

[34] A. Cunningham, P. R. West, G. S. Hammond, and J. H. Langenheim, "The Existence and Photochemical Initiation of Free Radicals in Hymenaea Trunk Resin," *Phytochemistry*, vol. 16, no. 9, pp. 1442–1443, Jan. 1977, doi: 10.1016/S0031-9422(00)88803-2.

[35] L. J. Seyfullah, C. Beimforde, J. D. Corso, V. Perrichot, J. Rikkinen, and A. R. Schmidt, "Production and Preservation of Resins – Past and Present," *Biological Reviews*, vol. 93, no. 3, pp. 1684–1714, 2018, doi: 10.1111/brv.12414.

[36] D. Grimaldi, M. S. Engel, M. S. Engel, and S. C. and P. M. S. Engel, *Evolution of the Insects*. Cambridge University Press, 2005.

[37] C. Jansen *et al.*, "Terahertz Imaging: Applications and Perspectives," *Applied Optics, AO*, vol. 49, no. 19, pp. E48–E57, Jul. 2010, doi: 10.1364/AO.49.000E48.

[38] T. Sasaki, Y. Hashimoto, T. Mori, and S. Kojima, "Broadband Terahertz Time-Domain Spectroscopy of Archaeological Baltic Amber," *International Letters of Chemistry, Physics and Astronomy*, vol. 62, pp. 29–33, 2015, doi: 10.18052/www.scipress.com/ILCPA.62.29.

[39] J. B. Perraud, J. B. Sleiman, F. Simoens, and P. Mounaix, "Immersion in Refractive Index Matching Liquid for 2D and 3D Terahertz Imaging," in *2015 40th International Conference on Infrared, Millimeter, and Terahertz waves (IRMMW-THz)*, Hong Kong, China, Aug. 2015, pp. 1–1. doi: 10.1109/IRMMW-THz.2015.7327706.

[40] J. B. Perraud *et al.*, "Liquid Index Matching for 2D and 3D Terahertz Imaging," *Applied Optics*, vol. 55, no. 32, p. 9185, Nov. 2016, doi: 10.1364/AO.55.009185.

[41] E. Mavrona *et al.*, "Terahertz Refractive Index Matching Solution," *Optics Express, OE*, vol. 27, no. 10, pp. 14536–14544, May 2019, doi: 10.1364/OE.27.014536.

[42] D. R. Bacon, J. Madéo, and K. M. Dani, "Photoconductive Emitters for Pulsed Terahertz Generation," *Journal of Optics*, vol. 23, no. 6, p. 064001, Apr. 2021, doi: 10.1088/2040-8986/abf6ba.

[43] N. M. Burford and M. O. El-Shenawee, "Review of Terahertz Photoconductive Antenna Technology," *Optical Engineering*, vol. 56, no. 1, p. 010901, Jan. 2017, doi: 10.1117/1.OE.56.1.010901.

[44] F. Simoens, "THz Bolometer Detectors," in *Physics and Applications of Terahertz Radiation*, M. Perenzoni and D. J. Paul, Eds. Dordrecht: Springer Netherlands, 2014, pp. 35–75. doi: 10.1007/978-94-007-3837-9_2.

[45] S. S. Prabhu, “Chapter 4 - Terahertz Spectroscopy: Advances and Applications,” in *Molecular and Laser Spectroscopy*, V. P. Gupta, Ed. Elsevier, 2018, pp. 65–85. doi: 10.1016/B978-0-12-849883-5.00004-8.

[46] V. Ganapati *et al.*, “Infrared Birefringence Imaging of Residual Stress and Bulk Defects in Multicrystalline Silicon,” *Journal of Applied Physics*, vol. 108, no. 6, p. 063528, Sep. 2010, doi: 10.1063/1.3468404.

[47] J. Peatross and M. Ware, *Physics of light and optics*. 2020. Accessed: Mar. 16, 2022. [Online]. Available: http://optics.byu.edu/docs/opticsBook.pdf

[48] J. S. White, D. Zimdars, and I. Duling, “Very High Speed THz Imaging of Foam Density and Other Defects,” in *2016 41st International Conference on Infrared, Millimeter, and Terahertz waves (IRMMW-THz)*, Sep. 2016, pp. 1–2. doi: 10.1109/IRMMW-THz.2016.7758567.

[49] A. T. Clark, J. F. Federici, and I. Gatley, “Effect of 3D Printing Parameters on the Refractive Index, Attenuation Coefficient, and Birefringence of Plastics in Terahertz Range,” *Advances in Materials Science and Engineering*, vol. 2021, p. e8276378, Nov. 2021, doi: 10.1155/2021/8276378.

[50] R. Schofield *et al.*, “Image Reconstruction: Part 1 - Understanding Filtered Back Projection, Noise and Image Acquisition,” *Journal of Cardiovascular Computed Tomography*, vol. 14, no. 3, pp. 219–225, Jun. 2020, doi: 10.1016/j.jcct.2019.04.008.

[51] O. Taubmann, M. Berger, M. Bögel, Y. Xia, M. Balda, and A. Maier, “Computed Tomography,” in *Medical Imaging Systems: An Introductory Guide*, A. Maier, S. Steidl, V. Christlein, and J. Hornegger, Eds. Cham (CH): Springer, 2018. Accessed: Apr. 01, 2022. [Online]. Available: http://www.ncbi.nlm.nih.gov/books/NBK546157/

[52] A. P. Dhawan, *Medical Image Analysis*. Hoboken, NJ: Wiley-Interscience, 2011.

[53] M. Biron, *Thermoplastics and Thermoplastic Composites*. Norwich, NY: William Andrew, 2012.

[54] Md. Hazrat Ali and A. Abilgaziyev, “Fused Deposition Modeling Based 3D Printing: Design, Ideas, Simulations,” in *Fused Deposition Modeling Based 3D Printing*, H. K. Dave and J. P. Davim, Eds. Cham: Springer International Publishing, 2021, pp. 23–42. doi: 10.1007/978-3-030-68024-4_2.

[55] J. A. Colla, R. E. M. Vickers, M. Nancarrow, and R. A. Lewis, “3D Printing Metallised Plastics as Terahertz Reflectors,” *Journal of Infrared, Millimeter, and Terahertz Waves*, vol. 40, no. 7, pp. 752–762, Jul. 2019, doi: 10.1007/s10762-019-00596-y.

[56] R. Burger *et al.*, “THz-TDS Reflection Measurement of Coating Thicknesses at Non-Perpendicular Incidence: Experiment and Simulation,” *Sensors*, vol. 21, no. 10, Art. no. 10, Jan. 2021, doi: 10.3390/s21103473.

[57] T. Fukuchi, N. Fuse, M. Mizuno, and K. Fukunaga, “THz Measurement of Refractive Index and Thickness of Ceramic Coating on a Metal Substrate,” in *2013 Conference on Lasers and Electro-Optics Pacific Rim (CLEOPR)*, Jun. 2013, pp. 1–2. doi: 10.1109/CLEOPR.2013.6600103.

[58] S. Mukherjee and J. Federici, “Study of Structural Defects Inside Natural Cork by Pulsed Terahertz Tomography,” in *2011 International Conference on Infrared, Millimeter, and Terahertz Waves*, Houston, TX, USA, Oct. 2011, pp. 1–2. doi: 10.1109/irmmw-THz.2011.6104965.

[59] P. Parsons, A. Clark, Z. Larimore, A.J. Good, S. Gatley, J. Federici, and M. Mirotznik, “Millimeter and Sub-millimeter Wave Electromagnetic Characterization of Additively Manufactured Zirconia Ceramics via NanoParticle Jetting.” *IEEE Transactions on Components, Packaging and Manufacturing Technology*, Under Review.

[60] J. Tepe, T. Schuster, and B. Littau, “A Modified Algebraic Reconstruction Technique Taking Refraction Into Account with an Application in Terahertz Tomography,” *Inverse Problems in Science and Engineering*, vol. 25, no. 10, pp. 1448–1473, Oct. 2017, doi: 10.1080/17415977.2016.1267168.

[61] V. V. Parshin, E. A. Serov, A. V. Vodopyanov, and D. A. Mansfeld, “Method to Measure the Dielectric Parameters of Powders in Subterahertz and Terahertz Ranges,” *IEEE Transactions on Terahertz Science and Technology*, vol. 11, no. 4, pp. 375–380, Jul. 2021, doi: 10.1109/TTHZ.2021.3076698.

[62] A. K. and S. Varghese, “Role of Surfactants on the Stability of Nano-Zinc Oxide Dispersions,” *Particulate Science and Technology*, vol. 35, no. 1, pp. 67–70, Jan. 2017, doi: 10.1080/02726351.2015.1131787.

[63] D. Sarkar, S. Tikku, V. Thapar, R. S. Srinivasa, and K. C. Khilar, “Formation of Zinc Oxide Nanoparticles of Different Shapes in Water-in-Oil Microemulsion,” *Colloids and Surfaces A: Physicochemical and Engineering Aspects*, vol. 381, no. 1–3, pp. 123–129, May 2011, doi: 10.1016/j.colsurfa.2011.03.041.

[64] J. H. Jang, S. Wang, S. M. Pilgrim, and W. A. Schulze, “Preparation and Characterization of Barium Titanate Suspensions for Stereolithography,” *Journal of the American Ceramic Society*, vol. 83, no. 7, pp. 1804–1806, Dec. 2004, doi: 10.1111/j.1151-2916.2000.tb01467.x.